AD-A215 943

GL-TR-89-0153

# Investigating the Effects Fracture Systems Have on Seismic Wave Velocities at the Lajitas, Texas Seismic Station


Victoria L. Sandidge-Bodoh

Southern Methodist University
Department of Geological Sciences
Dallas, TX 75275


1 May 1989

Final Report
3 March 1987 - 2 March 1989

**APPROVED FOR PUBLIC RELEASE; DISTRIBUTION UNLIMITED**




GEOPHYSICS LABORATORY
AIR FORCE SYSTEMS COMMAND
UNITED STATES AIR FORCE
HANSCOM AIR FORCE BASE, MASSACHUSETTS 01731-5000

SPONSORED BY
Defense Advanced Research Projects Agency
Nuclear Monitoring Research Office
ARPA ORDER NO. 5299

MONITORED BY
Geophysics Laboratory
Contract No. F19628-87-K-0034



This technical report has been reviewed and is approved for publication.

JAMES F. LEWKOWICZ
Contract Manager
Solid Earth Geophysics Branch
Earth Sciences Division

JAMES F. LEWKOWICZ
Branch Chief
Solid Earth Geophysics Branch
Earth Sciences Division

FOR THE COMMANDER

DONALD H. ECKHARDT, Director
Earth Sciences Division

4

GL-TR-89-0153

AD-A215 943

# Investigating the Effects Fracture Systems Have on Seismic Wave Velocities at the Lajitas, Texas Seismic Station

Victoria L. Sandidge-Bodoh

Southern Methodist University
Department of Geological Sciences
Dallas, TX 75275

1 May 1989

Final Report
3 March 1987 - 2 March 1989

APPROVED FOR PUBLIC RELEASE; DISTRIBUTION UNLIMITED



GEOPHYSICS LABORATORY
AIR FORCE SYSTEMS COMMAND
UNITED STATES AIR FORCE
HANSCOM AIR FORCE BASE, MASSACHUSETTS 01731-5000

SPONSORED BY
Defense Advanced Research Projects Agency
Nuclear Monitoring Research Office
ARPA ORDER NO. 5299

MONITORED BY
Geophysics Laboratory
Contract No. F19628-87-K-0034

The views and conclusions contained in this document are those of the authors and should not be interpreted as representing the official policies, either expressed or implied, of the Defense Advanced Research Projects Agency or the U.S. Government.

This technical report has been reviewed and is approved for publication.

JAMES F. LEWKOWICZ
Contract Manager
Solid Earth Geophysics Branch
Earth Sciences Division

JAMES F. LEWKOWICZ
Branch Chief
Solid Earth Geophysics Branch
Earth Sciences Division

FOR THE COMMANDER

DONALD H. ECKHARDT, Director
Earth Sciences Division

This report has been reviewed by the ESD Public Affairs Office (PA) and is releasable to the National Technical Information Service (NTIS).

Qualified requestors may obtain additional copies from the Defense Technical Information Center. All others should apply to the National Technical Information Service.

If your address has changed, or if you wish to be removed from the mailing list, or if the addressee is no longer employed by your organization, please notify AFGL/DAA, Hanscom AFB, MA 01731-5000. This will assist us in maintaining a current mailing list.

Do not return copies of this report unless contractual obligations or notices on a specific document requires that it be returned.

| 8a. NAME OF FUNDING / SPONSORING ORGANIZATION | 8b. OFFICE SYMBOL (If applicable) | 9. PROCUREMENT INSTRUMENT IDENTIFICATION NUMBER | | | |
|---|---|---|---|---|---|
| DARPA | NMRO | F19628-87-K-0034 | | | |
| 8c. ADDRESS (City, State, and ZIP Code) | | 10. SOURCE OF FUNDING NUMBERS | | | |
| 1400 Wilson Blvd.<br>Arlington, VA 22209-2308 | | PROGRAM ELEMENT NO. | PROJECT NO. | TASK NO. | WORK UNIT ACCESSION NO. |
| | | 61101E | 7A10 | DA | CP |

**11. TITLE** *(Include Security Classification)* Investigating the Effects Fracture Systems Have on Seismic Wave Velocities at the Lajitas, Texas Seismic Station

**12. PERSONAL AUTHOR(S)** Victoria L. Sandidge-Bodoh

| 13a. TYPE OF REPORT | 13b. TIME COVERED | 14. DATE OF REPORT (Year, Month, Day) | 15. PAGE COUNT |
|---|---|---|---|
| Final | FROM 3Mar87 TO 2Mar89 | 1 May 1989 | 182 |

**16. SUPPLEMENTARY NOTATION**

| 17. COSATI CODES | | | 18. SUBJECT TERMS (Continue on reverse if necessary and identify by block number) |
|---|---|---|---|
| FIELD | GROUP | SUB-GROUP | Lajitas, Seismic, Velocities, Fractures |
| | | | |
| | | | |

TABLE OF CONTENTS

LIST OF ILLUSTRATIONS

## LIST OF TABLES

Table | Page

# ACKNOWLEDGEMENTS

This research was supported in part by the Department of Geological Sciences, Southern Methodist University; the Institute for the Study of Earth and Man; and by the Defense Advanced Research Project Agency, grant MDA972-88-K-0001, to Eugene T. Herrin.

Thanks to my adviser, Eugene T. Herrin, and the rest of my committee, Patty E. Murtha (ARCO), Brian W. Stump, and Vicki L. Hansen for their valuable contributions towards the completion of this project. I give special thanks to ARCO at Plano, Texas, for the use of their rock physics lab under the supervision and guidance of Mike Batzle, their Macintosh software for rose diagrams, and their XRD analysis done on the Santa Elena limestone samples by Micheal Kelton. I also thank Leon Thomsen, for helpful suggestions concerning fracture density and elastic moduli; Tom Goforth, for lending geophones from Baylor University; and Steve Flint, Paul Golden, and Chris Hayward for their assistance in the field. Finally, I thank my family and friends for their constant support, encouragement and patience.

I dedicate this thesis to my loving husband, Leon F. Bodoh, Jr.; and to the memory of my grandma, Oda Mae Sandidge, who is very close to my heart.

# I. Introduction

Refraction data collected at the Lajitas site in 1983 yielded *in situ* P-wave velocities of 3.5 km/s for the Santa Elena limestone. A regional refraction survey conducted with a Vibroseis and a receiver line extending north from the seismic station to just a few miles south of Alpine along Highway 118 yielded P-wave velocities of 3.5 km/s for the first 160 meters below the earth's surface and 4.7 km/s for the next 1350 meters (Figure 1.1) (Golden et al., 1985). Three local refraction surveys: 1) an 1100 meter long reversed refraction spread with a dynamite source (line oriented NNW/SSE), 2) a 38 meter long reversed refraction spread with a sledge hammer and aluminum plate source (line oriented E/W), and 3) a down-hole survey at a 100 meter depth with sledge hammer and plate source (shots at three meter intervals extending out to approximately 80 meters south of borehole) yielded average P-wave velocities of 3.477 ± 0.05 km/s, 3.2 ± 0.05 km/s, and a mean apparent P-wave velocity of 3.485 km/s (deviation = ±0.16 km/s) respectively (Figure 1.2) (Reinke and Logan, 1983).

Based on the data accumulated by Sorrells (1961), Gardener (1974), and Clark (1966) concerning P-wave velocities in homogeneous limestones, the *in situ* P-wave velocities for

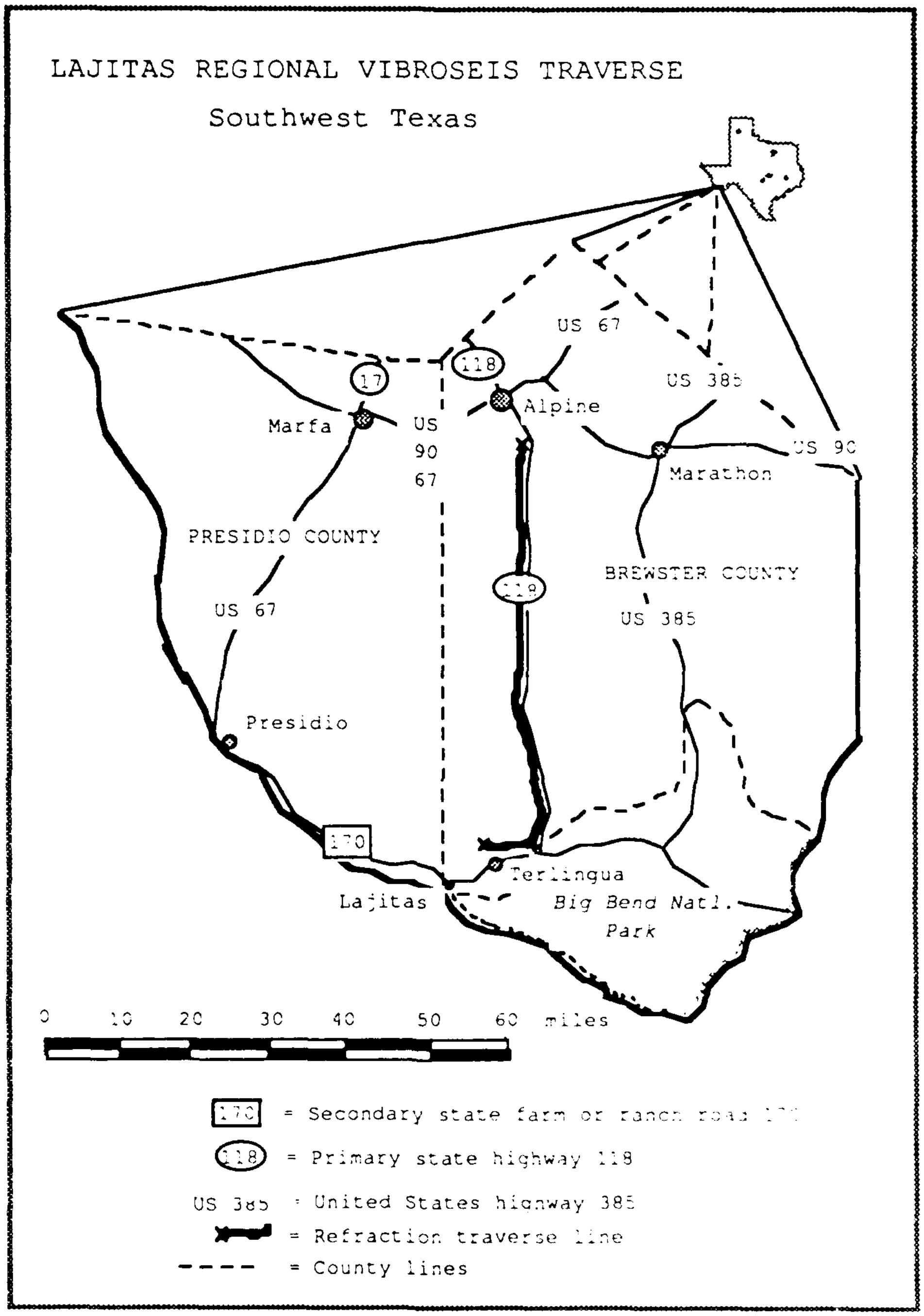


Figure 1.1 Regional refraction survey traverse.

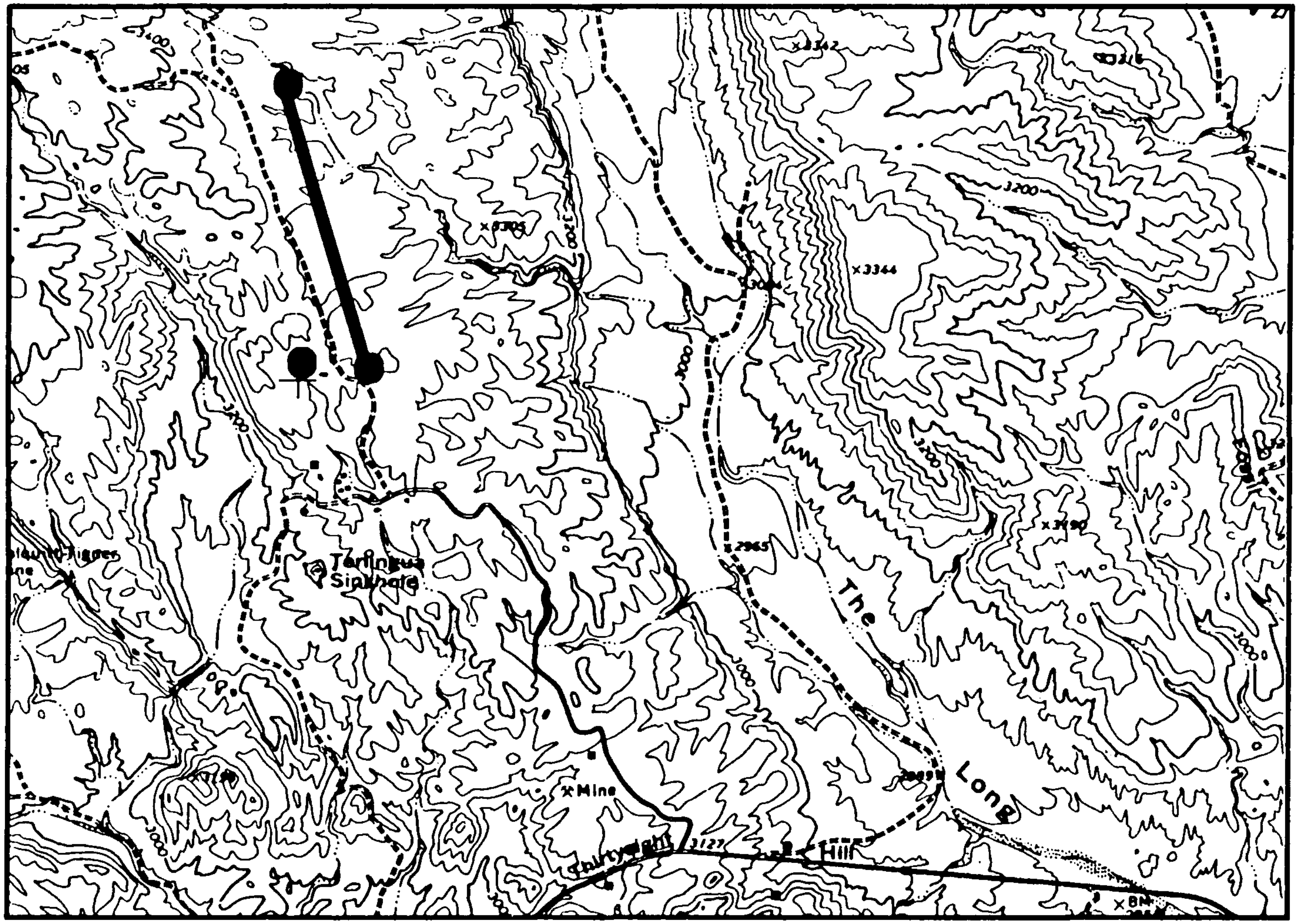


Figure 1.2 Location of local refraction survey traverses. North points to the top of the page and 1 cm equals approximately 0.23 km. (From Reinke and Logan (1983).)

the Santa Elena limestone were expected to average approximately 5.5 km/s (Figure 1.3).

Sorrells measured P-wave velocities through three mutually perpendicular cylindrical plugs cut from each of fourteen carbonate rock samples from different localities. Each set of plugs measured 2.54 - 7.62 cm in length and 2.54 cm in diameter. For wavelengths between 10 and 20 millimeters, the measured longitudinal wave velocities through each plug varied with changing hydrostatic pressures ranging from 1 - 2000 bars. At one atmosphere, velocities varied from 4.65 to 6.36 km/s in the samples and as much as thirty percent azimuthally in individual samples. Sorrells also examined the variations in the petrographic, physical, and mineralogical properties of the fourteen rock samples. Based on correlations between the velocity data and the petrographic, physical, and mineralogical variations Sorrells (1961) concluded that: 1) relatively large decreases in velocity correlate with relatively minor increases in porosity ranging from 0 - 3 percent; 2) increased pressure reduces the porosity thus causing a velocity change; 3) a range of 0 - 30 wt % in clay content decreases P-wave velocities; 4) an increase in dolomite content produces a slight increase in longitudinal wave velocity; 5) linear rock fabrics visible in thin section possess anisotropic properties; and 6) bulk density increases as P-wave velocity increases.

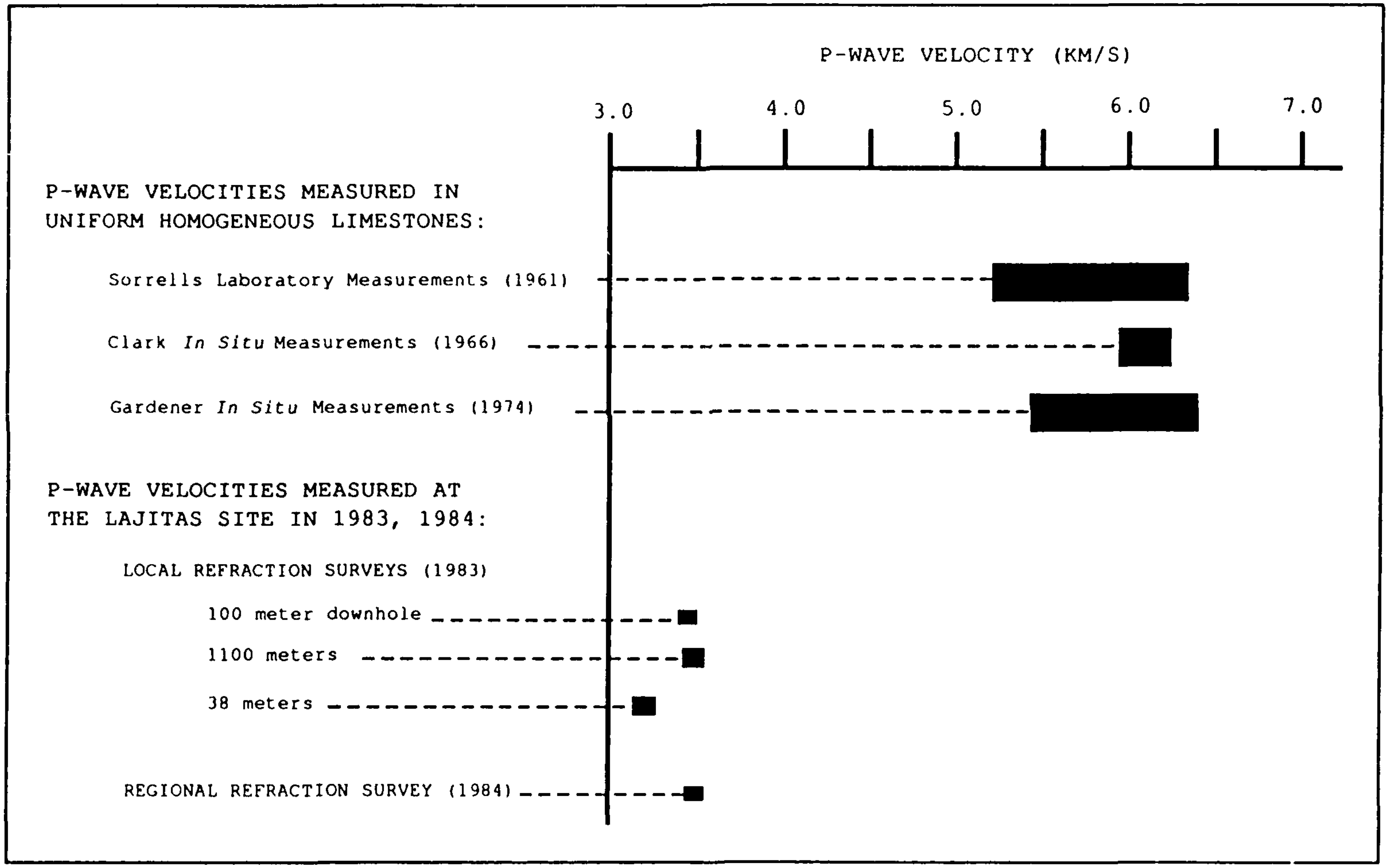


Figure 1.3 Illustration showing the contrast between P-wave velocities measured in fractured homogeneous Santa Elena limestone at the Lajitas site, and previous in situ and laboratory measurements.

Excluding samples with high clay content and vuggy porosity yields a bulk density range of 2.60 - 2.68 gm/cc and corresponding P-wave velocities ranging from 5.0 - 6.5 km/s for the Sorrells data. Gardener (1974) documents that *in situ* velocities increase with increasing density and in the 2.60 - 2.68 gm/cc bulk density range *in situ* P-wave velocity ranges from approximately 18000 - 21000 ft/s (or 5.49 - 6.40 km/s). Clark (1966) also shows that *in situ* P-wave velocities range from 5.5 - 6.5 km/s for homogeneous limestone. Therefore, *in situ* velocity measurements correspond to laboratory velocities for uniform homogeneous limestones.

Laboratory velocity measurements vary significantly with the nature of saturating fluids (Gardener et al., 1974; King, 1966; Wyllie et al., 1956, 1958; Elliot and Wiley, 1975); and because laboratory observations reveal that P- and S-wave velocities depend strongly on porosity and saturation conditions, Toksöz et al. (1976) raise several questions:

1) What effects do pore geometry and saturating fluids (such as gas, water, or oil) have on seismic velocities?

2) Can the pore geometry and saturation state be determined given the seismic velocities?

3) Given these rock models, for seismic velocities under reservoir conditions, how might one determine from seismic data the nature of the saturating fluids (e.g., gas, oil, brine)?

Several theoretical models have been formulated to answer these questions. Biot (1941) introduced a semiintuitive formulation of the equations of elasticity for a porous aggregate. Most importantly, he recognized that in a solid, the pore fluid pressure and volume increment are state variables, in addition to stress and strain. Gassmann (1951) expressed these variables in terms of the separate properties of the pore fluid and solid material. In 1981, Burridge and Keller carefully derived the basic equations first assumed by Biot and Gassmann and clarified the corresponding valid frequency regimes. A number of models (e.g., Eshelby, 1957; Bristow, 1960; Kuster and Toksöz, 1974; O'Connell and Budiansky, 1974; Budiansky and O'Connell, 1976) sharing the minimal assumptions of Biot-Gassmann theory concerning pore geometry emerged, attempting to provide stronger predictions on the elasticity of aggregates through stronger assumptions about the microscopic geometry of the constituents. Thomsen (1985) extended the standard Budiansky and O'Connell (1980) model theory for dilute concentrations of fluid heterogeneities, to high concentrations of pores and fractures, and simultaneously preserved explicit consistency with the predictions of Biot-Gassmann theory for low-frequency elastic moduli of porous rocks. The predictions of Biot-Gassmann theory are as follows: 1) the shear modulus of an unsaturated rock equals that of the same rock saturated with liquid, and 2) the difference between the unsaturated and saturated bulk modulus is a defined amount. Laboratory observations of the "Biot slow wave" provided support for the validity of other predictions made by Biot-Gassmann theory (Plona, 1980). These other predictions relate unsaturated moduli to saturated. Formal consideration of these theoretical models will be delayed until chapter V.

Fractures in the Santa Elena limestone lower the expected wave velocities in the first 160 meters. The objective of this research is to investigate the effects of fractures on seismic wave velocities at the Lajitas site with particular emphasis on macrofracture density and orientation and their effects on *in situ* P- and S-wave velocities. In determining these effects, we examine the relationship between several measurements of fracture orientation, porosity, and density and *in situ* P-, Sv-, and Sh-wave velocities at varying azimuths. Matrix and whole rock parameters, estimated from laboratory measurements of P- and S- wave velocities, pore porosity, dry bulk and saturated rock densities, and grain density for the Santa Elena limestone, aid in examining this relationship. The laboratory and *in situ* velocity measurements provide the parameters necessary for the application of the theoretical models relating pore porosity, fracture porosity and fracture density to seismic wave velocity.

First, a brief description of the geologic setting is given. Then, a discussion concerning the spatial distribution of fractures at the macroscopic scale, with emphasis on macrofracture density and orientation follows in section three. Next, attention is focused on microscopic inhomogeneities (such as vuggy porosity, preferentially oriented microfractures, compositional variations, etc.) possibly affecting *in situ* seismic velocities. The term *macroscopic* refers to structure and inhomogeneities easily observed in outcrop with the unaided eye, to regional structure and lithologic changes spanning terrain distinguishable from aerial and satellite photos with scales averaging approximately 1:22,000. Structural and mineralogical heterogeneities, seen only through a microscope, to hairline fractures and grain-sized mineralogical components barely visible to the unaided eye, define the term *microscopic*. Section five investigates the relationship between *in situ* P- and S-wave velocity and fracture orientation and utilizes the Biot-Consistent model to estimate the average fracture porosity and density along each seismic refraction spread in the survey area. Finally, section six contains a brief summary and conclusions. Appendix A shows the association between all figures containing maps.

## II. Geologic Setting

The region of concern encompasses the Lajitas seismic station located approximately 32 km northeast of Lajitas, a small village near the Rio Grande river in southwest Texas (Figure 2.1). Situated in the northeast quarter of the 7 1/2 minute Amarilla Mountain Quadrangle, the study area covers approximately 5 $km^2$. The region's southern border begins about 1 km north from FM 170. The edge of the Long Draw's western floodplain marks the region's eastern border.

The regional structure can best be described as a fractured antiform caused by a lacolithic intrusion of unknown depth during the Tertiary (Herrin, personal communication). On a macroscopic scale the predominant exposed rock in the region is lithologically homogeneous Santa Elena limestone (Figure 2.2). Examination of infrared satellite and air photos reveals a few grabens and a synclinal structure with most recent units composed of macroscopically unfractured shale. Along the perimeter of the study area, shale cuestas that tilt upward toward the central part of the region encircle the exposed limestone terrain. The Amarilla Mountain 7 1/2 minute topographic quadrangle shows a gradual rise in elevation where the shale beds flank the Santa Elena. The change in elevation increases where Santa Elena limestone

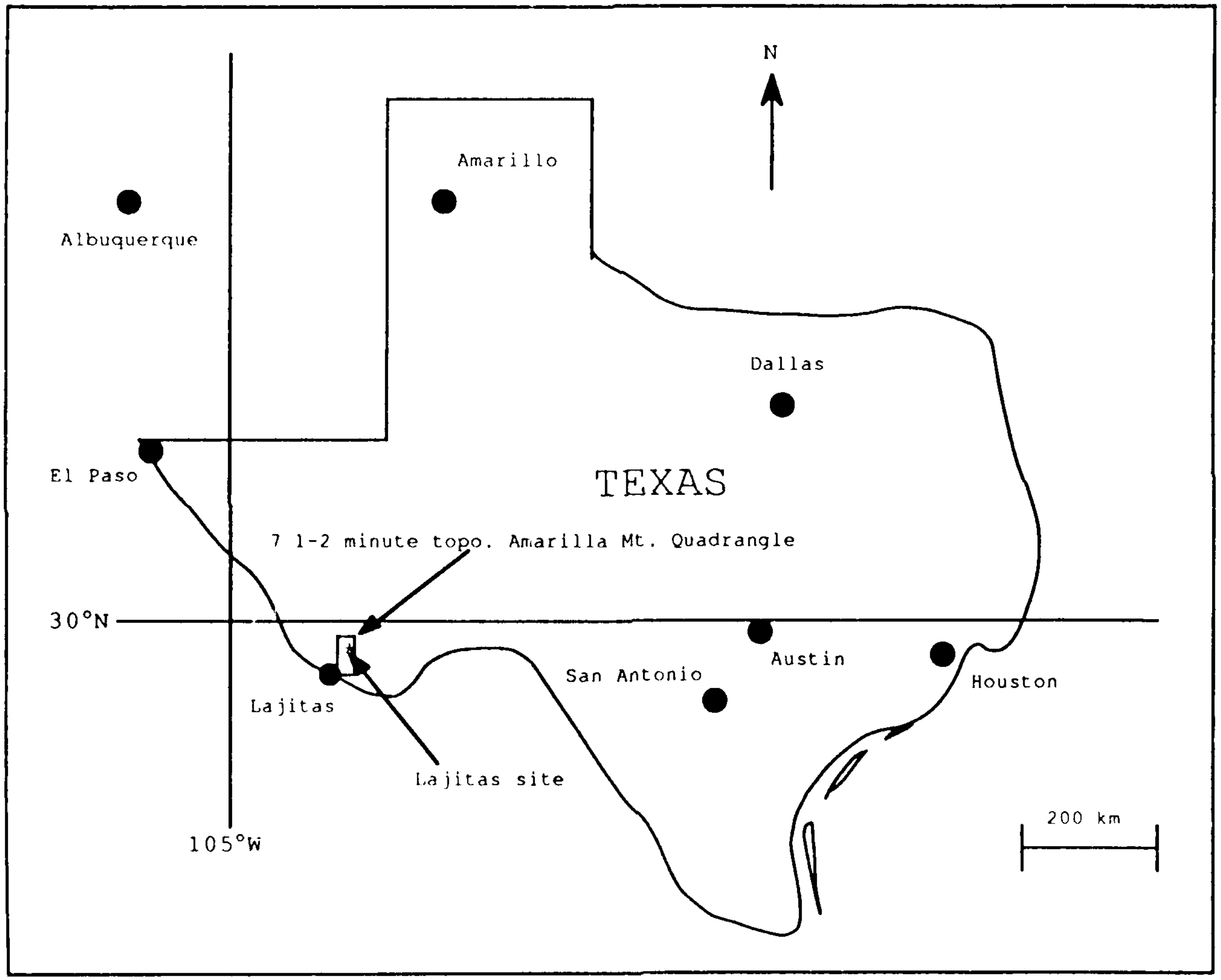


Figure 2.1 Location of study area.

GEOLOGIC MAP OF THE LAJITAS REGION IN SOUTHWEST TEXAS

SCALE: 1 cm approximately equals 1 km

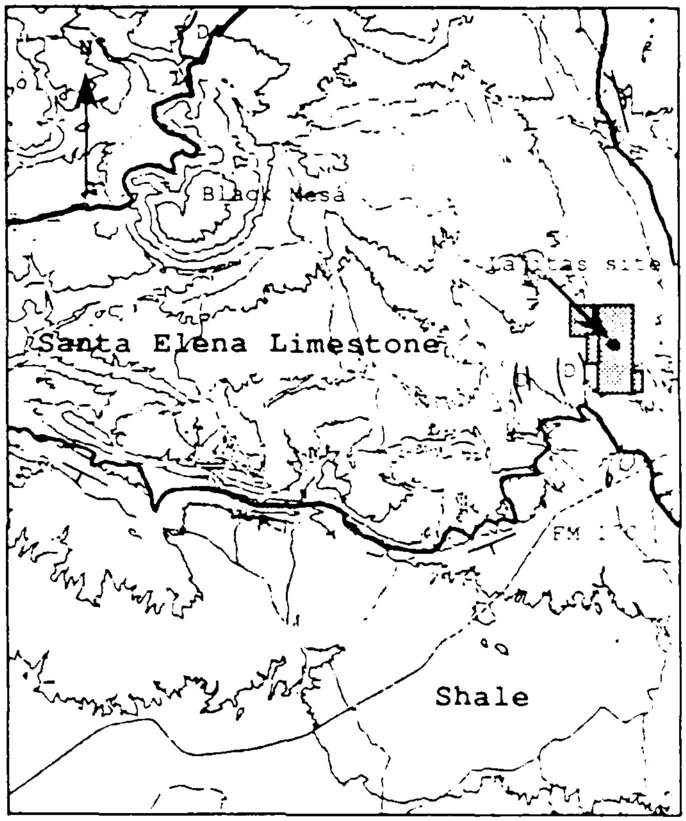


Figure 2.2 A geologic sketch of the Lajitas area (drawn from infrared photo and 7 1/2 minute Amarillo topographic quadrangle).

is exposed. Just outside the immediate vicinity, a few Tertiary intrusions puncture the horizontal limestone beds at the surface. Lacolith intrusions upwarped limestone at Black Mesa (Figure 2.2) and probably caused the Soltario uplift located about 14 miles to the northwest (Maxwell, 1971).

Fractures cut the Santa Elena Formation and possibly the Sue Peaks and Del Carmen Formations located stratigraphically below the Santa Elena Formation. The air and infrared satellite photos reveal distinct fracture systems of undetermined depth riddling the exposed Santa Elena limestone (Figure 2.3). The fractures could be open to the water table about 1500 feet below the surface. Because of the region's hot and arid climate, it is likely that these macrofractures are air-filled.

Shale, marl, and thin marly limestone ledges make up the Sue Peaks Formation and massive thick bedded limestones mainly compose the Santa Elena and Del Carmen Formations (Maxwell, 1971). Local refraction surveys conducted in the Lajitas area show that the Santa Elena/Sue Peaks and Sue Peaks/Del Carmen interfaces reach depths of approximately 245 and 320 - 335 meters below the surface respectively (Figure 2.4)(Alden, 1983; Reinke and Logan, 1983). All three formations are located within the Comanche Series (Maxwell, 1971).

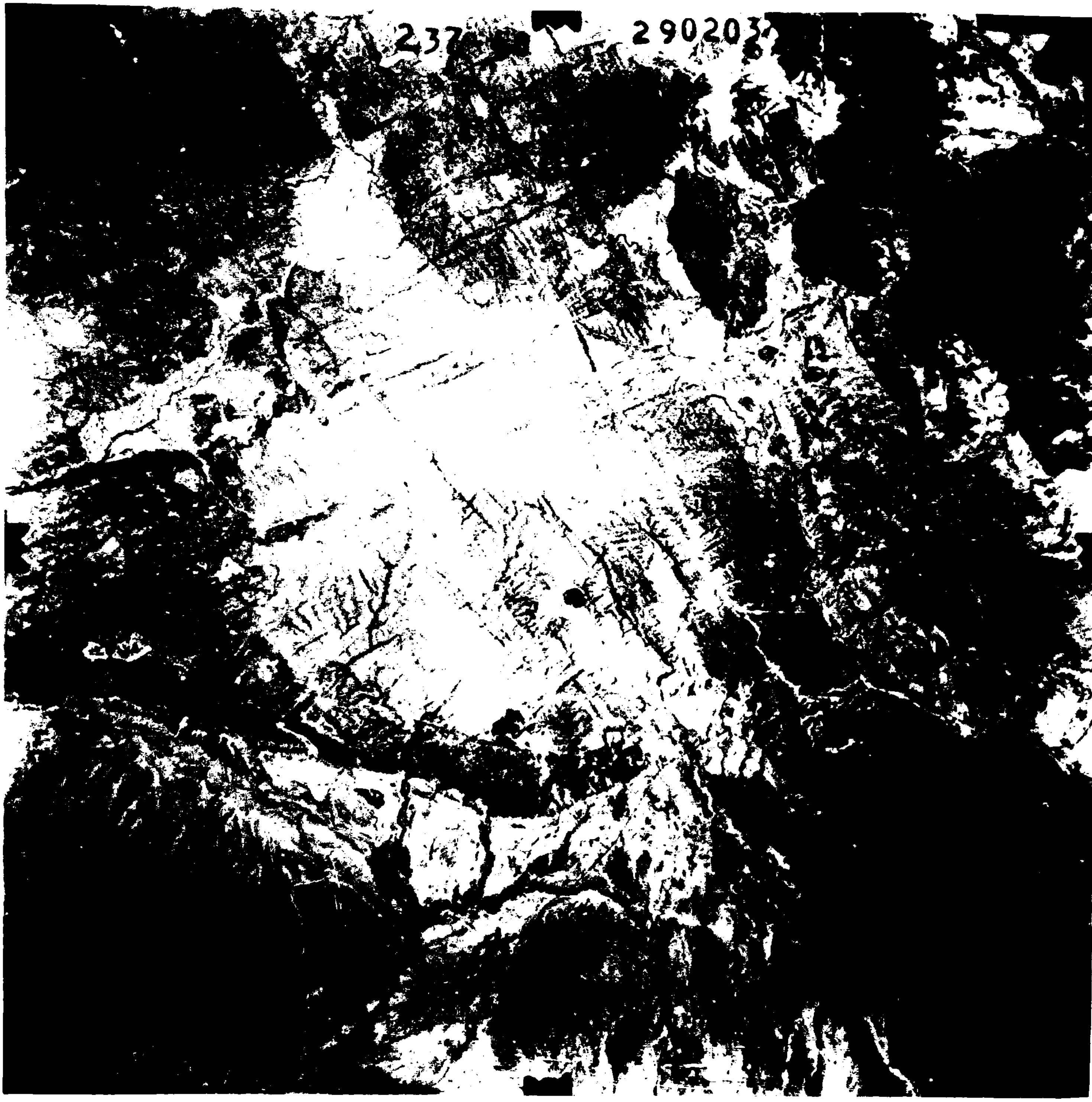


Figure [illegible] The [illegible] small graben and [illegible] site of the La[illegible] [illegible] of the [illegible]

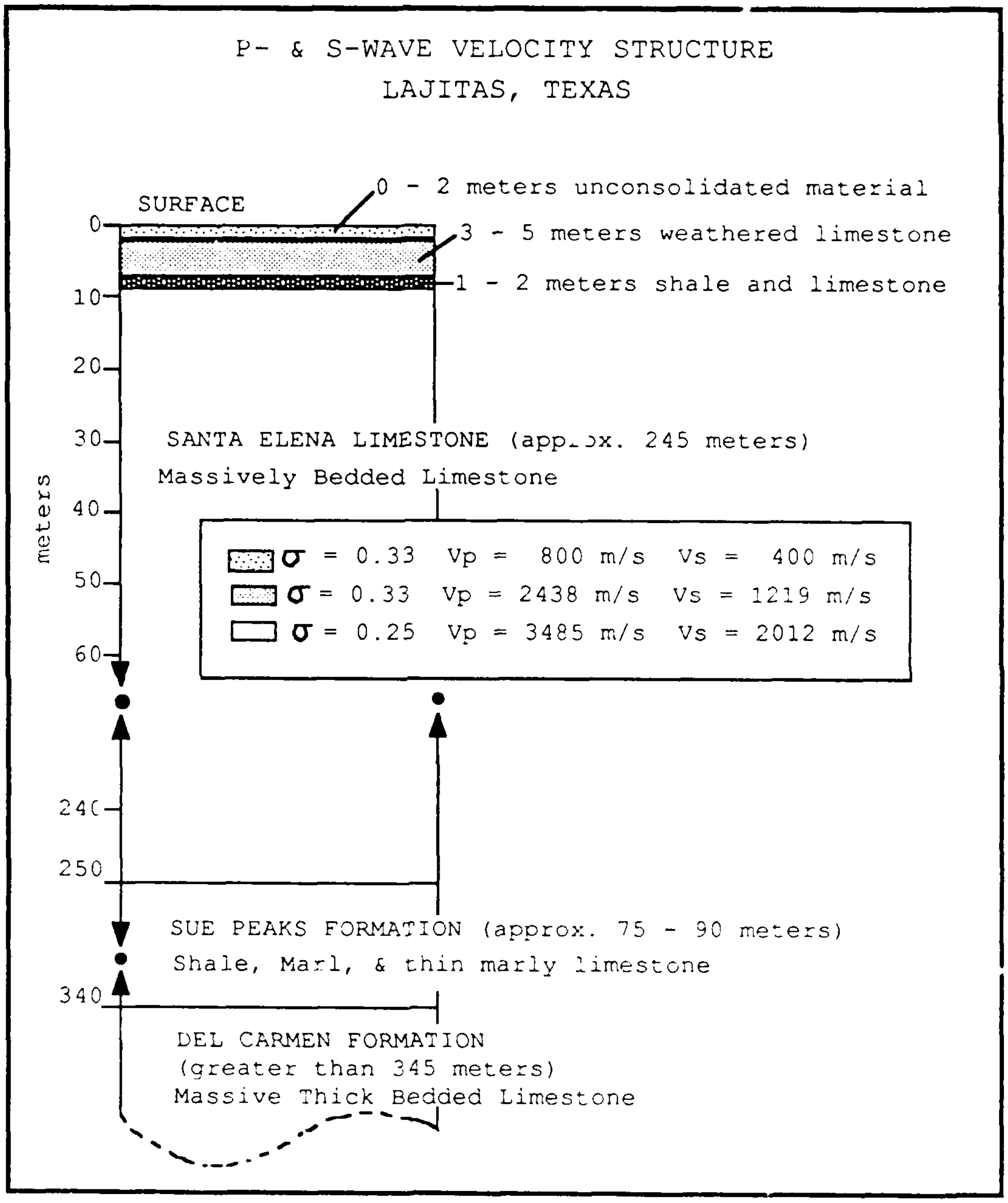


Figure 2.4. The approximate stratigraphic and seismic profile at the Lajitas site in southwest Texas. (Drawn from Alden (1983).)

## III. Preliminary Map and Field Work

The main preliminary map and field work objectives are to 1) determine fracture distribution and orientation both at a macroscopic and microscopic scale; and 2) collect oriented Santa Elena hand specimens. Knowledge of fracture orientation and distribution helps in defining possible anisotropic symmetries and consequently aids in planning refraction surveys such that proposed symmetries can be verified or discarded. Comparison of laboratory measurements of physical properties in oriented hand specimens aids in defining the homogeneity and elasticity of the Santa Elena rock matrix.

Measurements of fracture orientation at both a microscopic and macroscopic scale aid in estimating possible anisotropic symmetries defined by open fracture sets. An isotropic and homogeneous rock matrix possessing open and aligned vertical fractures restrains effective seismic anisotropy to a simple hexagonal symmetry (Crampin et al., 1984; Crampin, 1984). With the axis of symmetry oriented at right angles to the vertical, this model can be thought of as a transversely isotropic medium rotated 90 degrees from the horizontal. Note also that subvertical fractures cause negligible change in the symmetry just mentioned (Booth et al., 1986). If anisotropic symmetries defined by microscopic and macroscopic fractures mirror one another as Booth et al. (1986) claim, then anisotropic symmetries determined in the lab accurately predict corresponding anisotropic symmetries *in situ;* provided the rock matrix is isotropic and homogeneous.

Testing the homogeneity of the Santa Elena rock matrix requires the collection of several oriented rock specimens from random locations within the vicinity of interest. A comparison of physical rock properties for each collected specimen aids in determining the 'degree' of homogeneity. Physical properties, such as porosity, density, mineralogical composition, and P- and S-wave velocity can be measured in the laboratory. Measuring P- and S-wave velocity for each sample along several propagation paths differing in orientation aids in determining how the physical properties affect the composite elastic constants for the medium.

Planning the geometrical arrangement of seismic refraction lines requires the knowledge of fracture distribution and orientation. To observe slight anisotropic effects in isotropic and homogeneous material (i.e., a 2 percent difference in wave velocity), a source must generate wavelengths much greater than the fracture size and the separation distance between fractures (Backus, 1962). Because longitudinal wave velocities decrease to a minimum as the angle of incidence to a fracture plane approaches 90 degrees, one must consider fracture orientation when planning the geometrical arrangement of seismic refraction lines (Lynn and Thomsen, 1986). Also, because tensional and compressional stresses open and close fractures, aligning refraction lines parallel and perpendicular to traces of vertical fracture sets provides a means to determine the current stress regime (Rai and Hanson, 1986). Knowledge of accessible areas that minimize terrain corrections and geophysical field work is also valuable.

## Methodology

Determination of Macrofracture Distribution and Orientation. Compilation of a detailed lineation map representing fracture lineations at the surface by inspecting stereo pairs and a high resolution infrared photo enables the measurement of macrofracture distribution and orientation. Observations in the field both above and below the surface also reveal macroscopic fracture plane inclinations. Pepper's Mine, located near the Lajitas station, gives access to the subsurface, therefore allowing the measure of fracture plane orientations at depth with the use of a Brunton compass. The infrared satellite photo and the 7 1/2 minute Amarilla Mountain topographic quadrangle provides the means to construct a lineation map representing the orientation, size, and distribution of macrofracture traces exposed at the surface. Using mylar and rapidograph to trace visible macrofracture patterns from the infrared photo produces an accurate representation of fracture sets. Methods discussed in Chapter 5 of Compton's 1962 Manual of Field Geology suffice in determining scale and bearing on the constructed lineation map. Upon completion of the lineation map, one directly measures macrofracture separation distances and orientations using a protractor and scale. Because fracture orientation varies with geographical location, one must select unit volumes representative of macrofracture orientation for each locality of interest. Rose diagrams facilitate examination of dominant fracture orientations for each unit volume with errors in orientation less than 5 degrees.

Determination of Microfracture Distribution and Orientation. Measuring orientation of hairline fractures in several oriented *in situ* Santa Elena hand specimens yields dominant microfracture trends. Using a Brunton compass, one can measure orientation of microfractures within 3 degrees before extracting a sample. Rose diagrams document the spatial change in dominant fracture orientations.

Collection of Oriented Hand Specimens. From each sample, laboratory work requires analysis of three cylindrical plugs measuring 2.54 cm in diameter and 3 - 5 cm in length. Due to torsional motion in the coring bit, a sample riddled with open fractures reduces the chance of recovering plugs of sufficient length. Hence, one must choose samples large enough and with as few fractures as possible. Also, plugs having few or no fractures more closely reflect the nature of the rock matrix. One can orient samples using the methods of Prior et al. (1987).

## Observations

There is a correlation between microscopic and macroscopic fracture orientation and distribution. The broken-up character of the Santa Elena limestone (Figure 2.3) corresponds to dense brittle fracturing observed during geologic reconnaissance at the smaller scale in outcrop.

At the macroscopic scale, fracture traces unaffected by topography indicate vertical fracturing. In addition, tops and bottoms of massive stratigraphic layers following topographic contours suggest horizontal bedding (Billings, 1972). Three distinct fracture systems exist (Figure 3.1). However, rose diagrams from areas I, IIa, IIb, III, and IV show two general macrofracture trends approximately at right angles to one another--NNW and ENE (Figure 3.2a-e). Figure 3.2f shows a composite of fracture orientations for all five areas. Fracture separation distance ranges from 35 - 40 meters.

The Santa Elena's "cobblestone" (or "blocky") appearance suggests subvertical to vertical fracturing and horizontal parting along bedding planes. Also, a characteristic cubic or rectangular hand specimen shape implies vertical fracturing and horizontal parting at the microscopic scale. Two sets of fractures, NNW and ENE, dominate at the microscopic scale. Rose diagrams (Figure 3.3a-g) represent the general

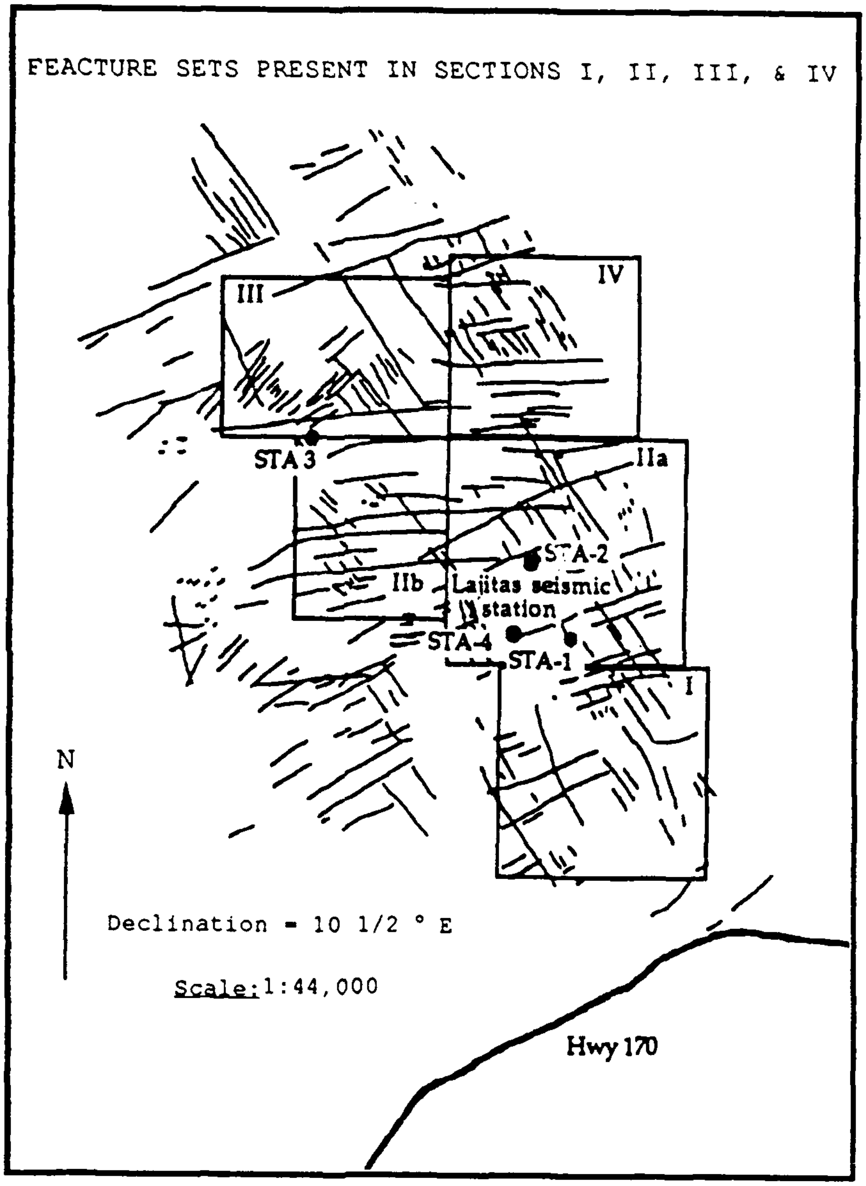


Figure 3.1  Detailed lineation map covering area of study.

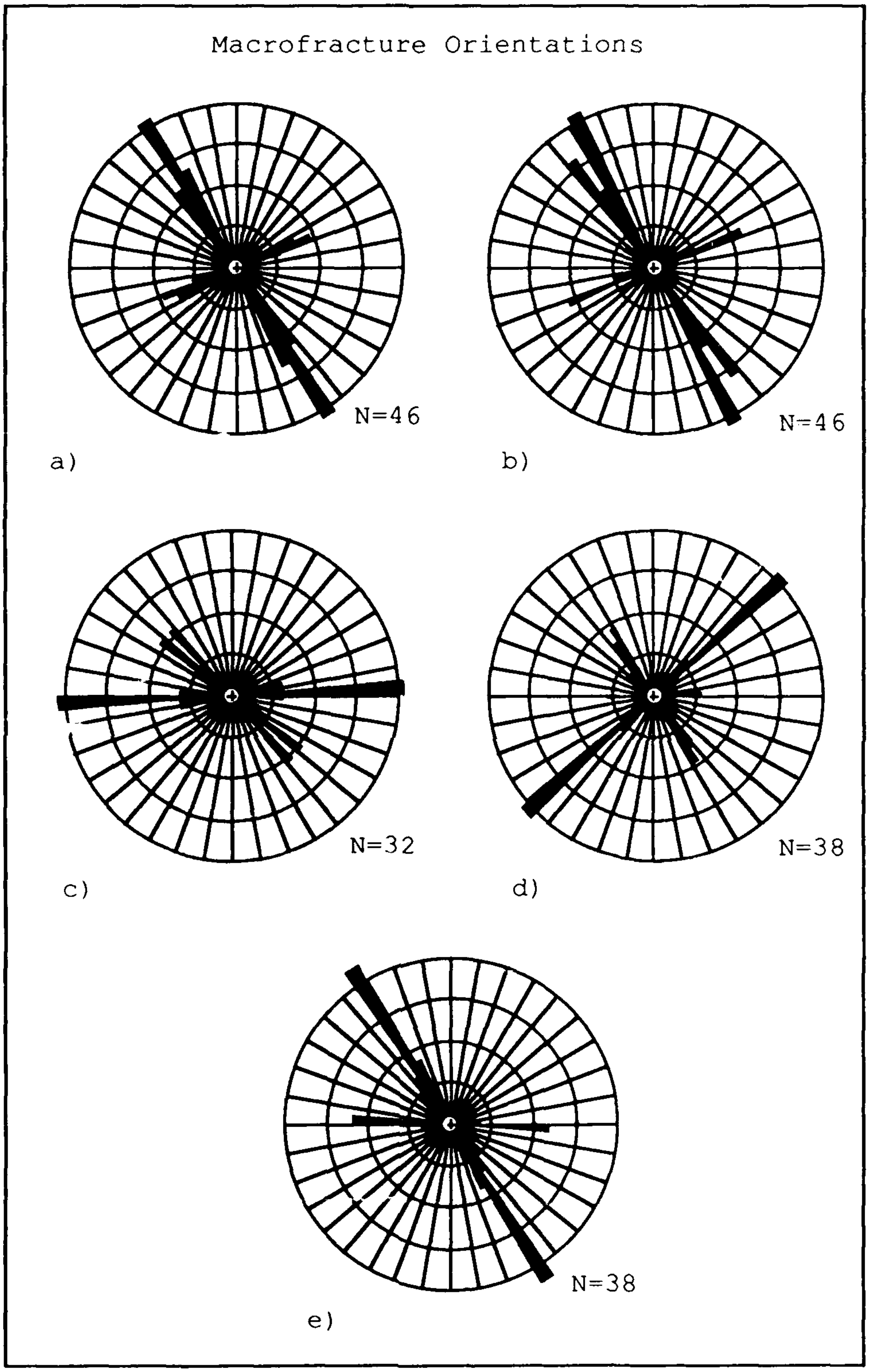


Figure 3.2a-e Observed strikes of macrofractures in unit areas a) I, b) IIa, c) IIb, d) III, and e) IV.

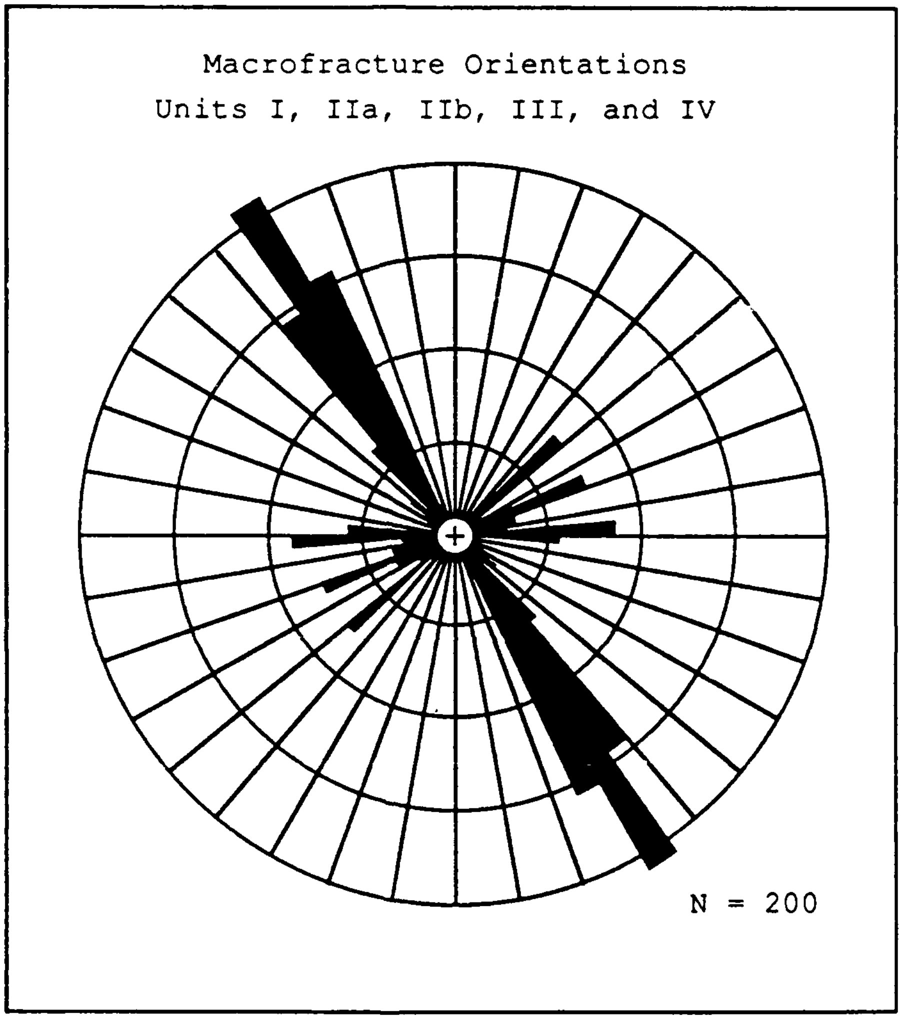


Figure 3.2f Cummulative representation of observed macrofracture strikes in areas I through IV.

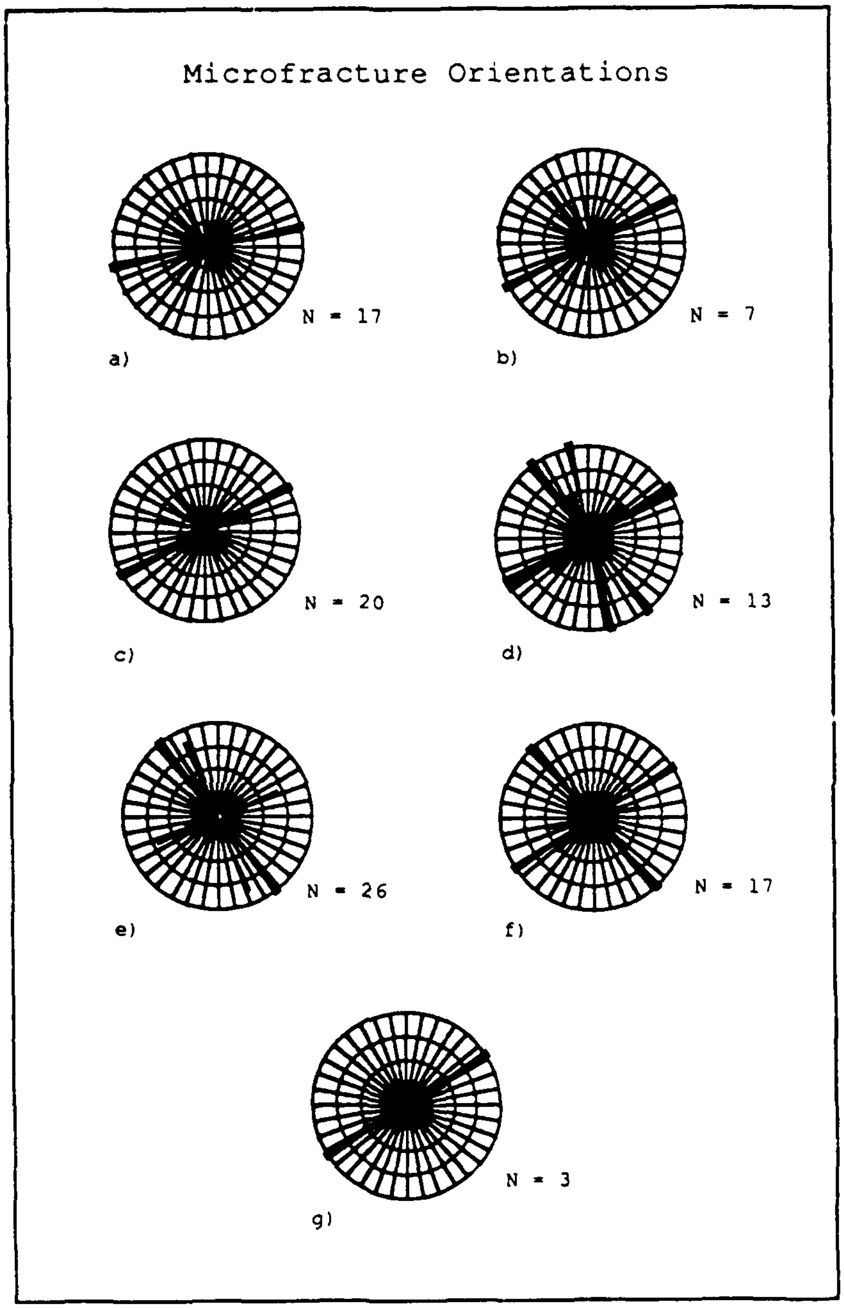


Figure 3.3a-g Observed strikes of microfractures in samples a) VLS-1, b) VLS-2, c) VLS-3, d) VLS-5, e) VLS-6, f) VLS-7, and g) VLS-8.

trends of hairline fracture planes in each sample. Figure 3.3h shows a composite of all fracture plane strikes at the microscopic scale. Thick caliche cover on sample VLS-4 and VLS-8 camouflaged a dense distribution of hairline fractures visible only on cutting the samples. Consequently, only a few fractures could be measured from sample VLS-8. No fractures were measured from sample VLS-4. The fracture separation distance at the microscopic scale ranges from 2.5 - 30.5 cm.

Pepper's Mine, once mined for its mercury, provides access to the subsurface (Figure 3.4). A dense distribution of vertical fractures lines the tunnel walls. The tunnels follow fractures oriented with either of the two general trends measured from the lineation map and oriented hand specimens (Figure 3.5). Excluding frequent horizontal parting along bedding planes, most fractures have subvertical to vertical inclinations. Although most bedding is horizontal, in a few areas, undulating laminated sandy limestone beds ranging from 10 - 15 cm in thickness and massive "pinched out" beds cause a variation in bedding dip from 14° to 31°. Fractures and partings between bedding planes are healed and partially healed with sparry calcite and cinnibar fillings. Fillings separating beds range from 7 - 30 cm in thickness, whereas fracture plane fillings range from 0 - 7 cm in thickness. Because of possible blast induced effects, fracture separation distance in the mine was not estimated.

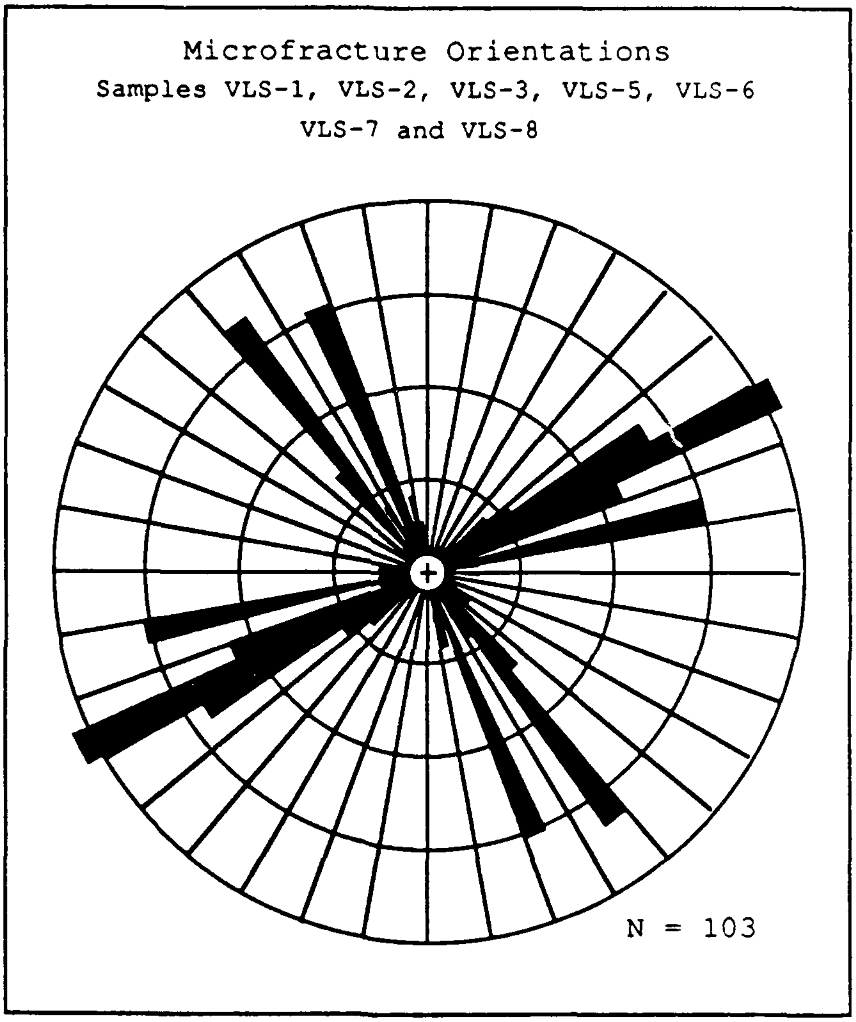


Figure 3.3h Cummulative representation of observed microfracture strikes in samples VLS-1, VLS-2, VLS-3, VLS-5, VLS-6, VLS-7 and VLS-8.

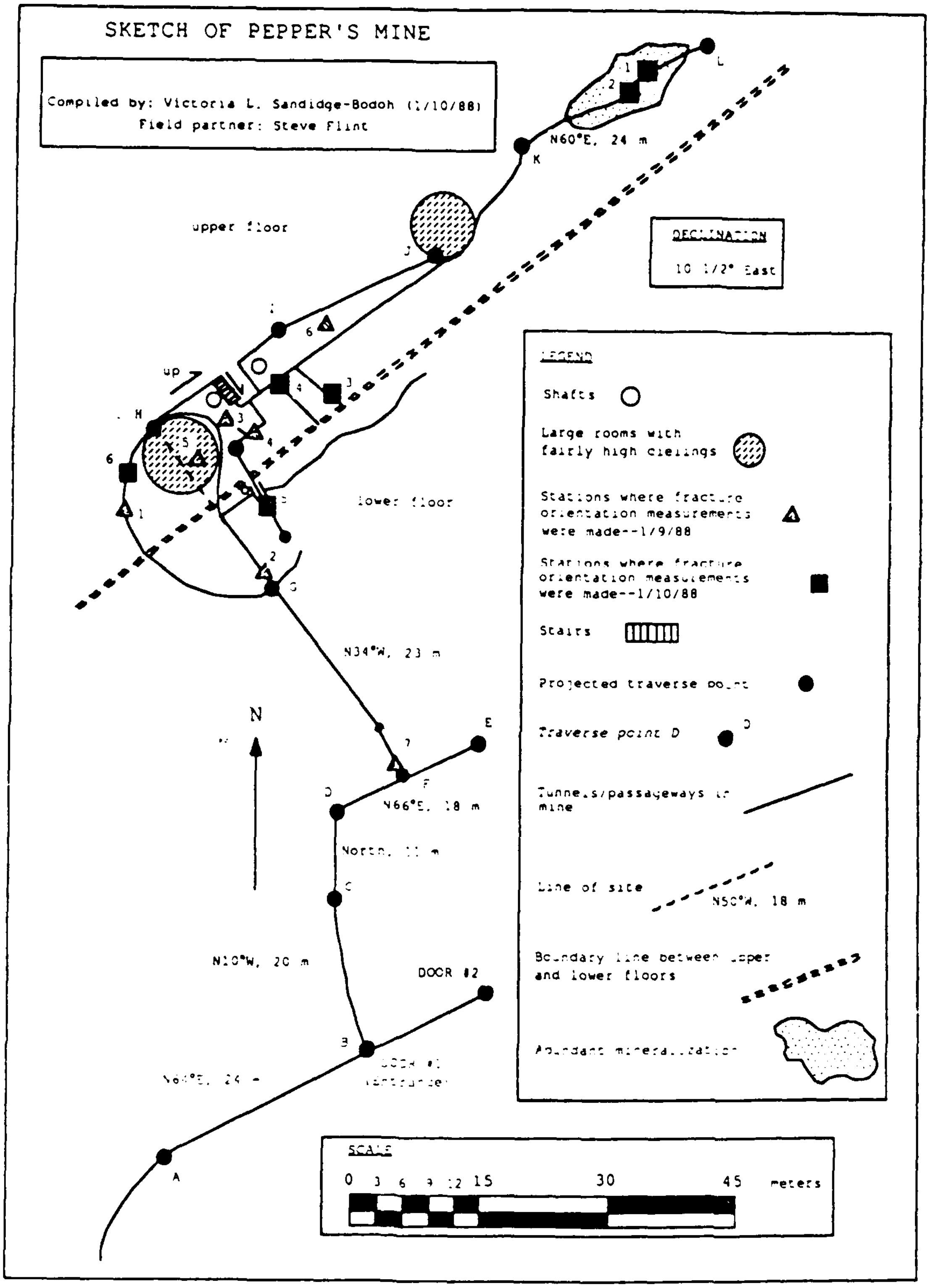


Figure 3.4 Map of Pepper's Mine.

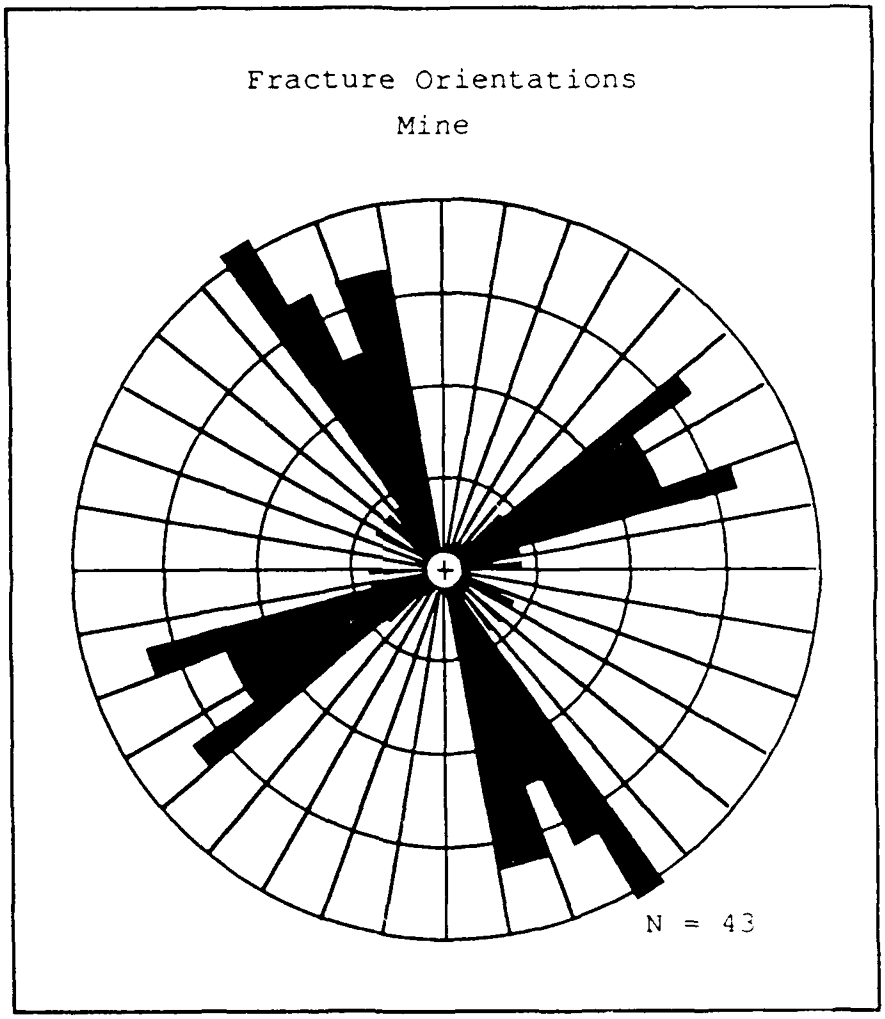


Figure 3.5 Observed strikes of fractures in Pepper's Mine.

The Santa Elena is comprised primarily of calcite and secondary clay, silica, and trace amounts of pyrite. Samples range in color from buff- to yellow- to violet-white and in some cases two to three colors intermingle, giving a marbled appearance. Bioturbation caused this intermingling. The texture is soft (H = 3 - 3 1/2), fine-grained and massive--a few samples look chalky. Fossil content varies from approximately 0 to 5 percent. Observed Nerinied (class gastropoda), Caprinid (class pelecypoda), ammonite and foraminifera fossils show sparry calcite replacement. However, silicification was observed in several rudistids (phylum echinodermata). Fresh cut surfaces revealing holes less than 0.5 mm coupled with quick evaporation in some water saturated samples, suggests a connected porosity range of 0 to 10 percent. Healed and partially healed fractures present in hand specimens have sparry calcite fillings.

In summary, three fracture sets exist in the Santa Elena limestone at the Lajitas, Texas site: vertical NNW and ENE trending orthogonal sets, and horizontal parting along bedding planes. This fracturing occurred both on a microscopic and macroscopic scale. Based on field observations, the Santa Elena limestone is composed primarily of calcite and varies in porosity from sample to sample.

## IV. Laboratory Measurements

Determining microscopic fracture orientation and seismic velocity in hand specimens in the laboratory aids in measuring microscopic inhomogeneities (such as vuggy porosity, high clay content, fractures, etc.) that may significantly affect propagating waves through material *in situ*. Testing the Santa Elena's degree of homogeneity in the laboratory entails methods similar to those used by Sorrells (1961). The methodology and laboratory results for measurements of P- and S-wave velocity, dry and saturated bulk rock density, grain density, porosity, microscopic fracture and pore geometry, and mineralogical composition follow in the next section. Note that the total porosity $\phi$ of a bulk medium equals the sum of its total crack porosity $\phi_c$ and total pore porosity $\phi_p$; where $\phi_c$ is the total void space between open fractures and $\phi_p$ is the total spheroidal to ellipsoidal void space within a given unit volume.

### Methodology

<u>Porosity/Density Measurement</u>. Spatial changes in porosity and composition can cause variations in bulk rock velocities of as much as 20 percent. Heterogeneities such as these can effect velocities measured *in situ*. Without knowledge of bulk rock porosity and compositional variations, one may

falsely conclude that azimuthal anisotropy exists. Laboratory porosity and dry bulk rock and grain density measurements aid in determining variation in composition and porosity between samples.

Determination of the mineral grain density, saturated and dry bulk rock densities and porosity requires the measurement of sample weight parameters. These parameters include dry weight, $w_D$, suspended weight, $w_{SU}$, and saturated weight, $w_{SA}$. The procedure for these measurements utilizes the techniques developed by Archimedes in 210 B.C. (Tipler, 1982). To obtain dry weight, one must first extract all moisture from plug samples using a vacuum oven set at approximately 60°C. Leaving samples in the vacuum oven for 24 hours and then allowing the samples to cool 20 minutes before weighing on the Mettler PE 3600 yields dry weight measurements with errors less than 0.01 grams. Prior to measuring saturated and suspended weights, one must saturate the samples using a pressure vessel (Figure 4.1).

Obtaining saturated and suspended weights entails weighing samples both resting on the bottom of and suspended in a beaker containing "saturation fluid"; in this case, water. The beaker rested on a Mettler PE 3600 balance capable of resolving weights to ±0.01 grams. To determine the saturated weight, $w_{SA}$:

(4.1) $$w_{SA} = w_{S+F+B} - w_{F+B}$$

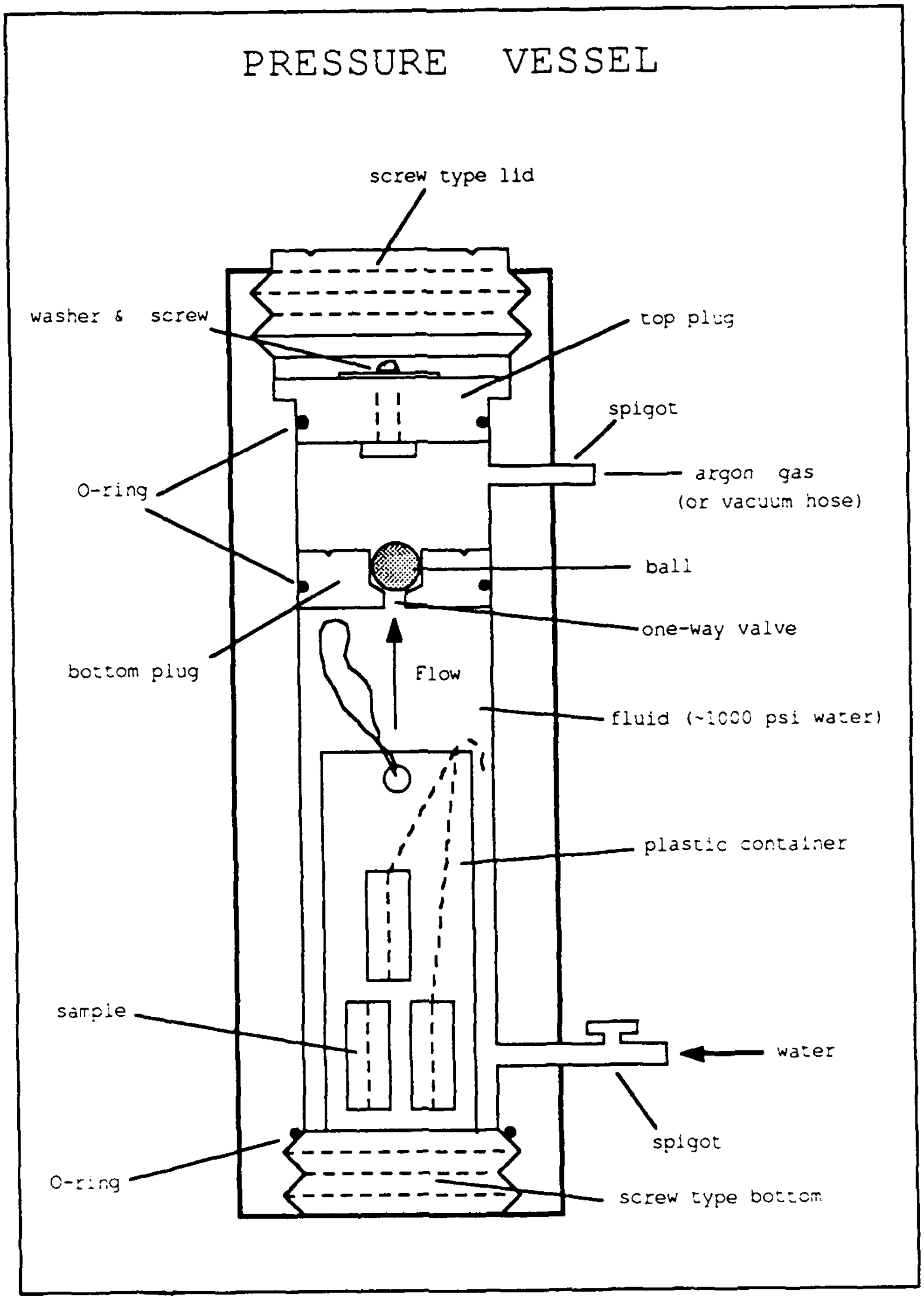


Figure 4.1 Pressure vessel used to saturate plug samples with water.

where $w_{S+F+B}$ equals the weight of the fluid, beaker, and a saturated sample resting fully immersed on the bottom of the beaker; and $w_{F+B}$ equals the weight of the beaker and fluid. To determine the suspended weight, $w_{SU}$:

$$w_{SU} = w_{SuS+F+B} - w_{F+B} \tag{4.2}$$

where $w_{SuS+F+B}$ equals the weight of the fluid, beaker, and a fully immersed saturated sample suspended from a string. Measuring $w_{F+B}$ before lowering each sample into the fluid-filled beaker is important. Due to surface tension, the volume of fluid in the beaker decreases with each sample removal, thus $w_{F+B}$ changes with each progressive set of saturated and suspended weight measurements. Also, using a fine string such as fishing line to slowly lower samples into the beaker eliminates fluid loss due to splashing.

Measurements of the dry weight $w_D$, $w_{SU}$, and $w_{SA}$ are sufficient to calculate connected porosity and density for each sample. Taking the ratio of pore volume to total volume, $V_P/V_T$, yields fractional porosity, $\phi$, where:

$$V_P = (w_{SA} - w_D)/\rho_f \tag{4.3}$$

and

$$V_T = w_{SU}/\rho_f . \tag{4.4}$$

Thus, with saturation fluid density, $\rho_f$, equivalent to 1.00

gm/cc for water:

(4.5) $$\phi = V_P/V_T = (w_{SA} - w_D)/w_{SU}.$$

For dry and saturated rock densities, $\rho_{dry}$ and $\rho_{sat}$:

(4.6) $$\rho_{dry} = w_D/V_T = (w_D/w_{SU})/\rho_f,$$

and

(4.7) $$\rho_{sat} = w_{SA}/V_T = (w_{SA}/w_{SU})/\rho_f.$$

The grain density, $\rho_{grain}$, equals:

(4.8) $$\rho_{grain} = w_D/V_S = w_D/[\rho_f(w_{SU}+w_D-w_{SA})]$$

where $V_S$ represents the solid volume of a sample, the difference between the total plug volume and pore volume:

(4.9) $$V_T - V_P = (w_{SU}+w_D-w_{SA})/\rho_f.$$

This method gives accurate estimates (±0.005) of dry bulk and saturated rock densities, grain density, and porosity provided unconnected void space does not exist in concentrations greater than 0.5 percent. For instance, a dry sample of pure calcite equal to a bulk volume of 19.306 cc with void space equal in concentration to 0.06 for air-filled connected porosity and 0.03 for isolated water-filled porosity weighs 48.3654 g and equals 2.5052 g/cc in density:

(4.10)
$$\rho_{dry} = (1-\phi)\,\rho_S + (\phi_W)\,\rho_W ,$$
$$= (1 - 0.09)\left(2.72\ ^{g}/_{cc}\right) + (0.03)\left(1.00\ ^{g}/_{cc}\right) ,$$
$$= 2.5052\ ^{g}/_{cc}$$

and

(4.11)
$$w_D = (\rho_D)\, V_T ,$$
$$= \left(2.5052\ ^{g}/_{cc}\right) 19.306\ cc = 48.3654\ g ,$$

where the total porosity and isolated porosity is $\phi$ and $\phi_w$ respectively and the density of water is $\rho_w$. The saturated weight equals

(4.12)
$$w_{SA} = \left((1-\phi)\ \rho_S + (\phi_P\, \rho_W)\right) ,$$
$$= 49.5238\ g .$$

Applying the rules of Archimedes:

(4.13)
$$w_{SU} = V_T\ \rho_w = 19.306\ cc ,$$

(4.14)
$$\rho_{grain} = \frac{48.3654\ g}{1.00\ g/cc\ (19.306\ g + 49.3654\ g - 49.5238\ g)} ,$$
$$= 2.5259\ g/cc$$

and

(4.15)
$$\phi = \frac{49.5238\ g - 48.3654\ g}{19.306\ g} = 0.06 .$$

Thus, the methods of Archimedes do not account for isolated pore porosity and consequently underestimate grain density when isolated porosity exists.

Table 4.1 lists density and porosity measurements for eacn of three plugs extracted from six of the eight oriented Santa Elena hand specimens. (Plugs of sufficient length could not be obtained from densely fractured samples VLS-4 and VLS-8.) Bulk dry rock densities range from 2.337 gm/cc to 2.611 gm/cc, whereas grain densities range from 2.667 gm/cc to 2.721 gm/cc. Calculations omitting the two grain density extremes yield a mean grain density of 2.70 gm/cc plus or minus a 0.03 maximum deviation. Thus, with grain densities measuring no less than 98 percent of pure calcite's 2.72 gm/cc density, differences observed between dry bulk and grain density in Table 4.1 are most likely due to connected pore space or air-filled microfractures and small concentrations (less than 3 percent) of isolated pore space. Grain densities less than 2.70 gm/cc imply the presence of secondary minerals and/or unaccounted isolated pore space. Percent porosity correlates well with changes between dry bulk and grain densities from plug to plug.

<u>Determination of Mineralogical Composition</u>. Pure limestones with isolated pore space yield grain densities less than that of pure calcite ($\rho_{calcite}$ = 2.72 g/cc). Grain densities less than 2.72 g/cc (by approximately 2 percent or more) also result when limestones contain secondary minerals

TABLE 4.1

POROSITY/DENSITY LABORATORY MEASUREMENTS

| Sample No. | Plug | Dry Rock Density (gm/cc) | Saturated Rock Density (gm/cc) | Grain Density (gm/cc) | Porosity (%) |
|---|---|---|---|---|---|
| | X1 | 2.505 | 2.580 | 2.709 | 7.5 |
| VLS-1 | Y1b | 2.569 | 2.617 | 2.699 | 4.8 |
| | Z1b | 2.550 | 2.602 | 2.689 | 5.2 |
| | X2 | 2.563 | 2.609 | 2.686 | 4.6 |
| VLS-2 | Y2b | 2.593 | 2.621 | 2.667 | 2.8 |
| | Z2 | 2.558 | 2.603 | 2.678 | 4.5 |
| | X3 | 2.472 | 2.563 | 2.720 | 9.1 |
| VLS-3 | Y3 | 2.567 | 2.619 | 2.707 | 5.2 |
| | Z3 | 2.455 | 2.544 | 2.697 | 9.0 |
| | X5 | 2.523 | 2.596 | 2.721 | 7.3 |
| VLS-5 | Y5 | 2.575 | 2.622 | 2.701 | 4.7 |
| | Z5 | 2.500 | 2.573 | 2.698 | 7.3 |
| | X6 | 2.611 | 2.640 | 2.688 | 2.8 |
| VLS-6 | Y6 | 2.604 | 2.629 | 2.672 | 2.5 |
| | Z6 | 2.584 | 2.619 | 2.676 | 3.4 |
| | X7 | 2.564 | 2.617 | 2.708 | 5.3 |
| VLS-7 | Y7 | 2.337 | 2.477 | 2.719 | 14.0 |
| | Z7 | 2.481 | 2.568 | 2.718 | 8.7 |

in concentrations approximately greater than 10 percent. Knowledge of mineralogical composition therefore facilitates estimates of total porosity in hand specimens.

X-ray diffraction analysis effectively identifies minerals and their corresponding relative abundances present in rock specimens. This type of analysis examines diffraction effects of x-rays incident on crystal lattice structures.

Determining mineralogical composition using x-ray diffraction techniques requires four basic steps: 1) sample preparation and estimation of coarse to fine particle weight percents, 2) measurement of diffracted angles, 3) application of Bragg's law, and 4) identification of minerals and estimation of their relative abundances.

To avoid grinding distinct grains during sample preparation, 1 - 2 mm disks sliced from each plug sample were crushed using a mortar and pestle. Determining the relative weight percents of sand and silt and clay size particles necessitated the measure of the total crushed sample weight, $w_{TOT}$, and the weight of sand and silt, $w_{SS}$, for each sample. Measurement of $w_{SS}$ required the separation of sand and silt sized particles from clay size particles less than 4 microns. After soaking each crushed sample in de-ionized water and sodium pyrophosphate to minimize flocculation problems, a sonic probe aided in removing clay size particles (or grain coatings) from host grains. Centrifuging and decanting the liquid separated sand and silt grains from clay particles in suspension. Drying and weighing residues left in the bottoms of the centrifuge tubes yielded weight percents of coarse and fine particles:

(4.16) $100(w_{SS}/w_{TOT})$ = % sand and silt size particles

(4.17) $100 - [100(w_{SS}/w_{TOT})]$ = % clay size particles

A micronizing machine ground the sand and silt residues to white flour; randomly orienting grains and consequently producing good diffraction characteristics. Measuring the change in *d* spacing from a dry to saturated state helped in identifying the clay type. To measure *d* spacings along the *c* axis in clays, clay particles left in suspension were funnelled through filters. (Due to their platy nature, the particles tended to settle on flat faces.) The *d* spacing in clays equals the distance between indefinite extended sheets of $SiO_4$ tetrahedra; where three of the four oxygens in each $SiO_4$ tetrahedron are shared with neighboring tetrahedra, leading to a ratio of Si:O = 2:5. Each sheet, if undistorted, has a hexagonal symmetry with the *c* axis perpendicular to the sheets of tetrahedra (Hurlburt and Klein, 1977). Because some clays swell or expand when saturated with fluid, *d* spacings can become enlarged. The degree of *d* spacing enlargement depends on the type of clay. Hence, diffraction patterns were obtained for oriented clay specimens both in an air and liquid saturated state.

Ethylene glycol, a fluid that expands and stabilizes *d* spacing, was used to saturate clays (Klug and Alexander, 1974).

X-ray diffraction analysis revealed the presence of secondary minerals in abundance of 2.5 to 8.8 percent (Table 4.2). These secondary minerals include quartz, ranging in quantity from 0.8 to 6.1 percent, and clays, ranging from 1.3 to 2.7 percent. Relative percentages for quartz, calcite, and total clay minerals have a 2 percent error factor; whereas the percentage error present in relative clay abundances, such as smectite, illite, and kaolinite, approaches 20 percent. Calcite, ranging from 91.2 to 97.5 percent (in relative abundance from plug to plug), is obviously the primary constituent. Therefore, results from the X-ray diffraction analysis support the inferences made from the porosity/density measurements. Differences observed between dry bulk and grain density result primarily from open pore space or microfractures, rather than substantial secondary mineral concentrations.

<u>Velocity Measurement</u>. Detecting and quantifying velocity anisotropy requires knowledge of either P- or S-wave velocity. For P-waves, defining anisotropy resulting from wave propagation through a fractured solid requires measurement of compressional velocity along two or more physically different propagation paths. Factors other than anisotropy, such as variation in rock composition, pore fluid saturation,

TABLE 4.2

XRD ANALYSIS--SOUTH TEXAS LIMESTONES

| SAMPLE ID. | VLS-1 | VLS-2 | VLS-3 | VLS-5XY | VLS-5Z | VLS-6 | VLS-7XY | VLS-7Z |
|---|---|---|---|---|---|---|---|---|
| Whole Rock Mineralogy | | | | | | | | |
| Quartz | 2.9% | 4.4% | 6.1% | 1.8% | 2.5% | 4.1% | 0.7% | 0.8% |
| Calcite | 94.6% | 93.6% | 91.2% | 96.9% | 95.7% | 94.5% | 96.6% | 97.5% |
| Total Clay Minerals | 2.5% | 2.0% | 2.7% | 1.3% | 1.8% | 1.4% | 2.6% | 1.7% |
| Total | 100.0% | 100.0% | 100.0% | 100.0% | 100.0% | 100.0% | 100.0% | 100.0% |
| Relative Clay Abundances | | | | | | | | |
| Smectite | 6.9% | 0.0% | 0.0% | 0.0% | 0.0% | 0.0% | 4.7% | 6.5% |
| Illite | 64.5% | 32.8% | 0.0% | 39.2% | 0.0% | 0.0% | 0.0% | 0.0% |
| Kaolinite | 28.7% | 67.2% | 100.0% | 60.8% | 100.0% | 100.0% | 95.3% | 93.5% |
| Total | 100.0% | 100.0% | 100.0% | 100.0% | 100.0% | 100.0% | 100.0% | 100.0% |

etc., also influence P-wave velocity more than S-wave velocity. Shear waves give more information about aligned cracks than do P-waves. Shear waves in anisotropic media split into two orthogonal polarized components which travel along identical propagation paths. These two components propagate at different velocities and separate in time. In a fractured solid, the shear wave component polarized parallel to the fracture plane strikes arrive first at the receiving end (Crampin, 1985). Thus measuring both P- and S-wave velocity, with shear-wave displacements polarized both parallel and perpendicular to observed fracture trends in hand specimens and outcrop, aids in defining pore geometry (spheroids versus fractures). Also, $V_P/V_S$ gives information concerning mineralogical composition, in addition to that obtained from porosity/density measurements and XRD analysis (Wilkens et al., 1984).

Velocity was measured for 3 - 5 cm cylindrical plugs 2.54 cm in diameter; as plugs longer than 5 cm vibrate and generate tube waves that produce spurious results. Error in travel time measurements increases from ±0.03 km/s to ±0.06 km/s when plugs are less than 2.54 cm in length.

Ends were trimmed and ground flat parallel to one another within 0.0015 cm for three plugs extracted from each of the six oriented Santa Elena rock samples. The orientation of each plug axis parallels poles to fractures or bedding. The axes of plugs Y and Z parallel northwest and northeast fracture plane normals respectively, whereas the X axis plug is vertical (Figure 4.2). Orientation of each plug axis comes within 10 degrees of fracture and bedding plane normals.

In the laboratory the velocity V is determined from the sample length L and the transit time $\Delta T$:

$$V = L/\Delta T \tag{4.18}$$

An ultrasonic pulse technique developed by Simmons (1965) measures travel times with errors less than 0.05 microseconds.

The travel time of an elastic wave through a set of transmitting and receiving transducers equals the time delay between a pulse input and signal output (minus any corrections). Because waves must pass through a coupling resin and a transducer facing material, designed to reduce ringing, static time corrections must be subtracted from raw measured transit times. Correction times equal 0.65 and 1.00 μs for P- and S-waves respectively.

With all measurements made under ambient conditions (i.e., bench-top) with no saturating liquids or confining pressure, the application of a uniaxial load of approximately 5 - 10 bars, with the use of parallel clamps, improved coupling between plug end and transducer surfaces, and thus yielded good P- and S-wave data.

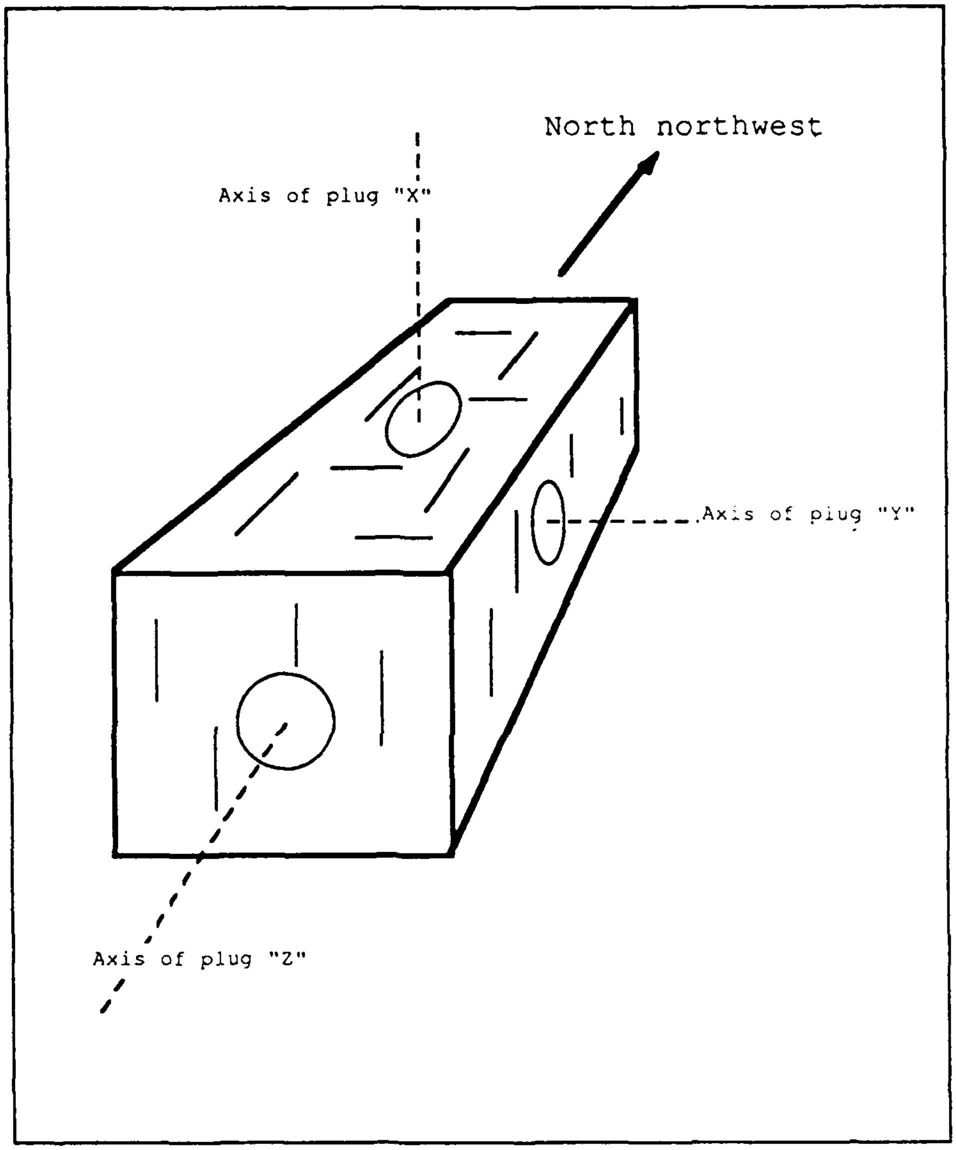


Figure 4.2 Illustration showing plug axes orientations.

Two switches in the transducer electrical circuit allowed for the change from longitudinal displacement to either of two shear wave polarizations. The propagation paths and particle displacement orientations of these three waves differ slightly, as shown in Figures 4.3 and 4.4. Transmitting one wave at a time substantially reduced P- to S- and S- to P-wave conversions due to reflections off the plug wall.

The frequency band width ranged from 1.5 - 2.75 MHz with wavelengths averaging approximately 1 - 2 millimeters. Each transducer disk used in this study had a free resonant frequency of 1 MHz.

The velocity data support the inferences made from the porosity/density measurements and XRD analysis (Table 4.3). Shear wave velocities vary azimuthally less than 2.00 percent (and in most cases less than 0.35 percent) within each individual plug. This 2.00 percent variation is well within the bounds of experimental error, hence azimuthal anisotropy either does not exist or can not be resolved (solely comparing fractional porosity to wave velocity) in the laboratory samples. However, shear velocities vary substantially from plug to plug--in the most extreme case as much as 12 percent. Variation of compressional wave velocities from plug to plug ranges from 0.7 - 15.8 percent. The higher values of measured connected porosity correlate with the lower P- and S-wave velocity measurements. Appendix B

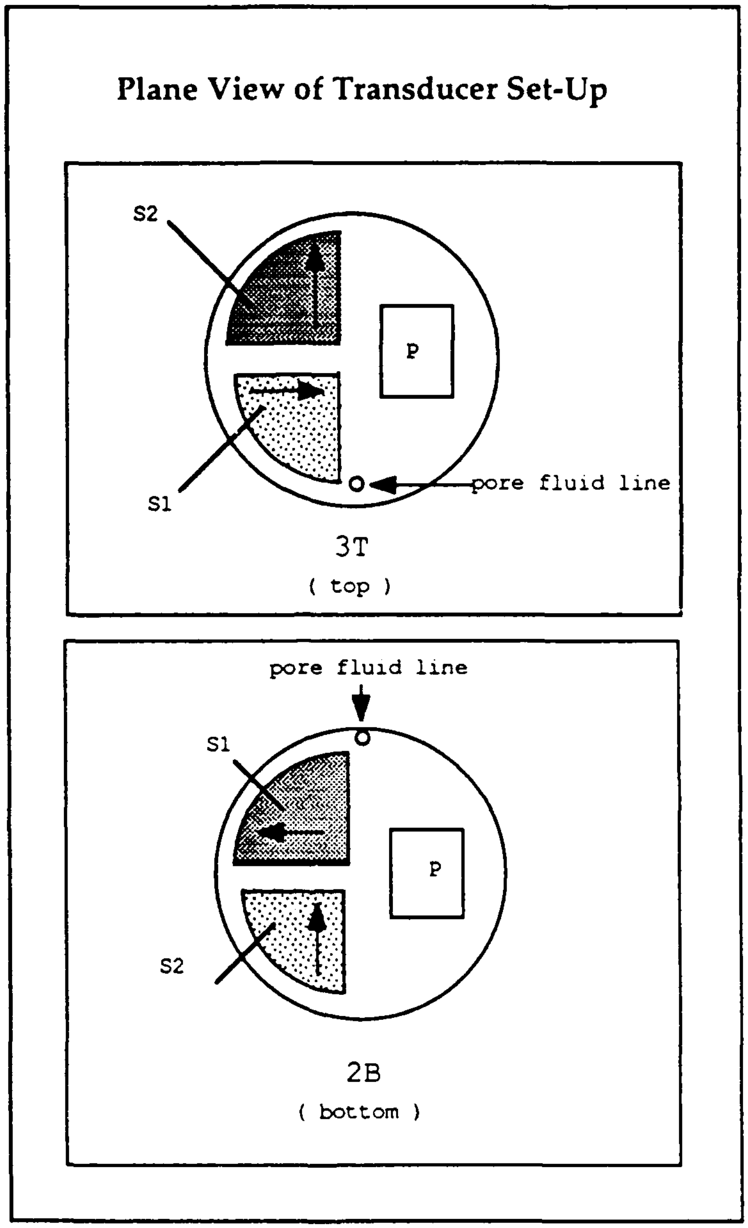


Figure 4.3 Configuration of upper and lower transducer sets.

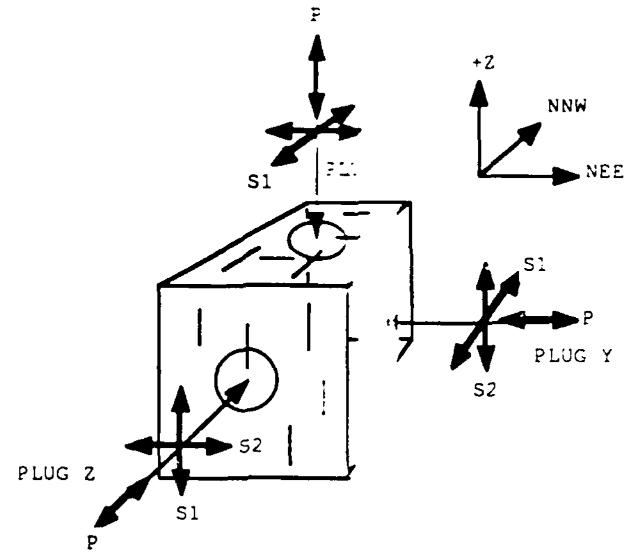


| Plug | P, S1, or S2 | Shear Component | Particle Displacement Directions |
|---|---|---|---|
| X | P | N/A | +Z/-Z |
| | S1 | SH | NNW/SSE |
| | S2 | SH | NEE/SWW |
| Y | P | N/A | NEE/SWW |
| | S1 | SH | NNW/SSE |
| | S2 | SV | +Z/-Z |
| Z | P | N/A | NNW/SSE |
| | S1 | SV | +Z/-Z |
| | S2 | SH | NEE/SWW |

Figure 4.4. Particle displacement orientation of compressional and shear waves generated by transducers.

TABLE 4.3

LABORATORY VELOCITY AND POROSITY MEASUREMENTS

| Sample No. | $V_P$ (km/s) | $V_{S1}$ (km/s) | $V_{S2}$ (km/s) | Porosity (%) |
|---|---|---|---|---|
| X1 | 5.25 | 2.94 | 2.95 | 7.5 |
| Y1b | 5.71 | 3.11 | 3.10 | 4.8 |
| Z1b | 5.70 | 3.11 | 3.10 | 5.2 |
| X2 | 5.56 | 3.04 | 3.04 | 4.6 |
| Y2b | 5.75 | 3.13 | 3.10 | 2.8 |
| Z2 | 5.64 | 3.10 | 3.09 | 4.5 |
| X3 | 5.23 | 2.90 | 2.90 | 9.1 |
| Y3 | 5.84 | 3.12 | 3.11 | 5.2 |
| Z3 | 5.58 | 3.11 | 3.10 | 9.0 |
| X5 | 5.71 | 3.08 | 3.08 | 7.3 |
| Y5 | 5.66 | 3.09 | 3.10 | 4.7 |
| Z5 | 5.66 | 3.11 | 3.06 | 7.3 |
| X6 | 5.87 | 3.15 | 3.18 | 2.8 |
| Y6 | 5.83 | 3.16 | 3.17 | 2.5 |
| Z6 | 5.80 | 3.17 | 3.19 | 3.4 |
| X7 | 5.85 | 3.10 | 3.16 | 5.3 |
| Y7 | 4.94 | 2.80 | 2.81 | 14.0 |
| Z7 | 5.66 | 3.17 | 3.11 | 8.7 |

gives a representative sampling of the waveforms from which travel times were selected.

Figures 4.5 and 4.6 illustrate the changes in P- and S-wave velocity with varying porosity. Scatter exceeds the limits of experimental error for porosities greater than 5 percent. Distribution and variation of pore geometries and changes in clay and silica content less than a few percent may contribute to this scatter.

The P- and S-wave matrix velocities, obtained from the zero intercepts, equal 6.04 km/s and 3.23 km/s respectively. These matrix velocities fall below Dandekar's (1968) matrix $V_P$ and $V_S$ measurements of 6.53 km/s and 3.36 km/s for pure calcite. Figure 4.7 shows the $V_P/V_S$ versus porosity for each plug of Santa Elena limestone. Again the zero intercept, of the linear curve best fit to the velocity data, falls slightly below Dandekar's (1968) $V_P/V_S$ measure of 1.94. In contrast to calcite, the matrix velocities and $V_P/V_S$ for pure quartz equal 6.05 km/s ($V_P$), 4.09 km/s ($V_S$), and 1.48 ($V_P/V_S$) (McSkimin et al., 1965).

The influence of composition, porosity, and pore geometry must now be quantified in order to interpret the laboratory seismic data. For a set of siliceous limestones, Wilkens et al. (1984) measured $V_P$ and $V_S$; determined bulk density, effective porosity, and carbonate content; and observed pore and fracture distributions using a scanning electron microscope. They showed that composition is more

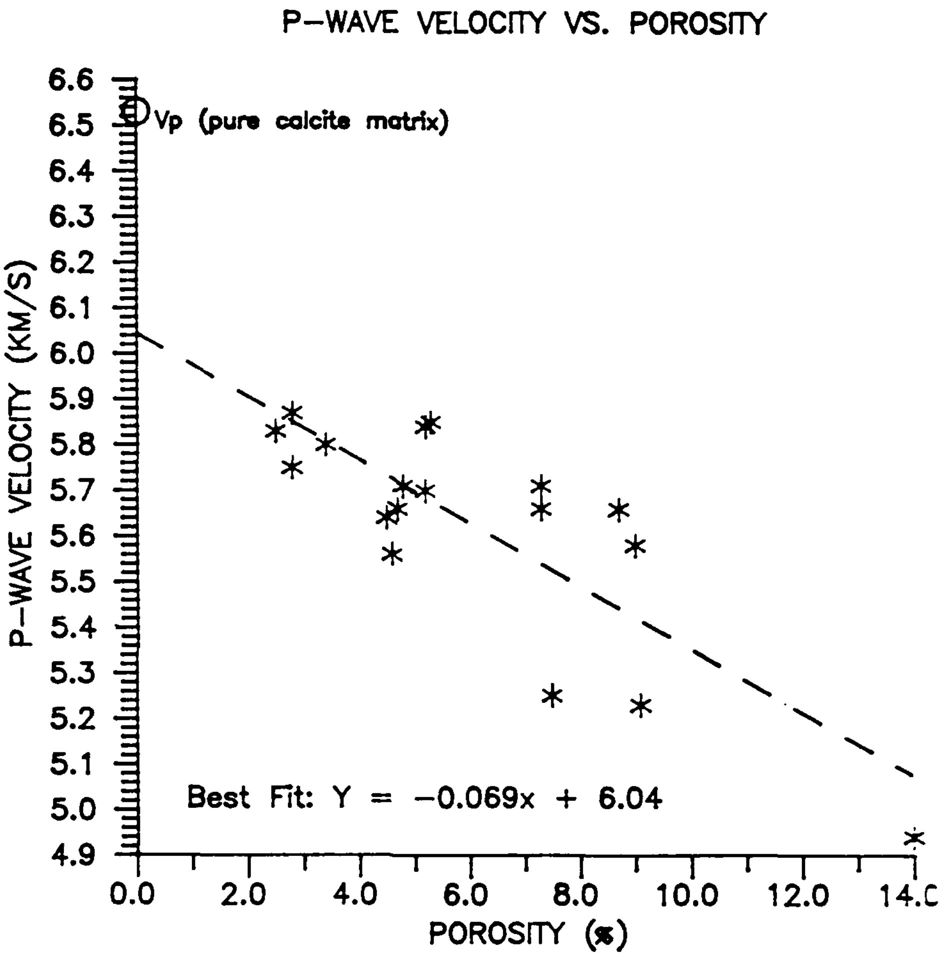


Figure 4.5 Changes in laboratory measurements of P-wave velocity versus porosity for the Santa Elena limestone.

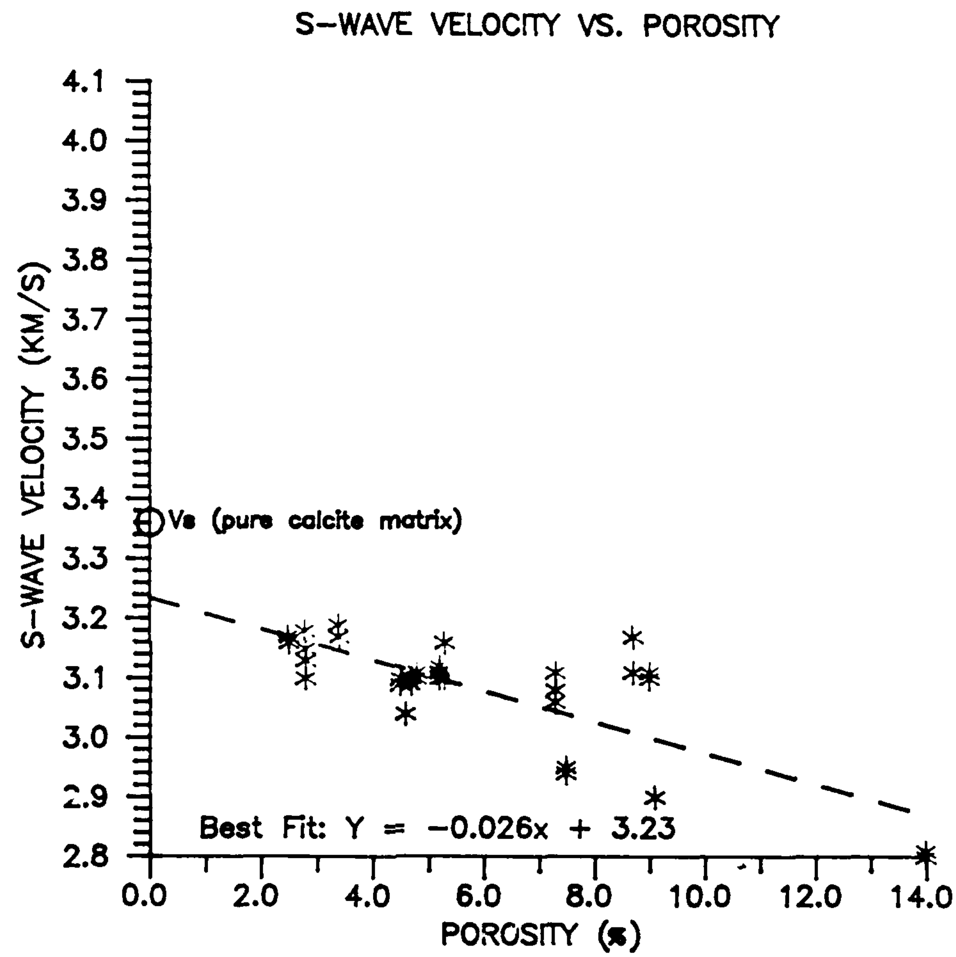


Figure 4.6 Changes in laboratory measurements of S-wave velocity versus porosity for the Santa Elena limestone.

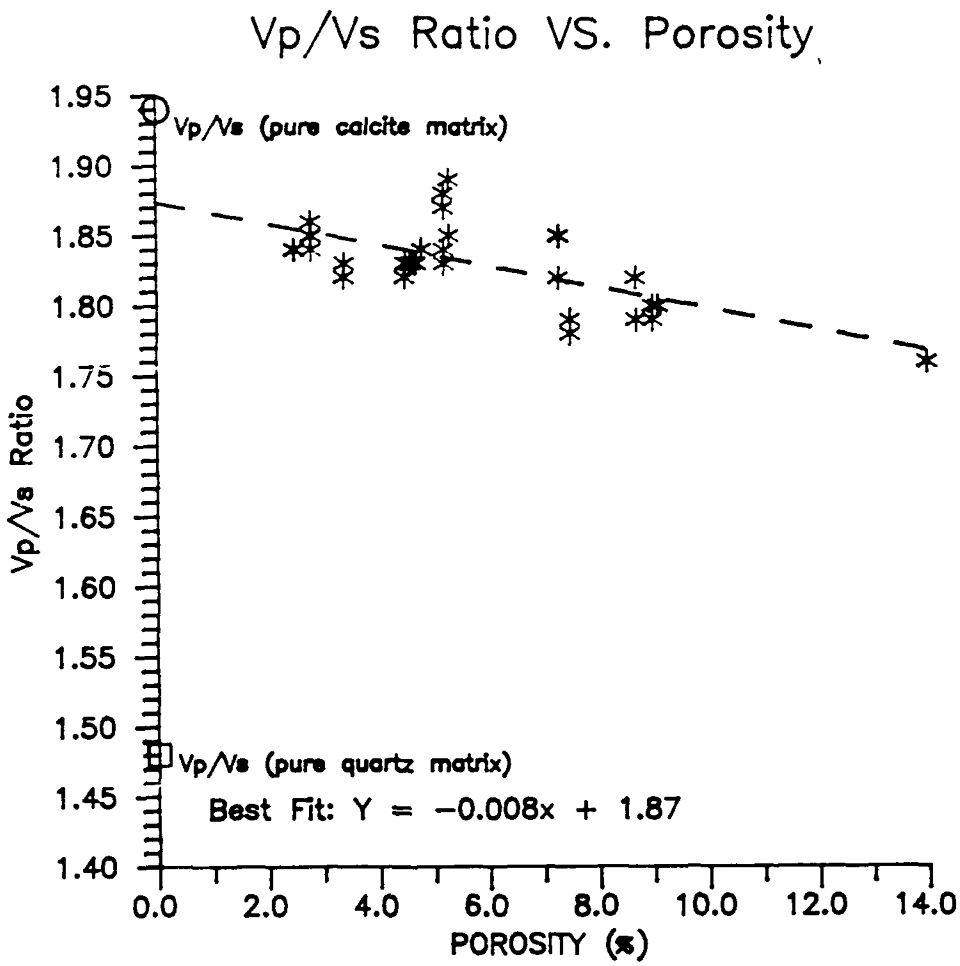


Figure 4.7 Vp/Vs ratio versus porosity for each plug of Santa Elena limestone.

important than porosity and pore geometry for $V_P/V_S$. According to Wilkens et al. (1984), the effect of composition is best ascertained from data obtained at high pressures where microfractures are closed.

At 1 kbar, both $V_P$ and $V_S$ increase with increasing bulk density and decreasing porosity in compositionally homogeneous sample sets. But, for siliceous limestones, $V_P$ increases monotonically and $V_S$ remains invariant because quartz, although less dense than calcite, has a higher shear wave velocity. ($V_P/V_S$ for quartz equals 1.5; whereas for common phase minerals in sedimentary rocks such as calcite, dolomite, and feldspar, $V_P/V_S$ equals or falls between 1.8 and 2.0.) Increasing pressure (closing microfractures) has little effect on $V_P/V_S$ between 0.01 and 1.0 kbar. Changing porosity by ± 5 percent in silica-rich limestones decreases $V_P/V_S$ by approximately 5 percent, but as quartz content decreases and calcite increases, $V_P/V_S$ increases by 20 percent. That is, total porosity and pore geometry cause variations of approximately 0.1 in $V_P/V_S$, whereas compositional variation equals 0.4. Because the Santa Elena's $V_P/V_S$ of 1.87 comes so close to the calcite ratio, the XRD measurements of 1.3 to 2.6 percent in clay content suggest that clay probably plays a role in lowering the Santa Elena's P- and S-wave matrix velocities, as concentrations of only 3 percent can lower longitudinal wave velocities (Sorrells, 1961).

For pure limestones, pore aspect ratios determined with the theory of Toksöz et al. (1976) (for seismic velocities) agree with the Wilkens et al. (1984) electron microscope observations. Based on this earlier success, laboratory measurements of the Santa Elena's P- and S-wave velocity normalized to the P- and S-wave matrix velocities of 6.05 km/s and 3.23 km/s respectively, are plotted, on the theoretical curves of Toksöz et al. (1976) for equations (4.22) and (4.23), as a function of aspect ratio and gas-saturated porosity in Figures 4.8 and 4.9. Aspect ratio, defined as the ratio of the minor to major semiaxis of a spheroid, estimates pore geometry. Data points for P-waves range in aspect ratio from approximately 0.1 to 1.0. With the exclusion of 6 out of 32 data points greater than 1.0, S-wave data points also range from approximately 0.1 to 1.0. For all S-wave data points to plot at or below 1.0, the normalizing velocity must equal 3.30 km/s; hence the S-wave intercept velocity chosen from Figure 4.6 may be low by 0.07 km/s. Experimental error may be another contributing factor to the high aspect ratios. Figures 4.8 and 4.9 indicate that pore spaces, ellipsoidal to spherical in shape, primarily contribute to the scatter observed in Figures 4.6 and 4.7.

In order to utilize results such as those in Figure 4.8 and 4.9, it is necessary to investigate the foundation of the Toksöz et al. (1976) model. Toksöz et al. (1976) demonstrate the effects of inclusion shapes on the velocities of a

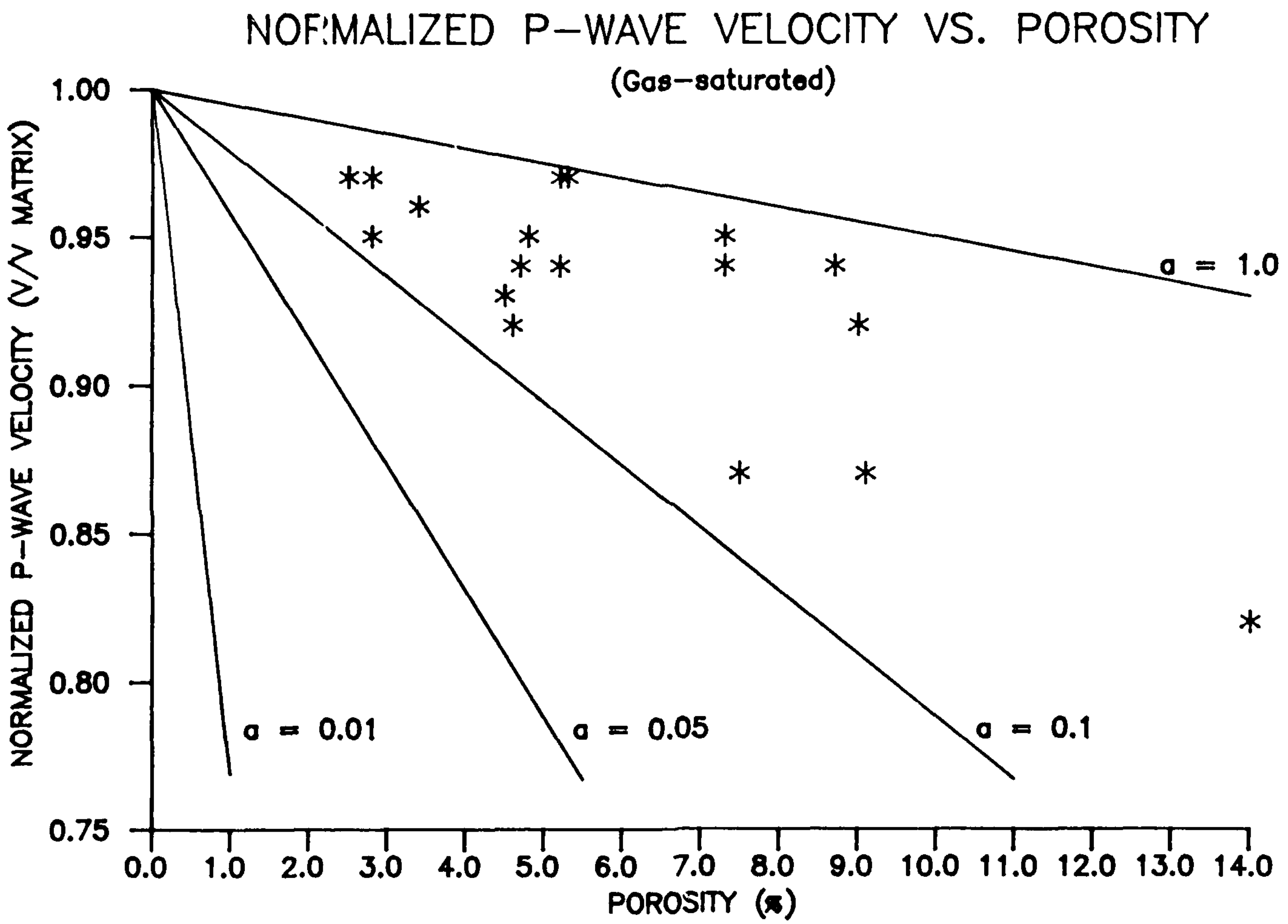


Figure 4.8 Theoretical compressional wave velocity—porosity relationships for differing aspect ratios versus data from this study. The ratio of the minor to major semiaxis of a speroid defines the aspect ratio a.

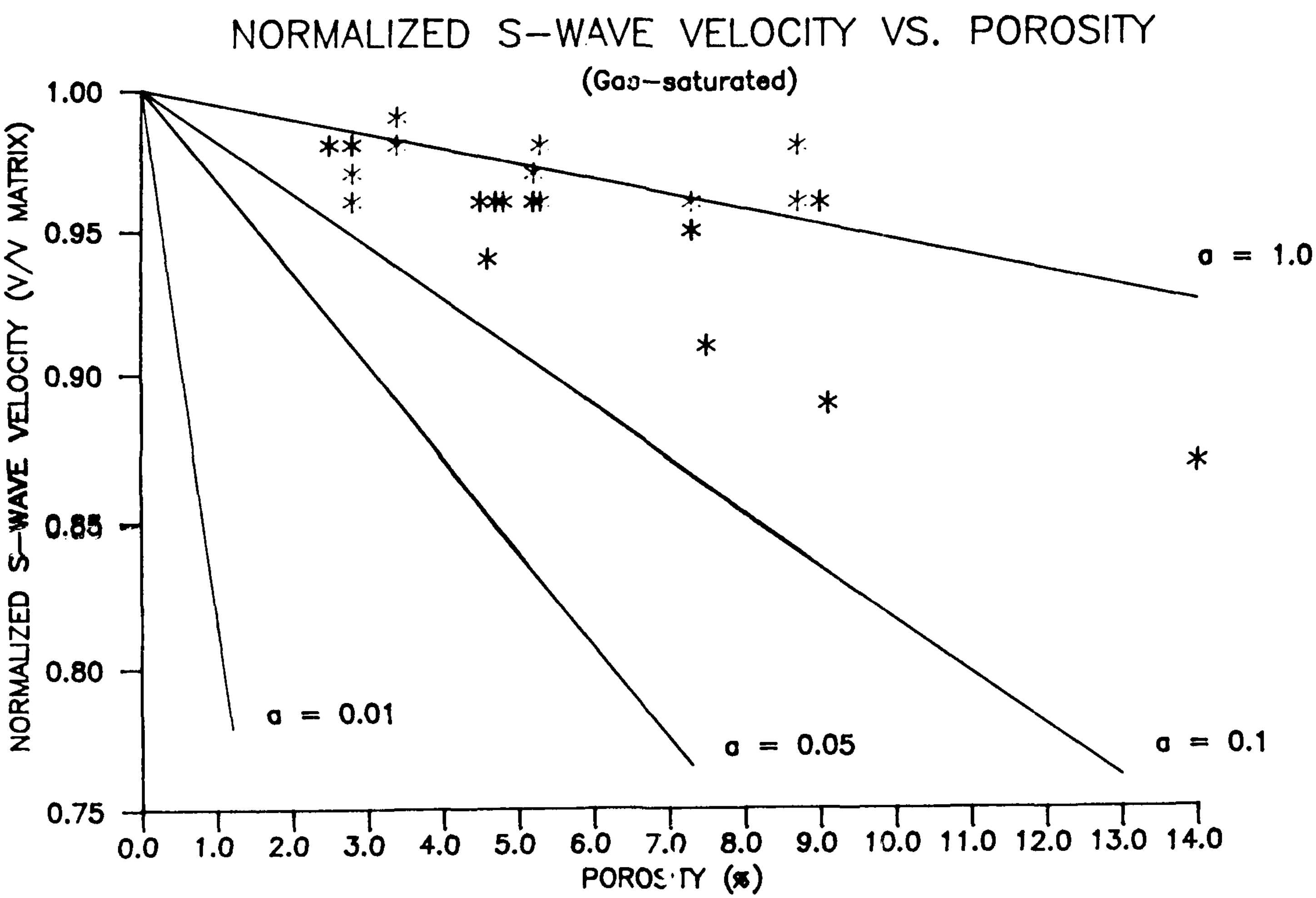


Figure 4.9 Theoretical shear wave velocity–porosity relationships for differing aspect ratios versus data from this study. The ratio of the minor to major semiaxis of a spheroid defines the aspect ratio a.

composite medium by comparing velocities and reflection coefficients predicted by an idealized model with published laboratory results. Their model defines a porous rock in terms of a solid elastic matrix, randomly distributed pores, and saturating fluids (gas, oil, or water). Assuming wavelengths long in comparison to pore size, and utilizing the formulas of Kuster and Toksöz (1974) based on scattering theory enables the approximation of a whole rock in terms of an equivalent homogeneous medium with some effective elastic coefficients. Toksöz et al. (1976) use these equations for calculating velocities and extend the theory to cover mixed-fluid (i.e., gas-water, oil-water) saturation for a spectrum of shapes. They also derive expressions relating pressure to seismic velocities in a porous and saturated medium.

Specifying the medium properties in terms of the bulk modulus K, shear modulus $\mu$, and density $\rho$

(4.19) $$\frac{\tilde{K}-K}{3\tilde{K}+4\mu} = \frac{1}{3} . c . \frac{K'-K}{3K+4\mu} T_{iijj} ,$$

(4.20) $$\frac{\tilde{\mu}-\mu}{6\tilde{\mu}(K+2\mu)+\mu(9K+8\mu)} = c\,\frac{\mu'-\mu}{25\mu(3K+4\mu)}\left[T_{ijij}-\frac{1}{3}T_{iijj}\right],$$

and

(4.21) $$\tilde{\rho} = \rho(1-c) + c\rho' ,$$

where c is the volume concentration of the inclusions, $T_{iijj}$ and $T_{ijij}$ are scalar quantities, functions of K, μ, K', μ', and the aspect ratio, α, of the inclusions. The ratio of the minor to major semiaxis of a spheroid defines the aspect ratio. A fracture's aspect ratio is a measure of its flatness. Unprimed quantities (K, μ, ρ) and primed quantities (K', μ', ρ') refer to the matrix and inclusions respectively whereas "tilded" quantities equal effective properties of the composite medium. (See Appendix C for expressions of $T_{iijj}$ and $T_{ijij}$.)

Using a rock model derived on the basis of laboratory data in the equations for calculating velocities, Toksöz et al. (1976) reach several conclusions. The conclusions most important to this study are 1) for a given matrix the composite elastic moduli and seismic velocities of rocks decrease with increasing porosity, 2) compressional velocities are affected more by properties of saturating fluids than shear velocities, and 3) for a given pore concentration, flatter (thinner) pores affect velocities substantially more than rounder or spherical pores. In fact, the presence of pores with aspect ratios less than 0.01 in concentrations of less than a percent can decrease velocities by as much as 20 percent.

Typically a whole rock contains pore shapes ranging from nearly equidimensional to very flat thin spaces. Theoretically, this variation can be represented in terms of a spectrum of aspect ratios; where spheres and rounded spheroids approximate equidimensional and vugular pores, and ellipsoids of low aspect ratio represent fractures or flat pores. Two or more crack populations comprise a spectrum of aspect ratios; that is, cracks in population "A" have aspect ratios equal to "a" and those in population "B" have aspect ratios equal to "b". As air saturated pores of small aspect ratio cause a greater change in compressional wave velocities than shear velocities, determining the effects of total porosity on seismic velocities in a whole rock requires one to examine the effects of each population individually. Generalizing the theoretical formulas given by equations (4.19) to (4.21) for the case of mixed aspect ratios, the effective bulk and shear modulus equal

$$\frac{\tilde{K}-K}{3\tilde{K}+4\mu} = \frac{1}{3}\cdot\frac{K'-K}{3K+4\mu}\sum_{m=1}^{M} c(\alpha_m)\cdot T_{iijj}(\alpha_m), \tag{4.22}$$

and

$$\frac{\tilde{\mu}-\mu}{6\tilde{\mu}(K+2\mu)+\mu(9K+8\mu)} = \frac{\mu'-\mu}{25\mu(3K+4\mu)}\sum_{m=1}^{M} c(\alpha_m)\cdot\left[T_{ijij}(\alpha_m)-\frac{1}{3}T_{iijj}(\alpha_m)\right], \tag{4.23}$$

where $c(\alpha_m)$ equals the concentration of pores with aspect ratio $\alpha_m$ and the total porosity in this case is

$$\phi = \sum_{m=1}^{M} c(\alpha_m). \qquad (4.24)$$

Assuming "noninteraction" between spheroidal pores and fractures (as this theory does) imposes the restriction $[c(\alpha_m)]/\alpha_m < 1$ in the application of equations (4.22) to (4.24) (Toksöz et al., 1976).

As the seismic data in Figure 4.8 and 4.9 indicate, the application of the Toksöz model predicts aspect ratios between 0.1 to 1.0. This geometry prediction is next tested by crack section examination.

Examination of Microstructure. Pore geometry can be examined in crack sections under the microscope. Examination of crack sections 60 - 150 microns in thickness enables a more detailed study of microstructure than standard petrographic thin section analysis. Two to five times the thickness of thin sections, crack sections produce fewer fractures during the sectioning process and provide three dimensional views of microstructure. Under a binocular microscope, the greater thickness of section creates several focal planes, thus allowing the tracking of microfractures and pore spaces through the section. Crack sections allow the recognition of structural features not detectable in thin section (Wilkens et al., 1984).

Crack sections cut to a few microns greater than the desired thickness on a thin section cut-off saw began the sectioning process. Impregnation of sections with a low viscosity blue-stained epoxy in a vacuum chamber defined fracture and pore geometry more sharply. Excess epoxy was planed off after drying and sections were polished smooth on a thin section grinder.

Crack section analysis of the Santa Elena limestone supports the inferences and conclusions made from the velocity, XRD, and porosity/density data. Two of five sections cut from plug ends, X1 and X3, contain several fractures healed with sparry calcite. Sections from X5 and Z7 contain no fractures and only one section, Y7, contains an open fracture. Calcite recrystallization took place, especially in sections filled with masses of crushed fossil debris. Pores are vugular and commonly isolated from one another. Isolated pore space in four sections appears to range from 1 - 4 percent and total pore porosity for all sections ranges from less than a percent to roughly 20 percent. Spheroidal pores dominate: 1) evenly dispersed limonite-filled vugs the size of foraminifera, and 2) equidimensional pores with indistinct boundaries barely visible to the unaided eye. Other than limonite in concentrations less than 0.5 percent, no secondary minerals, such as silica or clay, were observed in crack sections. Therefore, based on the theory predictions of Toksöz et al. (1976) and crack section analysis, existing microfractures within the Santa Elena rock matrix must be healed.

In conclusion, laboratory results corroborate 1) the observations made from the hand specimens (with the unaided eye) that the Santa Elena is composed primarily of calcite and has a variable connected porosity range of 0 to 10 percent, and 2) indicate that although connected porosity varies from 2 to 14 percent in the hand specimens, the Santa Elena rock matrix is homogeneous at the macroscopic scale. Randomly distributed pore space, ellipsoidal to spheroidal in geometry with radii less than 0.5 mm, and absence of open air-filled fractures at the microscopic scale in the Santa Elena, play a role in slightly reducing matrix P- and S-wave velocities. Clay is also a contributing factor to the slight velocity reduction.

The *in situ* seismic data of Reinke and Logan (1983) and Golden et al. (1985) cannot be explained by these models because the laboratory P-wave velocity measurements exceed the *in situ* velocity measurements by approximately 40 to 70 percent. Our next task is to determine the cause this velocity difference.

# V. Application of Fracture Model Theory

The main objective of this research is to investigate the effects macrofractures have on *in situ* seismic wave velocities. In this chapter, we examine the relationship between several measurements of macrofracture orientation, porosity, and density and *in situ* P-, Sv-, and Sh-wave velocities at varying azimuths. Matrix and whole rock parameters, estimated from the laboratory measurements of P- and S-wave velocities, pore porosity, dry bulk and saturated rock densities, and grain density for the Santa Elena limestone, aid in examining this relationship. Laboratory and *in situ* velocity measurements provide the parameters necessary for the application of theoretical models relating pore porosity, fracture porosity, and fracture density, to seismic wave velocities.

A discussion of these various theoretical models immediately follows. Then, model parameters, determined from *in situ* velocity and surface fracture measurements and laboratory data (from chapter IV), are given. Next, application of Thomsen's "Biot-Consistent" model (1985), using solid grain and Biot medium parameters and *in situ* P- and S-wave velocity measurements, predicts total porosity and fracture density along several seismic refraction lines. These predictions are then compared to the *in situ* model parameters determined from surface fracture measurements.

## Model Theory

Several theories, such as the "Noninteracting" (Budiansky and O'Connell, 1980; Kuster and Toksöz, 1974), "Augmented Self-Consistent" (O'Connell and Budiansky, 1977) and "Biot-Consistent" (Thomsen, 1985), model the elastic moduli of porous rocks.

According to Thomsen (1985), these theories share the minimal assumptions concerning the structure of pore space in Biot-Gassmann theory. Biot (1962) derived the basic equations for a porous, linearly elastic, isotropic aggregate at low frequency. Assuming that pore space is interconnected and that the frequency is sufficiently low such that the pore fluid pressure is uniform within a given unit volume $V$, these constituent equations may be written as

$$\bar{\tau} = \mu^{*} \bar{\gamma}, \tag{5.1a}$$

$$\bar{p} = -K^{*} \bar{\theta} + \alpha p_f, \tag{5.1b}$$

$$p_f = -\alpha M \bar{\theta} + M \Delta V_p / V . \tag{5.1c}$$

The bars indicate a volumetric change over $V$, fixed in a solid framework containing many grains and pores. The shear stress $\bar{\tau}$ and pressure $\bar{p}$ are averaged entirely over $V$ for both solid and fluid portions. The shear strain $\bar{\gamma}$ and dilitation $\bar{\theta}$ are also averaged over $V$. The incremental fluid pressure and incremental pore volume are $p_f$ and $\Delta V_p$ respectively; and elastic parameters $\mu^*$, $K^*$, $\alpha$, and $M$ are functions of the stresses and strains and fluid pressure of the initial state. Equations (5.1) implicitly assume that the solid parts of $V$ are homogeneous and isotropic on a microscopic scale.

Gassmann (1951a) interprets, without derivation, the elastic parameters in terms of the solid and the pore space separately. Because Gassmann made a nontrivial extension of Biot's work for elastic parameters, the results are referred to as the Biot-Gassmann formulas. When the medium is in a drained state, equations (5.1a) and (5.1b) reduce to Hooke's equations with shear and bulk elastic moduli (or "frame moduli"), $\mu^*$ and $K^*$, respectively.

For connected pore space, Geertsma (1957) and Nur and Byerlee (1971) show that

$$\alpha = 1 - \frac{K^*}{K_s}, \tag{5.2a}$$

and

$$M = \frac{K_s}{\alpha - \phi}, \tag{5.2b}$$

where $K_s$ and $\phi$ are the incompressibility of the solid grains and total porosity, respectively.

The Biot-Gassmann formulation (1941) makes two well-known predictions for elastic moduli of porous rocks: 1) the shear modulus of an unsaturated rock (permeated by a compressible fluid, e.g., gas) equals that of the same rock saturated with liquid and 2) the unsaturated and saturated bulk modulus differ by a defined amount. The theory of Toksöz et al. (1974), developed for small values of porosity and fracture density ($[c(\alpha_m)]/\alpha_m < 1$), is not consistent with the latter of these two predictions.

Similar to Toksöz et al. (1974) but in agreement with both Biot-Gassmann predictions, the noninteracting theory of Budiansky and O'Connell (1980) combines the standard theory for the elasticity of a solid isotropic matrix with a dilute concentration of spherical pores (Eshelby, 1957) and the corresponding theory for dilute concentrations of thin, ellipsoidal fractures (Bristow, 1960). The Budiansky and O'Connell model (1980) assumes 1) fluid pressure equalization between the two populations, and 2) a surrounding medium identical to that of the solid grains. Thus no elastic interaction takes place between neighboring heterogeneities spaced far apart. When no elastic interaction takes place the effects on the moduli are additive and lead to relationships linear in porosity or in fracture density. However, because high values of porosity and fracture density violate its assumptions, the theory is not applicable to the Lajitas data. (The next section, Model Parameters, gives fracture porosity estimates and fracture density estimates determined through the application of equation (5.41) by using fracture length and width parameters measured at the surface in outcrop.)

The augmented self-consistent model (cf., Budiansky and O'Connell, 1976; O'Connell and Budiansky, 1974, 1977; Berryman, 1980) statistically calculates the interaction between neighboring inhomogeneities. This theory assumes that the solution of the noninteracting Budiansky and O'Connell (1980) model for a single pore enveloped, not by the solid, but by a uniform medium with the elastic properties of the "whole rock" yields the effect of many spherical pores. This model allows for large porosity and/or fracture density but only agrees with Biot-Gassmann theory in the case of no fractures.

Thomsen (1985) provides the mathematical relationships and discusses the Biot-Gassmann theory and noninteracting and augmented self-consistent models in greater detail. He also proposes a "Biot-Consistent" model, applicable at low frequencies with no limits on fracture density and total porosity.

The Biot-Consistent model includes a third dependent state variable not included in the noninteracting and self-consistent models but recognized in Biot-Gassmann theory--the fluid pressure $p_f$. In the undrained case $p_f$ is equivalent to the incremental pore volume $\Delta V_p / V$. (See equations (5.1).) The corresponding modulus can be defined as the pore incompressibility $K_p$ :

$$K_p \equiv -V_p \frac{\bar{p}}{\Delta V_p} = K' \frac{\bar{p}}{p_f} . \tag{5.3}$$

Consequently, three rather than two characteristic moduli ($\mu$, K, $K_p$) specified at any particular value of K' (the saturating fluid bulk modulus) define the elastic response at all saturations for a "Biot medium". Hence in the model theory for a porous rock, the surrounding medium of the noninteracting model possesses the three moduli of the Biot medium.

Considering a Biot medium with a substantial equant porosity and fracture density, all interconnected, Thomsen (1985) relates the shear and bulk moduli $\mu$ and K, respectively, to:

$$\mu(p_f) = \mu_s \left[ 1 - \frac{\phi_p}{1 - b_B} - B_B \varepsilon \right] , \tag{5.4a}$$

and

$$K(p_f) = K_s \frac{1 - \left(1 - \frac{K'}{K_s}\right)\left(\frac{\phi_p}{1 - a_B} + A_B \varepsilon\right)}{\left[ 1 + \frac{K'}{K_B} \left( \frac{a_B}{1 - a_B} \frac{\phi_p}{\phi} + \frac{A_B \varepsilon}{\phi} \right) \right]} . \tag{5.4b}$$

Defining the above parameters in terms of Poison's ratio of the Biot medium (subscript B):

$$a_B \equiv \frac{1 + \nu_B}{3(1 - \nu_B)} , \tag{5.4c}$$

and

$$b_B \equiv \frac{2}{15} \frac{4 - 5\nu_B}{1 - \nu_B} , \tag{5.4d}$$

for the pores, and

$$A_B \equiv \frac{16}{9} \frac{1 - \nu_B^2}{1 - 2\nu_B} , \tag{5.4e}$$

and

$$B_B \equiv \frac{32}{45} \frac{(1 - \nu_B)(5 - \nu_B)}{(2 - \nu_B)} , \tag{5.4f}$$

for the fractures. These functions depend on Poison's ratio $\nu_b$ for the Biot medium:

$$\nu_B \equiv \frac{1 - {}^{2\mu_B}/_{3K_B}}{2 + {}^{2\mu_B}/_{3K_B}} . \tag{5.4g}$$

For the shear and bulk modulus of the Biot medium, $\mu_b$ and $K_b$:

(5.4h)
$$\mu_B = (VS_B)^2 \rho_B ,$$

and

(5.4i)
$$K_B = \left[(VP_B)^2 - \frac{4}{3}(VS_B)^2\right] \rho_B ,$$

where

(5.4j)
$$\rho_B = \phi_B \rho_f + (1 - \phi_B)\rho_s$$

and $\phi_B$ is the porosity of the Biot medium and $\rho_f$ and $\rho_s$ are the density of the fluid and solid grains respectively. The total porosity $\phi$ equals the sum of the total fracture porosity $\phi_c$ and pore porosity $\phi_p$

(5.4k)
$$\phi = \phi_c + \phi_p ,$$

and the fracture density $\varepsilon$ is related to $\phi_c$ (for circular, i.e., penny-shaped fractures) by

(5.4l)
$$\varepsilon = \frac{3}{4\pi}\frac{\phi_c}{\lambda} ,$$

where the thickness/diameter of the fractures equal the aspect ratio $\lambda$. For a spectrum of fracture shapes the average fracture density over the spectrum, $\langle\varepsilon\rangle$, replaces $\varepsilon$ in equations (5.4a) and (5.4b). The shear and bulk moduli of the solid grains, $\mu_s$ and $K_s$ , respectively equal:

(5.4m) $$\mu_s = (VS_s)^2 \rho_s,$$

and

(5.4n) $$K_s = (VP_s)^2 \rho_s - \frac{4}{3}(VS_s)^2 \rho_s.$$

In the drained case ($p_f = 0$), as according to the Biot-Gassmann theory that the shear modulus drained equals the shear modulus saturated

(5.5a) $$\mu_B(p_f) = \mu_B(0) = \mu^*_B = \mu^*,$$

and the *in situ* bulk modulus $K(p_f)$ reduces to

(5.5b) $$K(p_f) = K(0) = K_s \left[1 - \frac{\phi_p}{1 - a^*_B} - A^*_B \phi\right] = K^*$$

where "starred" parameters, such as $a^*_B$, $A^*_B$ and $\mu^*_B$, refer to the Biot medium in the drained case.

Note that in the drained state, the equations of motion define elastic-wave velocities in terms of moduli and density $\rho^*$:

(5.6a) $$VP^* = \left[\frac{\left(K^* + \frac{4}{3}\mu^*\right)}{\rho^*}\right]^{1/2},$$

and

$$VS^* = \left[\frac{\mu^*}{\rho^*}\right]^{1/2}, \tag{5.6b}$$

with the density given by

$$\rho^* = \phi\rho_f + (1-\phi)\rho_s . \tag{5.6c}$$

(The quantities $VP^*$ and $VS^*$ represent *in situ* seismic wave velocities.) Substituting equation (5.6c) into equations (5.6a) and (5.6b) and solving for $\mu^*$ and $K^*$:

$$\mu^* = (VS^*)^2\rho_s - (VS^*)^2\rho_s\phi , \tag{5.7a}$$

and

$$K^* = (VP^*)^2\rho_s - \frac{4}{3}(VS^*)^2\rho_s + \left[\frac{4}{3}(VS^*)^2\rho_s - (VP^*)^2\rho_s\right]\phi . \tag{5.7b}$$

Equating equations (5.7b) to corresponding equation (5.5b) and simplifying:

$$\phi = \frac{K_s\left[1 - \frac{\phi_p}{1 - a^*_B}\right] + \rho_s\left[\frac{4}{3}(VS^*)^2 - (VP^*)^2\right]}{K_s A^*_B + \rho_s\left[\frac{4}{3}(VS^*)^2 - (VP^*)^2\right]} , \tag{5.8a}$$

and

$$\varepsilon = \frac{\mu_s\left[1 - \frac{\phi_p}{1 - b^*_B}\right] + \left[(VS^*)^2\rho_s(\phi - 1)\right]}{\mu_s B^*_B} . \tag{5.8b}$$

Thus, application of the Biot-Consistent model using parameters determined from geophysical field measurements (VP* and VS*) and laboratory measurements ($\rho_s$, $K_s$, $\mu_s$, $a^*_B$, $b^*_B$, $A^*_B$, $B^*_B$, and $\phi_p$) predicts fracture density and fracture porosity ($\phi = \phi_p + \phi_c$) in the field.

## Model Parameters--*In Situ* Measurements

The main objectives of the geophysical field work were 1) to measure *in situ* P- and S-wave velocities at varying azimuths using shallow refraction seismic methods and 2) to select unit volumes at or near the chosen refraction site and count and measure the length and orientation of each observed fracture trace. Fracture density and fracture porosity estimates made from the surface fracture length and width measurements give a comparison to those predicted from the Biot-Consistent model using *in situ* velocity measurements and parameters derived from the laboratory data for the Santa Elena limestone. Determining P- and S-wave velocities along refraction spreads aligned parallel and perpendicular to the strikes of the dominant observed fracture planes tests for azimuthal anisotropy.

Data Acquisition. In this study, an iron plate and hammer provided both the compressional and shear source. The compressional source, according to the representative sampling of field seismograms shown in Appendix D, generated a range of frequencies from 200 - 300 Hz and wavelengths from 9

- 15 m in the Santa Elena limestone. The shear source (Figure 5.1) used in these experiments transmitted a maximum horizontal range of approximately 50 m (as opposed to a 100 m horizontal range for the compressional source) and generated frequencies from 75 - 330 Hz and wavelengths from 5 - 35 m.

To observe slight anisotropic effects in fractured isotropic and homogeneous material, the source must generate wavelengths much greater than the fracture size and separation distance between fractures (Backus, 1962). Wavelengths ranging from 5 to 35 m are not much greater than the 35 - 40 m separation distance measured between macrofractures on the lineation map. However, the 2.5 - 30.5 cm range of separation distances measured between fractures observed in outcrop ranges from 0.0007 - 0.007 times the size of these wavelengths. These smaller scale fractures (overlapping the lower macrofracture and upper microfracture boundary scale limits) vary 0.1 - 0.3 cm in width and 1 - 110 cm in length. Consequently, the high frequency content and short range of the shear and compressional source constrained the study to the examination of the effects that the fractures observed in outcrop have on *in situ* P- and S-wave velocity.

Figure 5.2 shows the geometrical arrangement of refraction lines used to measure P- and S-wave velocities at several azimuths and locates the unit volumes chosen for the fracture orientation and density and fracture porosity

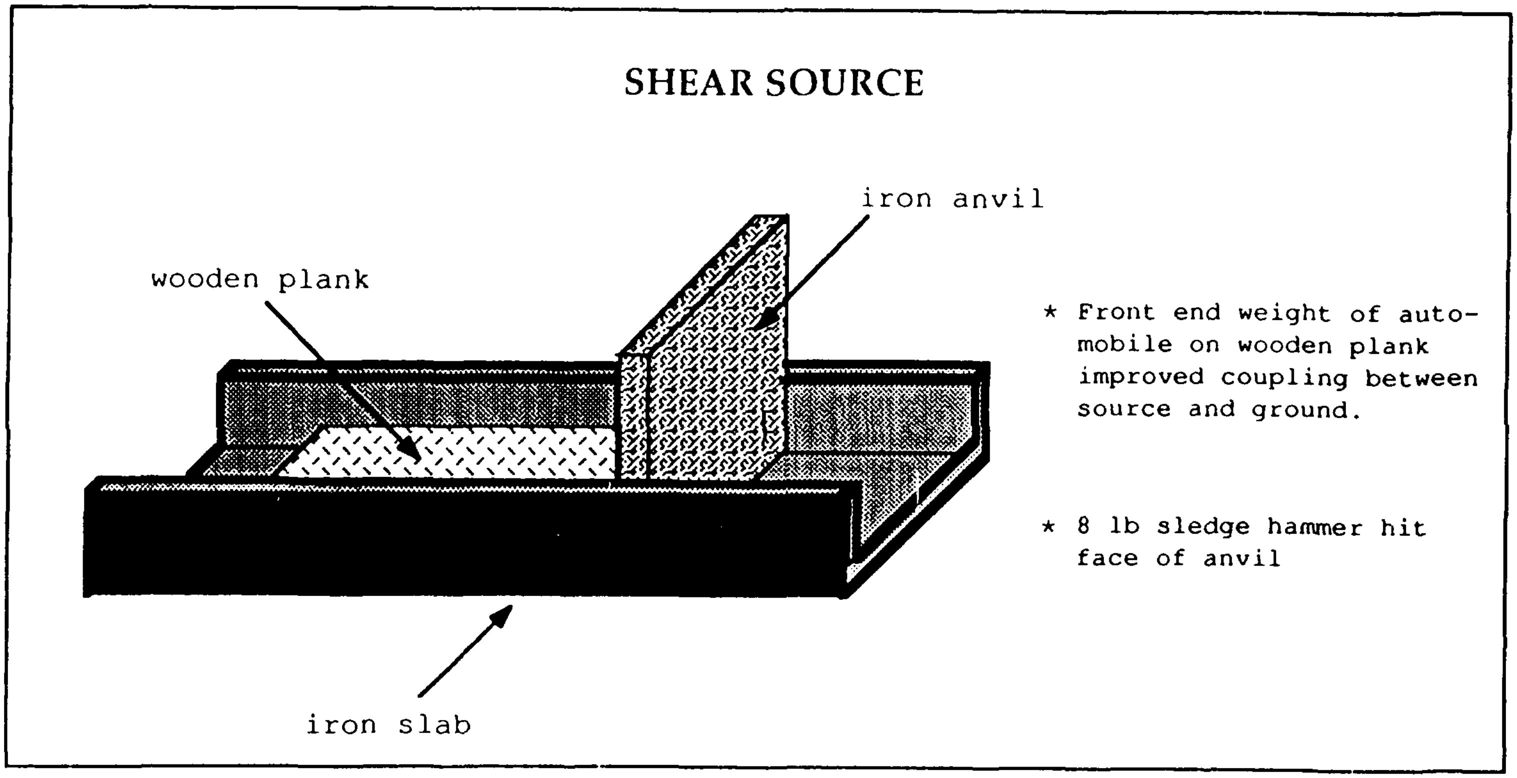


Figure 5.1 Shear source used for refraction work at the Lajitas Texas site in December 1988.

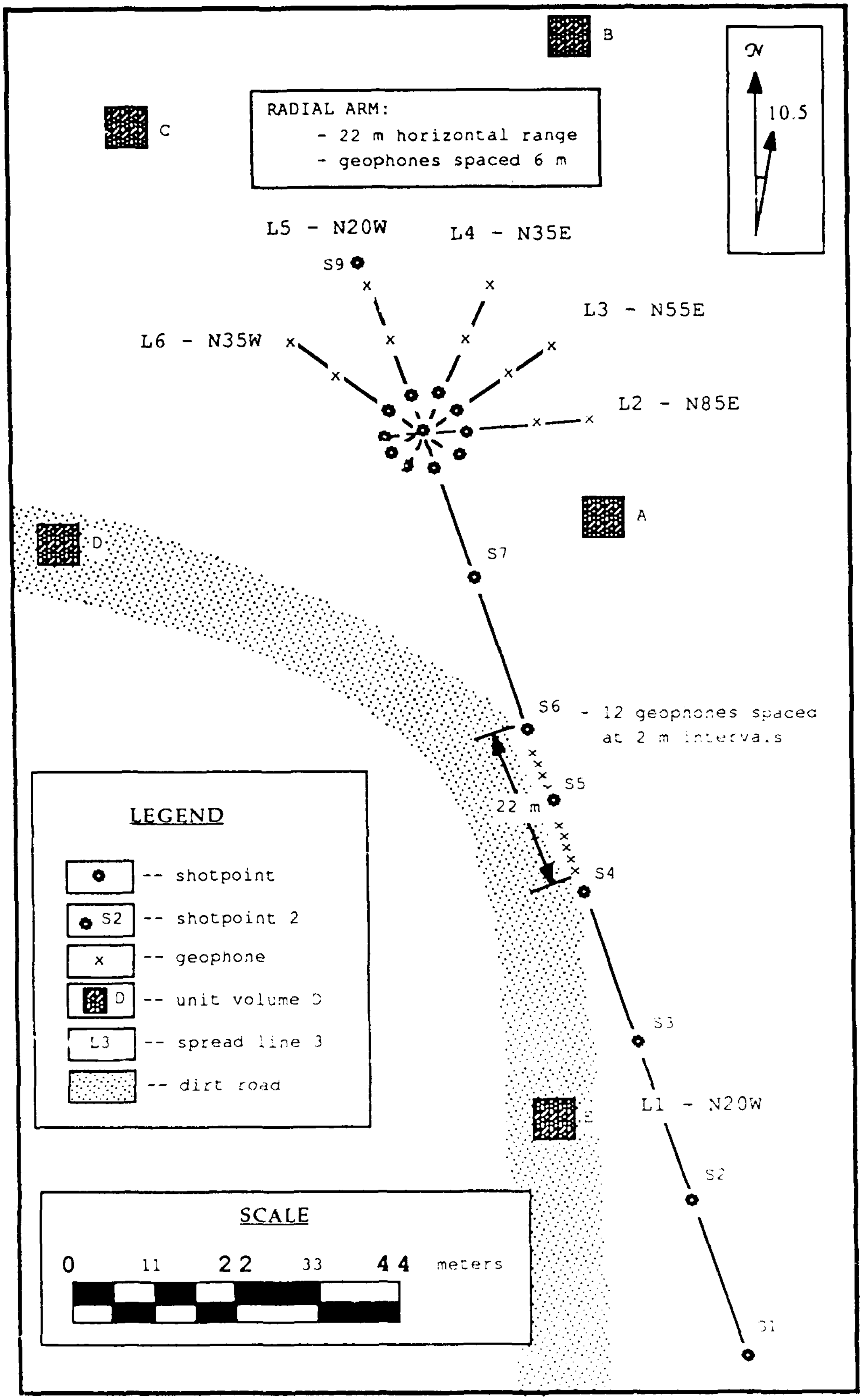


Figure 5.2 Map showing location and orientation of unit volumes A - E, shotpoints, and seismic spreads.

determinations. The refraction lines arranged in a "star-like" fashion aided in distinguishing azimuthal velocity variations due to fractures, from velocity variations due to stratigraphic discontinuities (Telford et al., 1976; Crampin 1984b); whereas reversed refraction spreads facilitated the detection of shingling effects already observed at the site (Reinke et al., 1983). Minimizing effects of shear-wave splitting by orienting refraction lines with major fracture trends helped in recognizing the effects of anisotropy (Crampin, 1978, 1981, 1984a, 1985, Crampin et al., 1984). In addition, measurement of P- and S-wave velocities perpendicular and parallel to dominant air-filled fracture sets tested for azimuthal anisotropy (Lynn and Thomsen, 1986; Rai and Hanson, 1986).

Fracture orientations measured in unit volumes A - E trend to the NNW and ENE (Figure 5.3a-e). Figure 5.3f shows the relationship between the six refraction line orientations and the cumulative representation of fracture trace orientations observed in unit volumes A - E. Excluding spread 4, all refraction lines trend subparallel to one of the observed sets of fracture planes.

For spread 1, high resolution profiles were obtained by using a 2 m geophone spacing and a 12 channel analog-to-digital recorder (sampling at 10 μs intervals), and by making several in line shots offset approximately 22 m from one another on both sides of the spread. The mobile source and

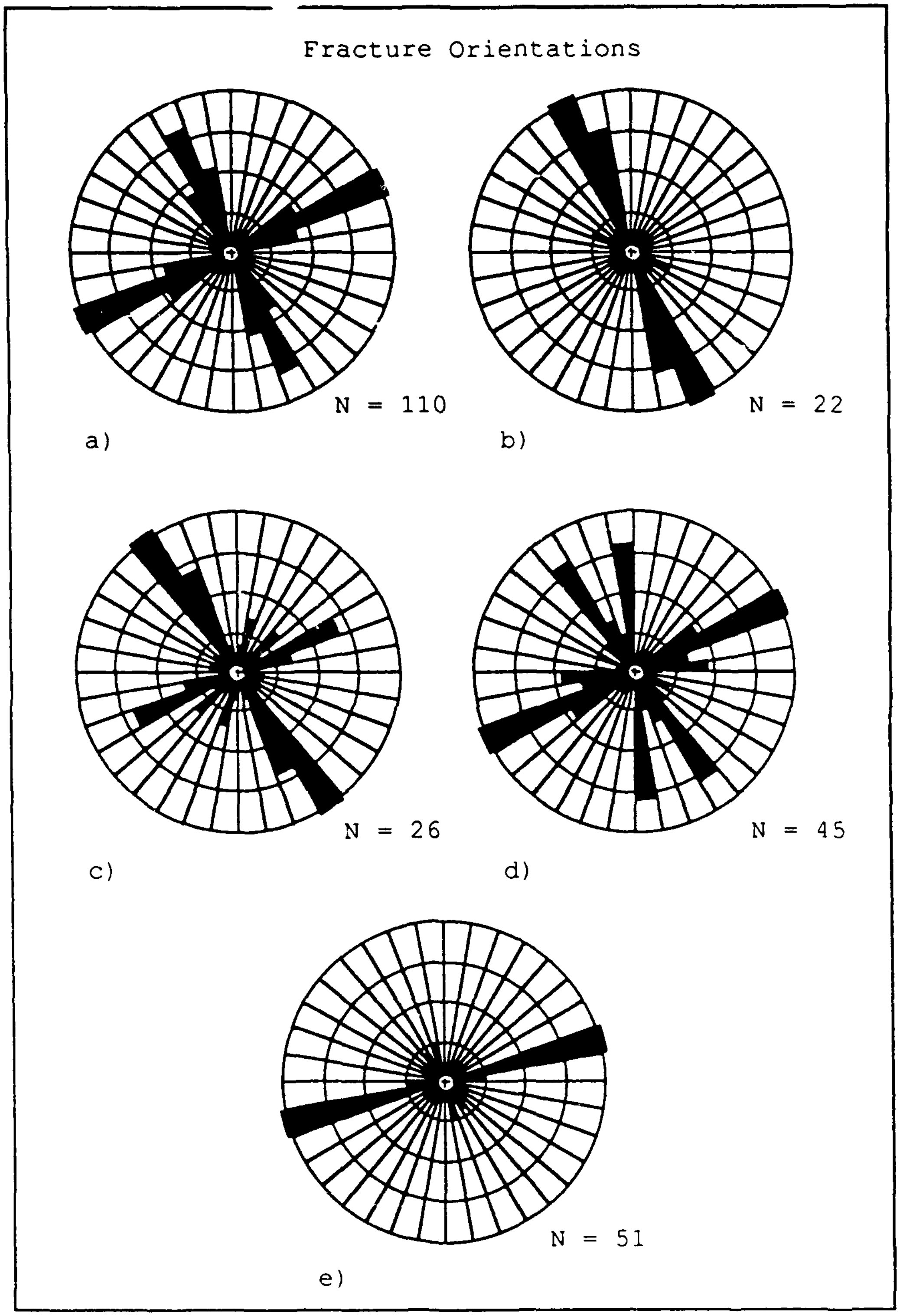


Figure 5.3a-e Observed strikes of fracture planes in unit volumes a) A, b) B, c) C, d) D and e) E.

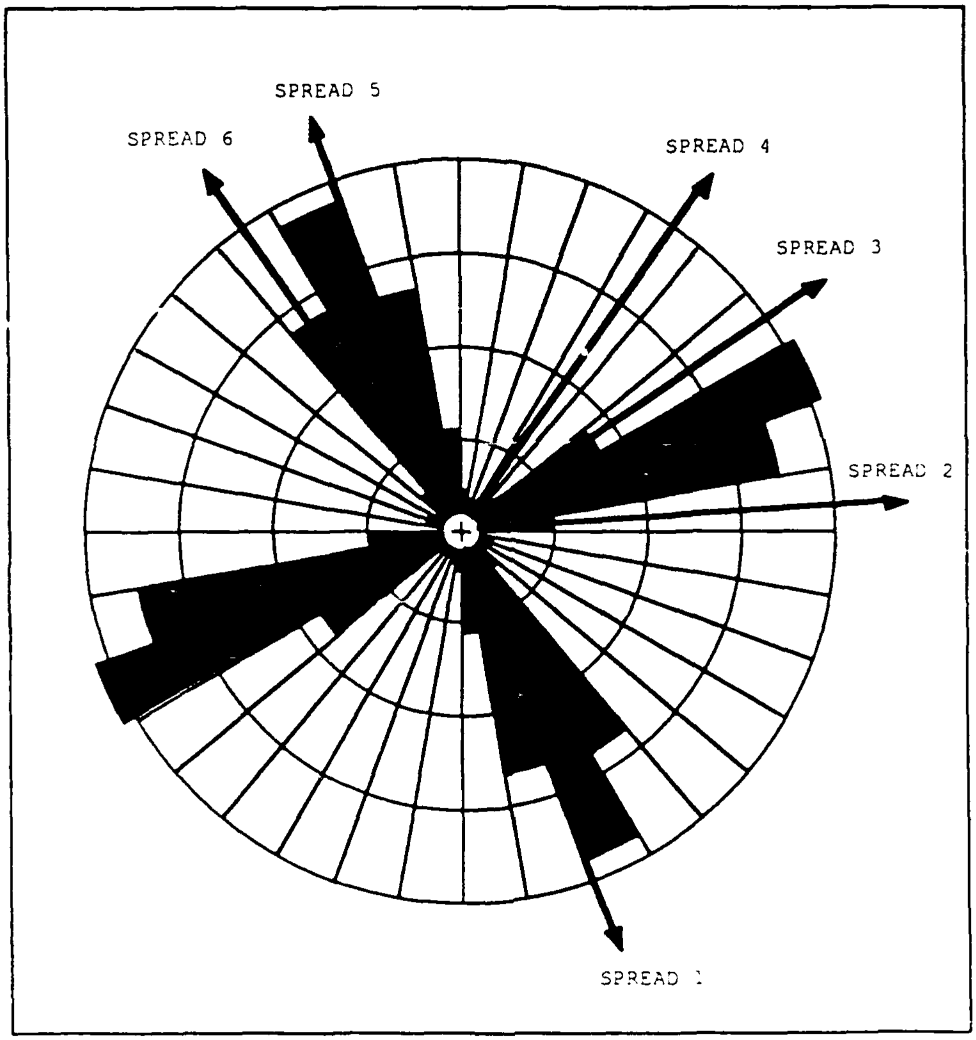


Figure 5.3f Illustration showing refraction line orientation versus a cumulative representation of observed fracture orientations in unit volumes A - E.

stationary receivers allowed for substantial horizontal coverage in a short period of time. The multiple shotpoints for each spread also aided in resolving the ambiguities inherent in the seismic refraction travel time curves based on first arrivals (Ackermann et al.,1986). Limited time and take-out cord between channel hook-ups constrained the radial array, comprised of spreads 2, 3, 4, 5 and 6, to two geophones per arm. In each radial arm, spacing between geophones equaled 6 m. Multiple shotpoints, placed 10, 15, and 20 m from the nearest geophone in each radial spread, yielded six first arrival picks per line.

Vertical 10 Hz PE3 Sensorphones and horizontal 14 Hz Mark Product phones measured velocity along each spread. The horizontal phones measured shear wave velocities polarized parallel and polarized perpendicular to each S-wave propagation path.

Rocky surface conditions at the site necessitated the burial of horizontal phones in small holes filled with fast quenching grout (Krohn,1984). Using nuts and bolts rather than spikes, horizontal phones were oriented and leveled in wet grout and later removed by loosening the nuts (Figure 5.4). The Mark Product phones required 24 pitch, 3/8" diameter nuts and bolts, with bolts measuring 2 - 3 inches in length. The fast quenching grout, termed "Jug Plug, the Mighty Miracle Mix", set within 15 minutes. Two and three-quarter pounds of Type I or III Portland cement, 0.69 lbs of

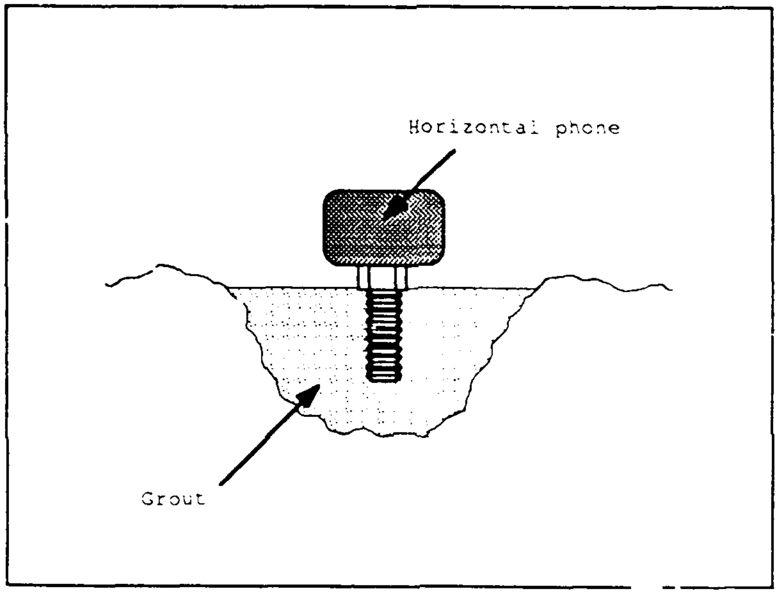


Figure 5.4 Illustration of method used to reduce geophone ground coupling at low frequencies.

CalSeal (gypsum) cement, 3.44 lbs of clean masonry sand, and 1.72 lbs (or 0.21 gals) of cool water made 1/15 $ft^3$ (3" X 6" X 6") of "Jug Plug". Developed for the rapid construction of seismometer vaults and good long term leveling of instruments, this grout has sufficient viscosity to cause the mixture to seek its own level when poured (Lewis, 1987). Hence, the vertical phones were placed on small grout pods using triangular stands (or T1F snow bases). Due to limited field time, geophones were only grouted for spread 1. Note that geophone spikes penetrated the surface more easily in the region of the radial array.

P- and S-Wave Velocity. Using refraction techniques, Reinke and Logan (1983) measured P-wave velocity along an 1100 m line oriented subparallel to and possibly overlapping spread 1 (and 5) of this study. Reinke and Logan (1983) spaced 24 geophones at 33.5 m intervals and used an 8 lb Kine-Stick two component explosive source, buried just below the surface, and offset 33.5 and 300 m from the nearest geophones for forward and reverse profiles respectively. They then applied an automated seismic refraction interpretation program (SIPT) to determine the number of subsurface layers represented by plotted travel times picked to the nearest millisecond. This program, developed by the US Bureau of Mines, uses regression and ray tracing techniques to produce a subsurface depth-velocity profile (Scott, 1973). A jagged interface between average velocities of 2.907 km/s and 3.779 km/s resulted in an attempt by SIPT to fit large time gaps present in the arrival times from the forward shot. Because of the fairly simple near surface stratigraphy and structure, Reinke and Logan (1983) speculate that "shingling", as described by Spencer (1965), causes the observed time gaps. Shingling occurs when "peaks and troughs move forward through the envelope which defines the refracted arrival. In this process, the amplitude of the first extremum decreases and it is eventually lost in the noise. At this offset where extremum is lost, there is a discontinuity in the time-distance curve and a new shingle is added corresponding to a later, larger amplitude extremum" (Spencer, 1965). However, this phenomenon does not explain the absence of time gaps in their reversed profile. Disregarding the forward profile as invalid and using only travel times from the reversed profile for interpretation yielded no significant P-wave velocity interface in the Santa Elena limestone. The P-wave velocity averages approximately 3.477 km/s, as indicated for the Santa Elena by the reversed shot.

Travel time curves representing P- and Sv-wave first arrivals for spread 1 of this study behave similarly (Figures 5.5 - 5.7). The forward and reversed profiles for spread 1 are laid out in the same direction as the 1100 m forward and reversed profiles of Reinke and Logan (1983). "Shingling" occurs in all profiles. Understanding of this shingling

P-WAVE TRAVELTIME CURVES
(Spread 1)

FORWARD PROFILE

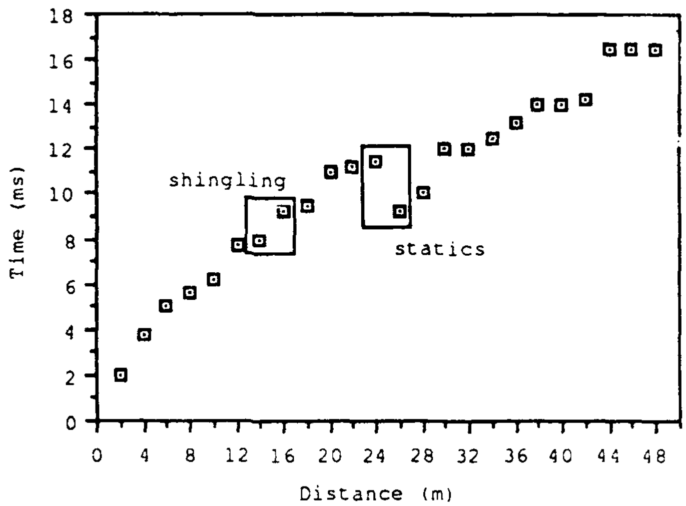


a)

REVERSE PROFILE

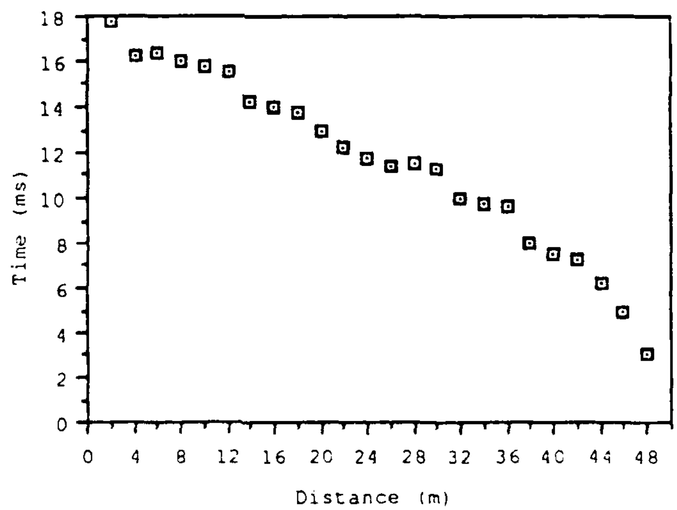


b)

Figure 5.5a-b P-wave first arrival picks for a) forward and b) reversed profiles of spread 1.

SV-WAVE TRAVELTIME CURVES
(Spread 1)

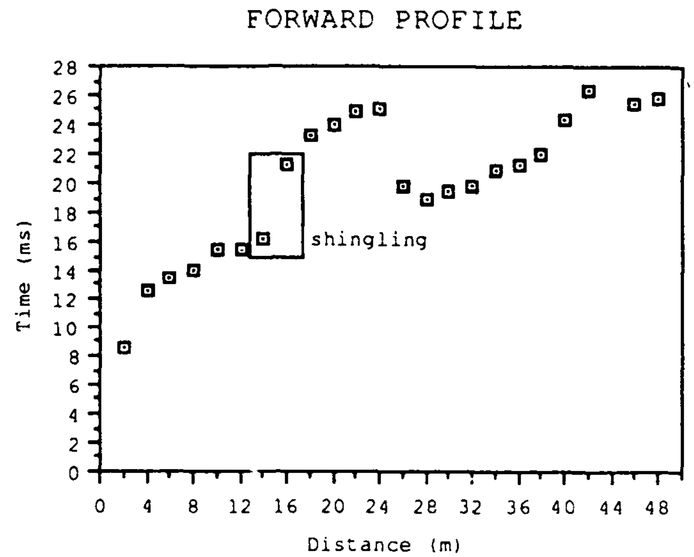


a)

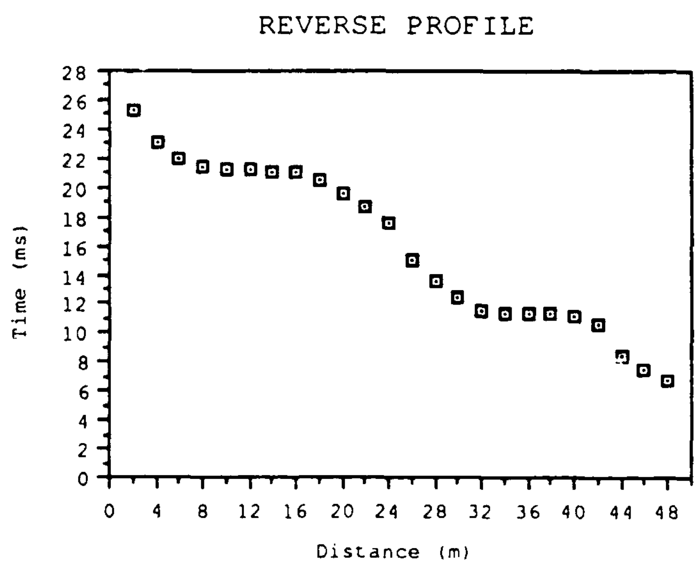


b)

Figure 5.6a-b Sv-wave first arrival picks for a) forward and b) reversed profiles of spread 1.

SH-WAVE TRAVELTIME CURVES
(Spread 1)

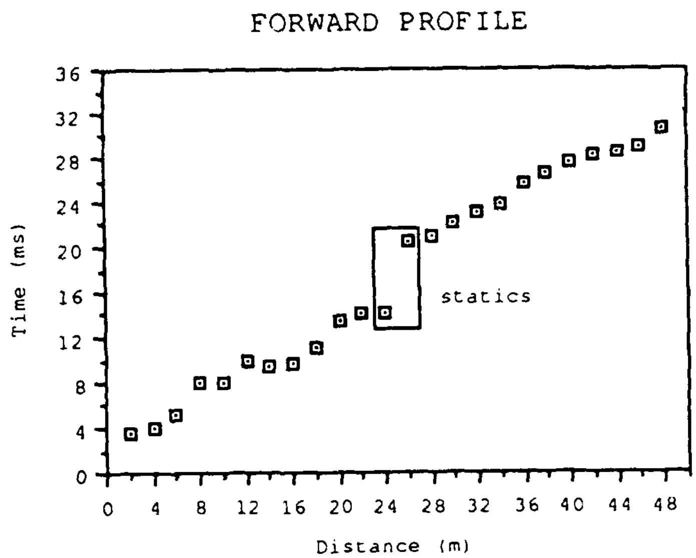


a)

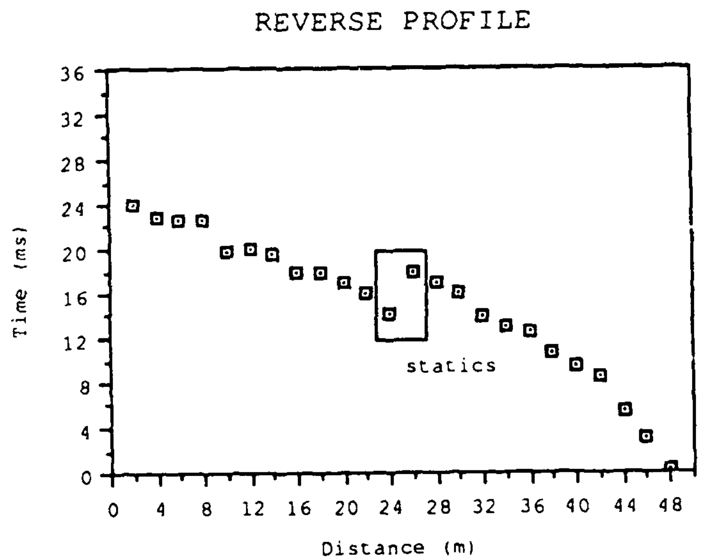


b)

Figure 5.7a-b Sh-wave first arrival picks for a) forward and B) reversed profiles of spread 1 phenomenon requires further study outside the scope of this research.

Static effects, such as those resulting from topographic gradients, may also cause time gaps. Source offsets along a slight uphill gradient extending from S1 to S7 produced time gaps. Using expressions for dipping beds with discrete velocities (Dobrin, 1976), one can obtain the change in elevation and the velocity of the refracting medium from the direct arrival ($V_0$) and the forward and reversed slowness and intercept times of the refractor (assuming the refractor is horizontal). Using rough intercept time estimates (±4 ms), these expressions approximate an average change in elevation of 1.6 m. A change in elevation of 1.5 m, determined in the field using hand leveling techniques with a Brunton compass, comes within 10 percent of this 1.6 m estimate. The average refractor depth ranges from 3.2 ± 1.3 m (or 10.5 ± 4.2 ft) at shotpoint S3 to 4.8 ± 1.9 m (or 15.7 ± 6.2 ft) at shotpoint S7. First arrival times picked to the nearest ms yield P-, Sv-, and Sh-wave velocities equal to 3.02 ± 0.6 km/s, 2.53 ± 0.5 km/s, and 2.24 ± 0.4 km/s respectively. Broadened peaks, due to irregularity and weathering of the rock surface, and variations in horizontal and vertical velocity of overburden may have introduced error in the first arrival travel time picks (Domzalski, 1956). Over relatively short horizontal distances (22 - 44 m), first arrival times picked from broad peaks to the nearest millisecond introduced as much as 20 percent error in the velocity measurements. In contrast, travel times picked to the nearest millisecond and measured over greater horizontal distances produced less than 1 percent error in the velocity measurements determined for the reversed 1100 m line by Reinke and Logan. Also, narrower pulse widths produced by the explosive source made first arrival picks more obvious in their study.

In the radial array, the minimum and maximum compressional wave velocity measurements (based on error introduced by first arrival picks) equal 2.53 ± 0.5 km/s and 3.35 ± 0.7 km/s; whereas those for shear wave velocity equal 1.59 ± 0.3 km/s and 2.70 ± 0.5 km/s (Figure 5.8). Median values equal 2.99 ± 0.6 km/s and 2.22 ± 0.4 km/s for P- and S-wave velocities respectively. *In situ* P-wave velocities are 40 to 60 percent less than the median laboratory $V_P$ measurement of 5.68 km/s; whereas for S-waves, the median $V_S$ laboratory measurement of 3.10 km/s and *in situ* velocities differ by 20 to 50 percent. Because a compositionally homogeneous medium with air-filled pores (spheroidal to ellipsoidal in geometry) has relatively little effect on shear wave propagation (in comparison to compressional waves), open [illegible]-filled fractures most likely cause the substantial drop in [illegible] P- and S-wave velocities. The $V_P/V_S$ values of 1.10 and 1.24 in line 2 and 3 seem low. However, an increase in $V_P$ and decrease in $V_S$ by 20 percent raises these values to 1.66 and 1.86. Ignoring error, $V_P/V_S$ ranges from 1.10 to 1.97 for spreads 2 through 6.

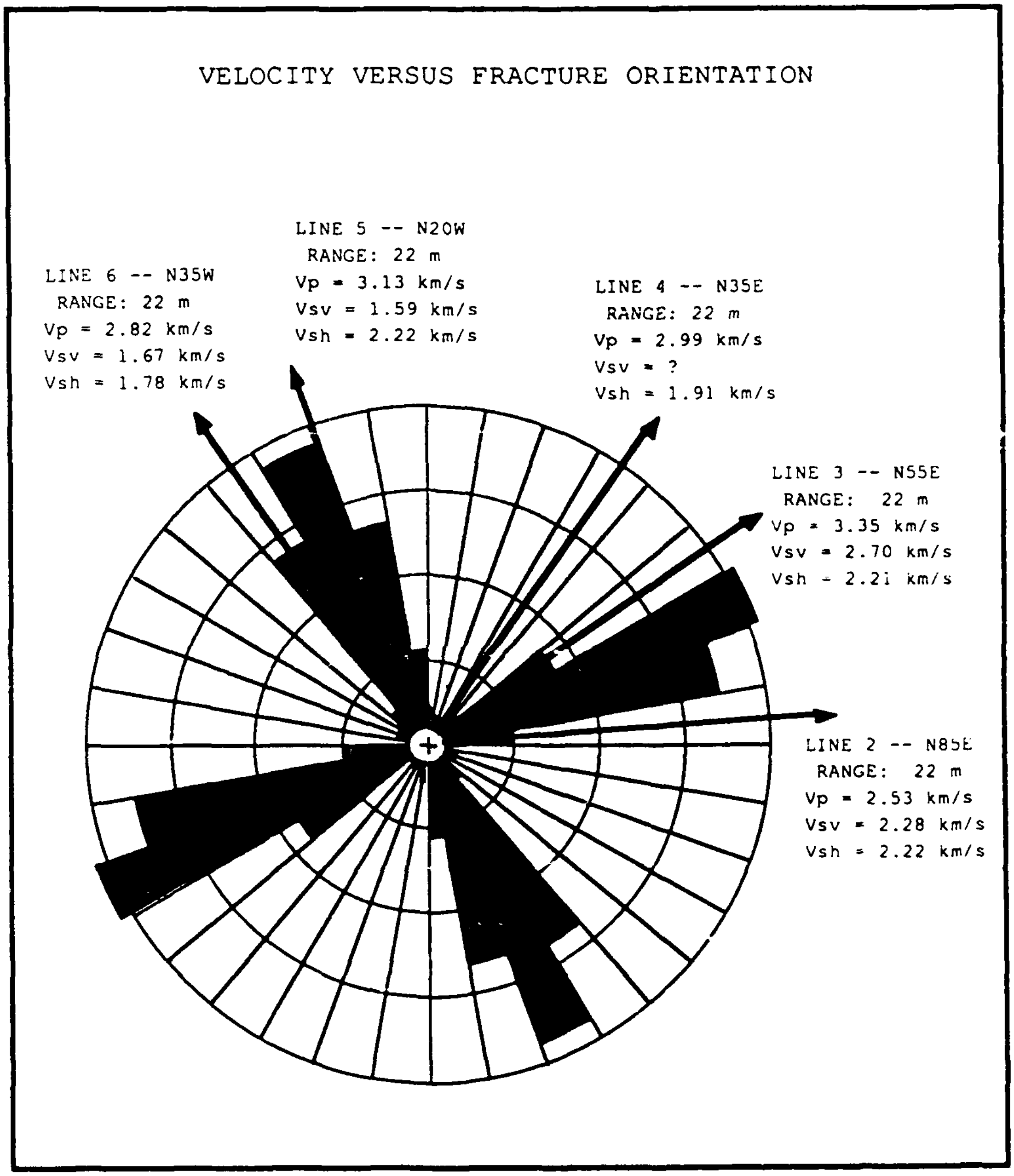


Figure 5.8 *In situ* P-, Sv- and Sh-wave velocity versus fracture orientation measured in units A - E.

If error is ignored, higher radial velocities along northeasterly spreads (in comparison to their transverse counterparts) suggest azimuthal anisotropy. Compressional waves propagating parallel to dominant fracture trends, N20W and N55E, exceed velocities measured along lines fringing the range of dominant fracture trends (N35W, N85E) or lines parallel to no fractures at all (N35E) by approximately 5 to 25 percent. P-waves propagating to the northeast exceed those propagating to the north northwest by 7 to 15 percent in velocity. Other work done at the Lajitas seismic station suggests that incoming teleseismic waves from the east travel at faster velocities than those coming from the north (Golden, personal communication). Therefore, easterly fracture sets may have slightly more effect on velocities than northerly sets.

However, the error introduced in line 1 also applies for lines 2 through 6. In addition, few data points defining the radial profiles (2 points for every shot), and minor static problems originating from varying shotpoint locations further cloud the picture. High winds, a crude shear source, and ungrouted geophones in the radial array contribute further to the error. Thus, azimuthal anisotropy can not be determined with certainty. At most, one can infer that a dense network of open air-filled fractures lower the expected wave velocities.

Thomsen speculates that a medium with open air-filled orthogonal fracture sets, approximately equal in prominence, is statistically isotropic (personal communication). The next two sections, Surface Fracture Porosity Estimates and Surface Fracture Density Estimates, closely examine the geometrical and spatial distribution of fractures exposed at the surface within the seismic refraction array boundaries.

Surface Fracture Porosity Estimates. Recall equation (4.24):

$$\phi_c = \sum_{n=1}^{N} \phi(\alpha_n) .$$

Now assume a spectrum and the volume V, given by surface area A and depth d:

$$\phi_c = \sum_{n=1}^{N} \phi(\alpha_n) = \sum_{n=1}^{N} \frac{c(\alpha_n)}{V} = \sum_{n=1}^{N} \frac{c(\alpha_n)}{Ad} . \tag{5.9}$$

For vertical fractures extending to the unit volume depth d, estimating each opening of fracture traces exposed at the surface in terms of an ellipse with major and minor axis $a_n/2$ and $b_n/2$ yields a total fracture porosity $\phi_c$

$$\phi_c = \frac{\pi}{4Ad} \sum_{n=1}^{N} a_n b_n d = \frac{\pi}{4A} \sum_{n=1}^{N} a_n b_n , \tag{5.10}$$

where $a_n$ and $b_n$ equal the measured length and width of a single fracture trace exposed at the surface (Figure 5.9). This relationship holds when the total fracture porosity for a given unit surface area represents fracture porosity throughout the region of interest.

Outcrop exposure at various locations within the seismic refraction array boundaries constrained coverage of each unit surface area. The surface areas range from 2270.96 $cm^2$ to 13548.36 $cm^2$:

Unit A = 13548.36 $cm^2$
Unit B = 2270.96 $cm^2$
Unit C = 5903.21 $cm^2$
Unit D = 3860.00 $cm^2$
Unit E = 6350.79 $cm^2$

Observed fracture widths in unit volumes A - E average around 0.2 and 0.3 cm. Holding the fracture width constant at 0.2 cm, $\phi_c$ equals

$$\phi_c = \frac{(0.2)\pi}{4A} \sum_{n=1}^{N} a_n$$

(5.11)

$$\approx \frac{0.1571}{A} \sum_{n=1}^{N} a_n .$$

Calculating the fracture porosity and aspect ratio for each individual fracture in a given unit area (before summing) yields a spectrum of fracture populations:

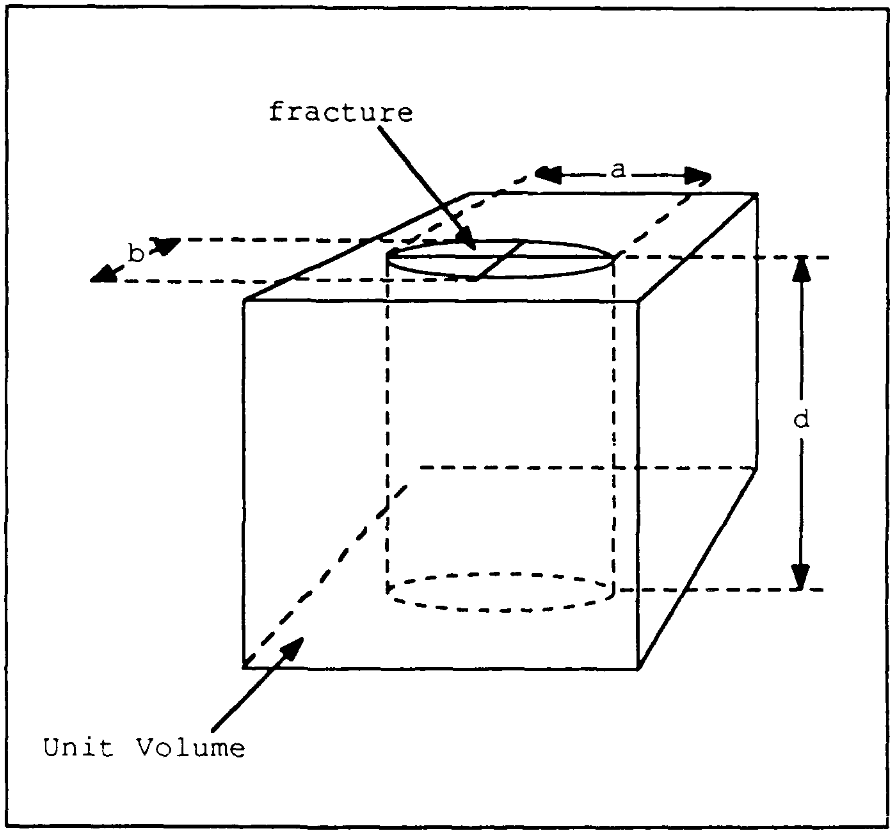


Figure 5.9 Illustration showing fracture parameters a, b, and d, for a given unit volume.

$$\phi_c(n) = \frac{0.1571}{A} a_n \text{ ; for } n = 1, 2, 3, \ldots, N \tag{5.12a}$$

where for every fracture "n", $\phi_c(n)$ is associated with an aspect ratio $\alpha_n$:

$$\alpha_n = \frac{b_n}{a_n} = \frac{0.2}{a_n} . \tag{5.12b}$$

That is, every fracture with length $a_n$ and width $b_n$ and depth d, is associated with a fracture volume $a_n b_n d$ and an aspect ratio $b_n/a_n$. For each measured fracture in units A through E, the aspect ratio and volume contribution were obtained using equations (5.12). The fractures range from 0.002 to 0.157 in aspect ratio. For each unit area, these fractures were grouped by powers of ten in aspect ratio ($10^{-3}$, $10^{-2}$, $10^{-1}$, and $10^{0}$) and their fracture volumes summed to yield $c(\alpha_m)$, the total fracture volume for each group. Figure 5.10 associates the fracture porosity (or concentration) $c(\alpha_m)/Ad$ with the average aspect ratio $(b_n/a_n)/N$ for each group. Two populations dominate--fracture populations with average aspect ratios of 0.024 and 0.005 with concentrations ranging from 0.33 - 1.55 percent and 1.12 - 2.87 percent respectively (Table 5.1a). The total fracture porosity ranges from 1.88 - 3.93 percent with a median value equal to 3.05 percent. Similarly, at fracture widths equal to 0.3 cm, $\phi_c$ equals

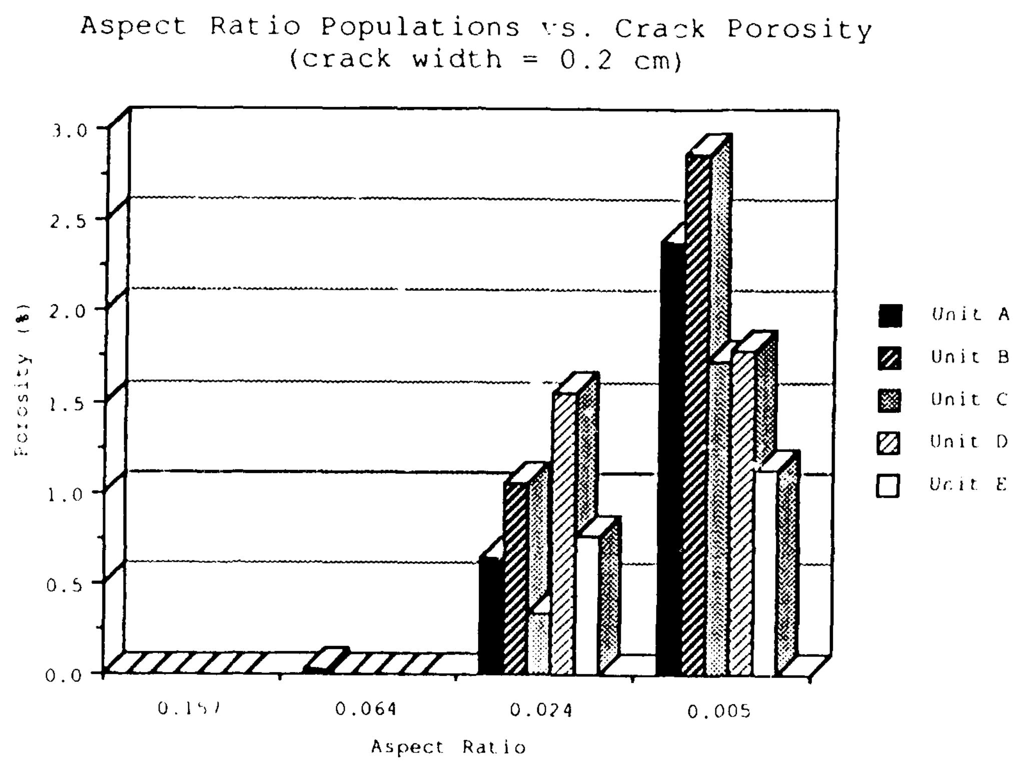


Figure 5.10 Concentration of crack populations having crack widths equal to 0.2 cm.

TABLE 5.1a

ASPECT RATIO VS. CONCENTRATION (fracture width = 0.2 cm)

| Aspect Ratio | Concentration (%) Unit A | Unit B | Unit C | Unit D | Unit E |
|---|---|---|---|---|---|
| 0.157 | 0.00 | 0.00 | 0.00 | 0.00 | 0.00 |
| 0.064 | 0.03 | 0.00 | 0.00 | 0.00 | 0.00 |
| 0.024 | 0.64 | 1.06 | 0.33 | 1.55 | 0.76 |
| 0.005 | 2.38 | 2.87 | 1.72 | 1.79 | 1.12 |
| | 3.05 | 3.93 | 2.05 | 3.34 | 1.88 |

TOTAL FRACTURE CONCENTRATION:
MEDIAN = 3.05%

$$\phi_c = \frac{(0.3)\pi}{4A} \sum_{n=1}^{N} a_n$$

(5.13)

$$\approx \frac{0.2356}{A} \sum_{n=1}^{N} a_n \, .$$

And equations (5.12) for $b_n$ = 0.3 cm become:

(5.14a) $$\phi_c(n) = \frac{0.2356}{A} a_n \; ; \text{ for } n = 1, 2, 3, \ldots, N$$

and

(5.14b) $$\alpha_n = \frac{b_n}{a_n} = \frac{0.3}{a_n} \, .$$

Calculating the aspect ratio and the volume of each measured fracture using equations (5.14) and grouping into populations by aspect ratio, also yields two dominant fracture populations with average aspect ratios of 0.024 and 0.005 (Figure 5.11). Concentrations range from 0.73 - 3.05 percent for aspect ratios averaging 0.024 and from 0.0 - 3.07 percent for ratios averaging 0.005 (Table 5.1b). With two additional fracture populations present in small quantities when fracture widths equal 0.3 cm, total fracture porosity ranges from 1.82 - 4.87 percent with a median value of 4.59 percent. Concentrations for fracture populations having aspect ratios of 0.064 and 0.137 range from 0 - 0.14 percent.

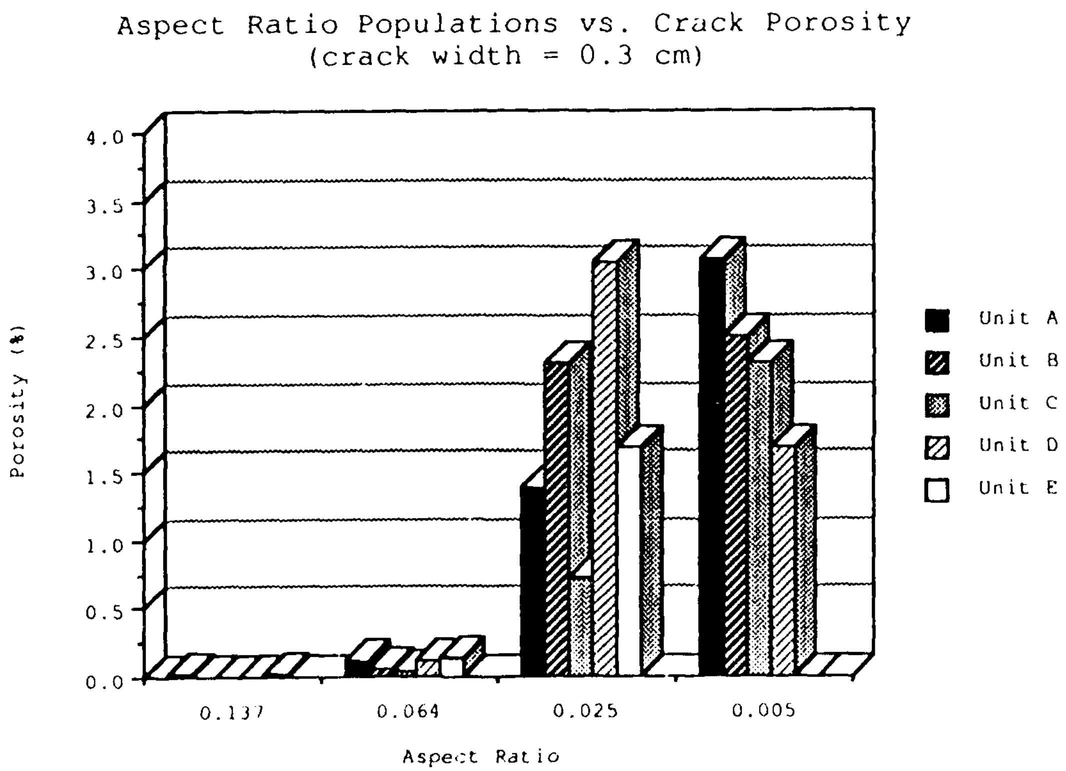


Figure 5.11 Concentration of crack populations having crack widths equal to 0.3 cm.

TABLE 5.1b

ASPECT RATIO VS. CONCENTRATION (fracture width = 0.3 cm)

| Aspect Ratio | Concentration (%) Unit A | Unit B | Unit C | Unit D | Unit E |
|---|---|---|---|---|---|
| 0.137 | 0.02 | 0.00 | 0.00 | 0.00 | 0.01 |
| 0.064 | 0.11 | 0.06 | 0.04 | 0.12 | 0.14 |
| 0.025 | 1.39 | 2.31 | 0.73 | 3.05 | 1.67 |
| 0.005 | 3.07 | 2.50 | 2.31 | 1.67 | 0.00 |
| | 4.59 | 4.87 | 3.08 | 4.84 | 1.82 |

TOTAL FRACTURE CONCENTRATION:
MEDIAN = 4.59%

The relatively large concentrations at the aspect ratio of 0.005 violate the imposed restriction on the theoretical model of Toksöz et al. (1976) that $c(\alpha_m)/\alpha_m < 1.0$. In all cases but one, c(0.005)/0.005 exceeds 1.0 (Table 5.2a-b). In addition, the Toksöz model only applies for low values of pore porosity (less than 10 percent) and dilute concentrations of fractures (fracture densities less than 0.1). Note that air-filled partings along horizontal bedding planes also contribute to fracture porosity. Because hand specimens extracted from the Santa Elena limestone average 15 - 20 cm in thickness, four to seven partings may occur in every meter with depth. Five horizontal fractures, 0.3 cm in thickness and slicing through a 1 $m^3$ volume, adds 1.2 percent to the total fracture porosities listed in Tables 5.1a-b. In Pepper's Mine, filled horizontal partings along bedding planes ranges from 7 - 30 cm in thickness whereas fillings in vertical fractures only range from 0 - 7 cm. These observations suggest that horizontal partings may be larger and contribute more to fracture porosity than do the vertical fractures observed at the surface. For the case where air-filled fracture porosity due to horizontal partings equals that due to vertical fractures, total fracture porosity ranges from 3.64 - 9.74 percent. Thus theoretical models used to predict total porosity and fracture density in terms of *in situ* velocities and matrix and whole rock parameters

TABLE 5.2a

ASPECT RATIO VS. $c(\alpha_n)/\alpha_n < 1$
(fracture width = 0.2 cm)

| $c(\alpha_n)/\alpha_n < 1$ | Unit A | Unit B | Unit C | Unit D | Unit E |
|---|---|---|---|---|---|
| c(0.157)/0.157 | 0.0000 | 0.0000 | 0.0000 | 0.0000 | 0.0000 |
| c(0.064)/0.064 | 0.0017 | 0.0000 | 0.0000 | 0.0000 | 0.0000 |
| c(0.024)/0.024 | 0.2780 | 0.4610 | 0.1430 | 0.6740 | 0.3300 |
| c(0.005)/0.005 | 3.9670 | 4.7830 | 2.8670 | 2.9830 | 1.8670 |

TABLE 5.2b

ASPECT RATIO VS. $c(\alpha_n)/\alpha_n < 1$
(fracture width = 0.3 cm)

| $c(\alpha_n)/\alpha_n < 1$ | Unit A | Unit B | Unit C | Unit D | Unit E |
|---|---|---|---|---|---|
| c(0.157)/0.157 | 0.0015 | 0.0000 | 0.0000 | 0.0000 | 0.0007 |
| c(0.064)/0.064 | 0.0172 | 0.0094 | 0.0063 | 0.0188 | 0.0219 |
| c(0.025)/0.025 | 0.5560 | 0.9240 | 0.2920 | 1.2200 | 0.6680 |
| c(0.005)/0.005 | 6.1400 | 5.0000 | 4.6200 | 3.3400 | 0.0000 |

must hold for large values of fracture porosity and pore porosity.

Surface Fracture Density Estimates. Fracture porosity ($\phi_c$) was estimated for unit surface areas A through E in the previous section. This section estimates the fracture density, $\varepsilon$, for each unit area.

For media containing ellipsoidal fractures of various aspect ratio, Budiansky and O'Connell (1976) relate the fracture density $\varepsilon$ to the number of fractures per unit volume $N_v$ and the major axis, a, and minor axis, b, of each fracture:

$$\varepsilon = \frac{2N_v}{\pi}\left\langle \frac{A^2}{P} \right\rangle , \tag{5.14a}$$

where

$$P = 4a\int_0^{\frac{\pi}{2}} \left[1 - \left(\frac{a^2-b^2}{a^2}\right)\sin^2\theta\right] d\theta \tag{5.14b}$$

and

$$A = \pi ab \tag{5.14c}$$

equal a fracture perimeter and area respectively. In the case of circular fractures (i.e., penny shaped fractures), equation (5.14a) simplifies to

(5.14d) $$\varepsilon = N_v \left\langle a^3 \right\rangle .$$

Lynn and Thomsen (1986) go further and set equation (5.14d) equal to equation (5.41), the fracture density/fracture porosity relationship used in the Biot-Consistent theoretical model for circular fractures

(5.15) $$\varepsilon = \frac{3}{4\pi}\frac{\phi_c}{\lambda} = N_v \left\langle a^3 \right\rangle ;$$

where $\langle a^3 \rangle$ is the mean cube of the fracture lengths (or traces) exposed at the surface. This expression relates more closely to fracture permeability rather than fracture porosity (Long, 1983).

Both equations (5.14d) and (5.15) assume implicitly that all fractures within a given unit volume must be the same size. For this to be true, as fracture length increases, fracture width increases proportionately such that the aspect ratio $\lambda$ ($= \alpha = b/a$) remains constant. Because more than one fracture population exists in the Santa Elena limestone, the relationship, $\varepsilon = N_v \langle a^3 \rangle$, is not appropriate for estimating surface fracture density at the site. The existence of more than one fracture population requires that the aspect ratio be taken into consideration when estimating the surface fracture density.

Using expression (5.41), the total fracture porosity $\phi_c$ and the mean aspect ratio within a given unit volume, $\bar{\lambda}$, can be related to an average value of fracture density $\langle\varepsilon\rangle$:

$$\langle\varepsilon\rangle = \frac{3}{4\pi}\frac{\phi_c}{\bar{\lambda}}, \tag{5.16a}$$

where for every population "n"

$$\bar{\lambda} = \frac{\lambda_1 + \lambda_2 + \ldots + \lambda_n}{N}; \quad \text{for } n = 1, 2, \ldots, N. \tag{5.16b}$$

Using the aspect ratios and the total fracture porosities determined for units A through E in the previous section, equation (5.16b) yields a mean aspect ratio of 0.063 for vertical fractures with 0.2 cm openings. The average fracture density ranges from 0.07 to 0.15 with a median value of 0.11 (Table 5.3). Similarly, for vertical fractures with 0.3 cm openings, the mean aspect ratio equals 0.058; and the average fracture density ranges from 0.07 to 0.20 with a median value of 0.19. Consideration of horizontal parting raises the median density values to 0.23 and 0.38, assuming fracture porosity due to horizontal parting equals that due to vertical fracturing in the region of study. Because horizontal parting appears extensive along cliff walls, its contribution to fracture porosity may even be higher. The fracture density estimates for the vertical fractures act as a lower bound.

TABLE 5.3

AVERAGE FRACTURE DENSITY ESTIMATES FOR UNITS A - E

| | Average Fracture Density <ε> | |
|---|---|---|
| Unit | Fracture Width = 0.2 cm<br>Mean Aspect Ratio = 0.063 | Fracture Width = 0.3 cm<br>Mean Aspect Ratio = 0.058 |
| A | 0.11 | 0.19 |
| B | 0.15 | 0.20 |
| C | 0.08 | 0.13 |
| D | 0.13 | 0.20 |
| E | 0.07 | 0.07 |

Most sedimentary rocks have fracture densities greater than 0.1; and rocks of interest to the petroleum industry commonly have fracture densities of 0.3 or more (Thomsen, 1985). Hence, the estimated values for fracture density at the surface seem reasonable.

Inspection of fracture distribution suggests that the ENE trending fractures have more prominence than the NNW trending. For unit areas A through E, the mean fracture lengths range from 12.01 - 33.58 cm; and the minimum and maximum exposed fracture traces equal 1.27 ± 0.05 cm and 111.76 ± 0.05 cm (Table 5.4). The mean fracture lengths for ENE trending fracture sets exceed NNW trending sets by approximately 10 - 25 percent in units B, C, and E, 50 percent in unit A, and equal one another in unit D. In number, the NNW and ENE fracture sets equal 130 and 124 respectively. The average separation distance between NNW fractures is approximately 6.65 cm; for ENE fractures the separation distance averages 6.15 cm. Although the NNW and ENE fracture sets approximately equal one another in number and in average separation distance, the relatively short NNW fractures give the ENE set more prominence. In addition, the infrared photo reveals more pronounced east trending macrofractures (Figure 2.3). These observations give the *in situ* velocity measurements more credibility.

## TABLE 5.4

## SPATIAL DISTRIBUTION AND SIZE OF FRACTURES

| Unit | Orientation | Surface Area and *Estimate of Dimensions NNWxENE | Mean Crack Length <a> (cm) | Average Separation Distance d (cm) | Maximum Crack Length $a_{max}$ (cm) |
|---|---|---|---|---|---|
| | NNW | 152.40 cm | 16.16 | 5.75 | 111.76 |
| A | ENE | 92.71 cm | 31.50 | 3.12 | 93.98 |
| | (NNW+ENE) | 13548.36 $cm^2$ | 23.96 | 4.44 | - |
| | NNW | 40.64 cm | 20.85 | 4.86 | 53.34 |
| B | ENE | 55.88 cm | 23.50 | 6.99 | 33.02 |
| | (NNW+ENE) | 2270.96 $cm^2$ | 21.33 | 5.93 | - |
| | NNW | 77.47 cm | 27.53 | 9.41 | 81.28 |
| C | ENE | 76.20 cm | 33.58 | 11.94 | 68.58 |
| | (NNW+ENE) | 5903.21 $cm^2$ | 29.63 | 10.68 | - |
| | NNW | 74.93 cm | 18.50 | 6.24 | 54.61 |
| D | ENE | 52.07 cm | 18.06 | 5.80 | 71.12 |
| | (NNW+ENE) | 3860.00 $cm^2$ | 18.27 | 6.02 | - |
| | NNW | 55.88 cm | 12.01 | 6.99 | 48.26 |
| E | ENE | 110.00 cm | 16.34 | 2.94 | 48.26 |
| | (NNW+ENE) | 6350.79 $cm^2$ | 14.90 | 4.97 | - |

*Unit surface areas in most cases have trapezoidal or L-shaped geometry.

## Model Parameters--Solid Grain and Biot Medium

The moderate to high fracture porosity and fracture density estimates for both the horizontal and vertical fractures, and the 2.5 - 14 percent range in pore porosity measured in the laboratory, suggest that application of the Biot-Consistent model is most appropriate in analyzing the relationship between fracture density and porosity and *in situ* P- and S-wave velocities. Utilizing the Biot-Consistent model to obtain predictions of fracture porosity and fracture density along seismic ray paths requires solid grain and Biot medium parameters as well as pore porosity and *in situ* P- and S-wave velocity measurements.

When matrix velocities equal the P- and S-wave intercept velocities of 6.04 km/s and 3.23 km/s in Figures 4.5 and 4.6, and grain density equals that of pure calcite; equations (5.4m) and (5.4n) yield a solid grain shear and solid grain bulk modulus of $2.838 \times 10^{13}$ kg/(km)s$^2$ and $6.139 \times 10^{13}$ kg/(km)s$^2$ respectively (Table 5.5).

Table 5.6 lists the Biot medium parameters calculated for various values of pore porosity using equations (5.4c) through (5.4j). All Biot medium parameters (the composite P- and S-wave velocities, shear and bulk moduli, pore and fracture parameters, etc.) decrease as pore porosity increases.

In the next section, application of the Biot-Consistent model predicts fracture porosity and density using 1) the solid grain parameters $\mu_s$ and $K_s$, 2) the Biot medium parameters, $A_B^*$, $B_B^*$, $a_B^*$, and $b_B^*$, calculated from the mean and

TABLE 5.5

SOLID GRAIN PARAMETER VALUES

Solid Grains:

$VP_s$ = compressional velocity of the solid grains

= compressional intercept velocity (Figure 4.5)

= 6.04 km/s

$VS_s$ = shear velocity of the solid grains

= shear intercept velocity (Figure 4.6)

= 3.23 km/s

$\rho_s$ = density for pure calcite

= $2.72 \times 10^{12}$ kg/km$^3$

$\mu_s$ = $2.838 \times 10^{13}$ kg/(km)s$^2$

$K_s$ = $6.139 \times 10^{13}$ kg/(km)s$^2$

TABLE 5.6

BIOT MEDIUM PARAMETER VALUES ($\rho_f$=0)

| | Pore Porosity | | | |
|---|---|---|---|---|
| | $\phi_p$ = 0.052 (median) | $\phi_p$ = 0.060 (mean) | $\phi_p$ = 0.11 | $\phi_p$ = 0.14 |
| Compressinal wave velocity $VP_B$* | †5.84 km/s | ††5.62 km/s | 5.30 km/s | 4.94 km/s |
| Shear wave velocity $VS_B$* | †3.12 km/s | ††2.99 km/s | 2.96 km/s | 2.81 km/s |
| Dry Bulk Density $\rho_B$* | †2.567 E12 kg/km$^3$ | ††2.533 E12 kg/km$^3$ | 2.421 E12 kg/km$^3$ | 2.337 E12 kg/km$^3$ |
| Shear Modulus $\mu_B$* | †2.499 E13 kg/(km)s$^2$ | ††2.265 E13 kg/(km)s$^2$ | 2.121 E13 kg/(km)s$^2$ | 1.845 E13 kg/(km)s$^2$ |
| Bulk Modulus $K_B$* | †5.423 E13 kg/(km)s$^2$ | ††4.980 E13 kg/(km)s$^2$ | 3.973 E13 kg/(km)s$^2$ | 3.243 E13 kg/(km)s$^2$ |
| Poison's Ratio $\nu$* | 0.300 | 0.303 | 0.273 | 0.261 |

| | | | | |
|---|---|---|---|---|
| Fracture Parameters: | | | | |
| $A_B$* | 4.044 | 4.098 | 3.624 | 3.466 |
| $B_B$* | 1.376 | 1.372 | 1.415 | 1.432 |
| Pore Parameters: | | | | |
| $a_B$* | 0.619 | 0.623 | 0.584 | 0.569 |
| $b_B$* | 0.476 | 0.475 | 0.483 | 0.486 |

† Values associated with the median pore porosity ($\phi_p$=0.052)

†† Mean laboratory measurements

median laboratory measurements of pore porosity and P- and S-wave velocities, and 3) the *in situ* P- and S-wave velocity measurements VP* and VS*.

## Model Application and Interpretation

Applying the Biot-Consistent model for the drained case with the *in situ* velocity measurements and solid grain and Biot medium parameters (discussed in the previous section) yields a range in average fracture porosity of 10 to 15 percent when pore porosity equals 6 percent, the mean of the laboratory porosity measurements (Table 5.7). For the median 5.2 percent pore porosity measurement, the fracture porosity range is slightly higher. Fracture density ranges from 0.30 to 0.48. These values come well within the range of fracture density estimates made from the surface fracture measurements of length and width when horizontal fracturing, in addition to vertical fracturing, is taken into consideration. Using the predicted values of average fracture porosity and density in equation (5.16a) predicts a range in average aspect ratio of 0.06 - 0.07 along spreads 4 through 6, and 0.10 - 0.11 along spreads 1 through 3. In comparison, the average aspect ratios used to estimate fracture density from surface fracture measurements equal 0.058 and 0.060 (Table 5.3).

In the radial array (spreads 2 through 6) the Biot-Consistent model predicts higher fracture densities along the north trending lines, indicating that the ENE fracture set is more prominent. Along north trending spread 1, measurement

TABLE 5.7

CALCULATED FRACTURE POROSITY, ASPECT RATIO, AND DENSITY
VERSUS
*IN SITU* P- AND S-WAVE VELOCITY MEASUREMENTS

| | SPREAD 1<br>VP* = 3.02 km/s<br>VS* = 2.39 km/s | SPREAD 2<br>VP* = 2.53 km/s<br>VS* =2.25 km/s | SPREAD 3<br>VP* = 3.35 km/s<br>VS* = 2.46 km/s | SPREAD 4<br>VP* = 2.99 km/s<br>VS* = 1.91 km/s | SPREAD 5<br>VP* = 3.13 km/s<br>VS* =1.91 km/s | SPREAD 6<br>VP* = 2.82 km/s<br>VS* = 1.73 km/s |
|---|---|---|---|---|---|---|
| FOR $\phi_P$=0.052 | | | | | | |
| $\phi$ | 0.20 | 0.22 | 0.19 | 0.18 | 0.16 | 0.18 |
| $\phi_C$ | 0.15 | 0.17 | 0.14 | 0.13 | 0.11 | 0.13 |
| $\langle\varepsilon\rangle$ | 0.34 | 0.38 | 0.31 | 0.45 | 0.44 | 0.48 |
| $\langle\lambda\rangle$ | 0.10 | 0.11 | 0.11 | 0.07 | 0.06 | 0.65 |
| FOR $\phi_P$=0.060 | | | | | | |
| $\phi$ | 0.19 | 0.21 | 0.18 | 0.17 | 0.16 | 0.17 |
| $\phi_C$ | 0.13 | 0.15 | 0.12 | 0.11 | 0.10 | 0.11 |
| $\langle\varepsilon\rangle$ | 0.32 | 0.36 | 0.30 | 0.43 | 0.43 | 0.47 |
| $\langle\lambda\rangle$ | 0.10 | 0.10 | 0.10 | 0.06 | 0.06 | 0.06 |

of P- and S-wave velocities at a greater depth explains, in comparison to the north trending radial spreads, the lower fracture density prediction.

Thus the Biot-Consistent model for the drained case and the data collected in this study can explain the difference between the bulk rock and *in situ* velocities at the Lajitas site.

## VI. Summary and Conclusions

A breached fractured antiform, caused by a lacolithic intrusion sometime during the Tertiary, exposes the Santa Elena limestone of Cretaceous age. Two orthogonal air-filled fracture sets existing in the Santa Elena strike NNW and ENE with subvertical to vertical inclinations. Primarily calcite with secondary clay and silica in concentrations less than 3 percent and 6 percent respectively, the Santa Elena rock matrix is homogeneous compositionally. In comparison to P- and S-wave velocities for pure calcite ($V_p$ = 6.53 km/s, $V_s$ = 3.36 km/s), a variation in pore porosity ranging from 2.5 percent to 14 percent, with void space spherical in geometry, lowers compressional wave velocities 10 to 25 percent and for shear wave velocities 5 to 15 percent. The P- and S-wave velocities for the solid grains, determined from intercept velocities, equal 6.04 km/s and 3.23 km/s respectively. *In situ* velocity ranges from 2.53 km/s to 3.35 km/s for compressional waves, and from 1.59 km/s to 2.28 km/s for shear waves.

The Biot-Consistent model for the drained state accurately predicts fracture porosity and average fracture density with the *in situ* velocity measurements and solid grain and Biot medium parameters determined from the laboratory measurements for the Santa Elena limestone. Average fracture densities range from 0.30 to 0.48; whereas crack porosity varies from 10 to 17 percent.

Several observations suggest the presence of slight azimuthal anisotropy: 1) the faster *in situ* Sv-wave velocity measurements of 2.70 ± 0.5 km/s and 2.28 km/s ± 0.5 km/s along easterly paths (as opposed to the Sh-wave velocity measurements of 2.21 ± 0.4 km/s and 2.22 ± 0.4 km/s), 2) greater fracture density predictions along north trending seismic ray paths, 3) longer more pronounced ENE fracture sets, as observed from the infrared photo and measured in unit surface areas A through E, and 4) the personal communication from Golden that incoming teleseismic P- and Sv-waves from the east travel at faster velocities than those coming from the north.

Determining the presence of azimuthal anisotropy at the Lajitas site with certainty requires a refraction survey designed to measure *in situ* P- and S- wave velocities with less than 2 percent error. Using an explosive source to produce narrower pulse widths, and placing receivers at two meter intervals along full spread lengths (oriented at several azimuths) to provide maximum horizontal coverage, produces *in situ* P- and S- wave velocity measurements with enough accuracy to determine the presence of azimuthal anisotropy with certainty.

In conclusion, 1) three sets of open air-filled fractures exist in the Santa Elena limestone: horizontal partings along bedding planes, and vertical NNW and ENE trending fracture sets, and 2) these open air-filled fractures lower the expected wave velocities at the Lajitas Texas site.

# APPENDIX A

## SCALE RELATIONSHIPS AND ORIENTATION BETWEEN MAPS

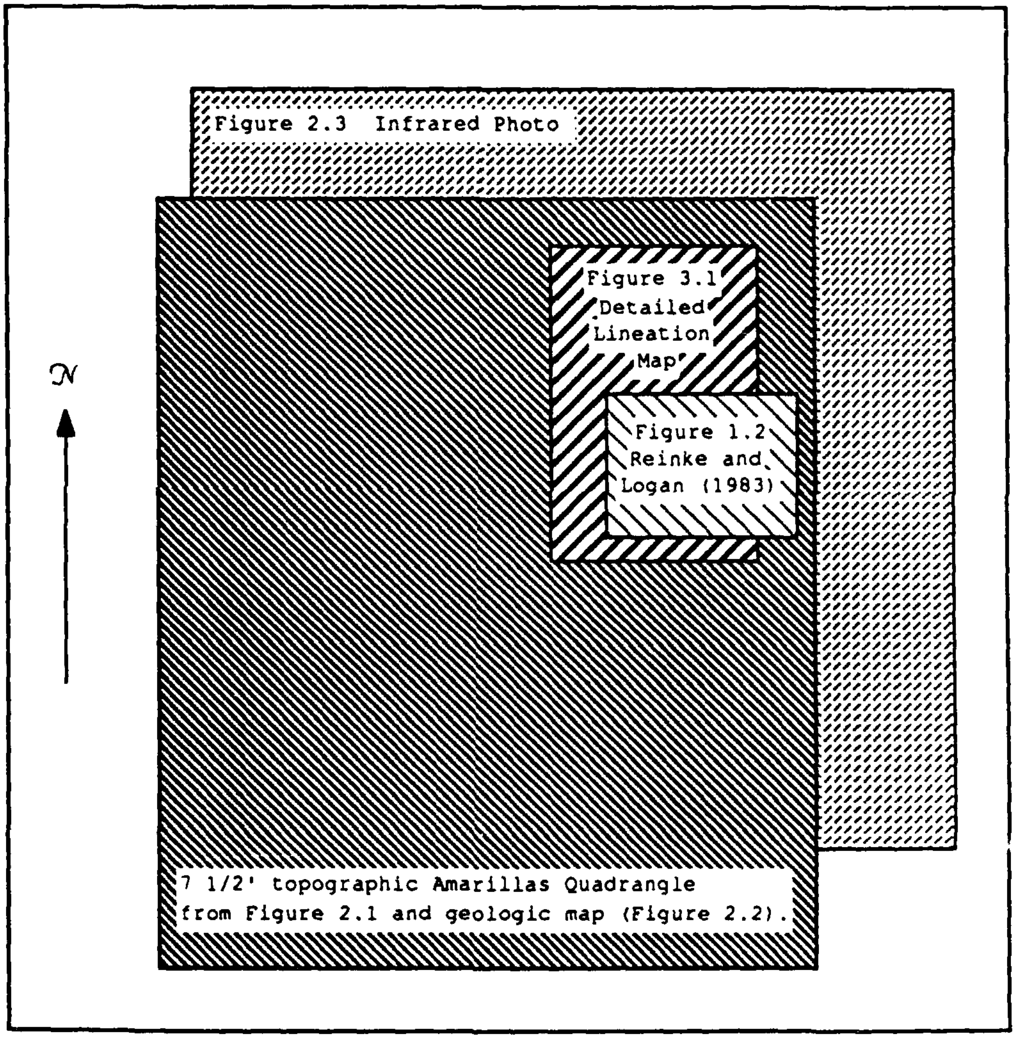


Scale relationship between Figures 1.2, 2.2, 2.3, and 3.1.

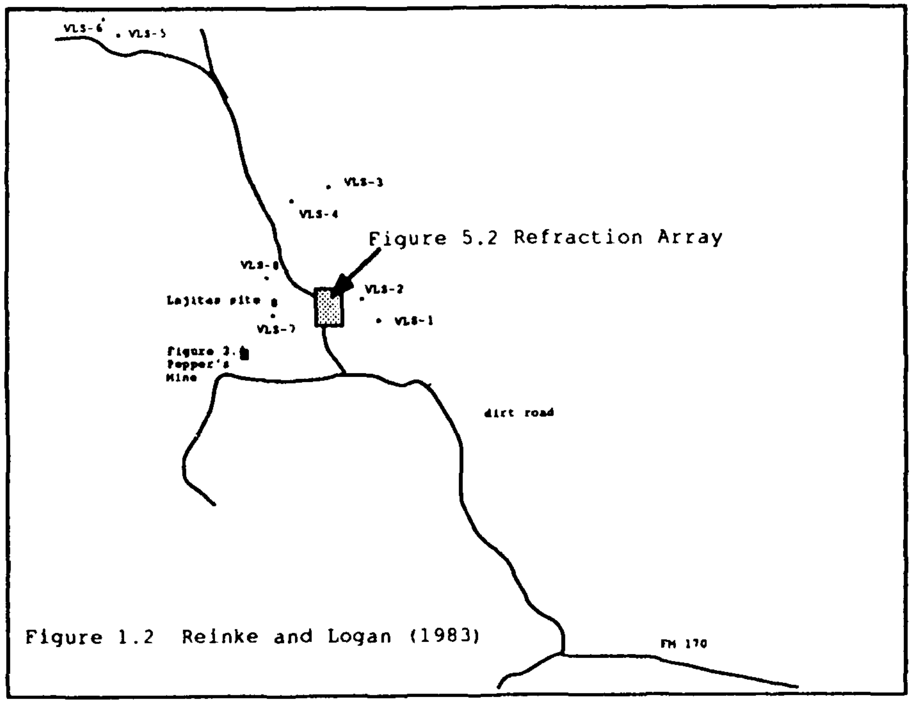


Scale relationship between Figure 1.2, 3.4, 5.2 and location from which the eight oriented hand specimens (VLS-1, VLS-2, ..., VLS-8) were extracted.

# APPENDIX B

# EXPERIMENTAL SEISMOGRAMS FOR SANTA ELENA LIMESTONE

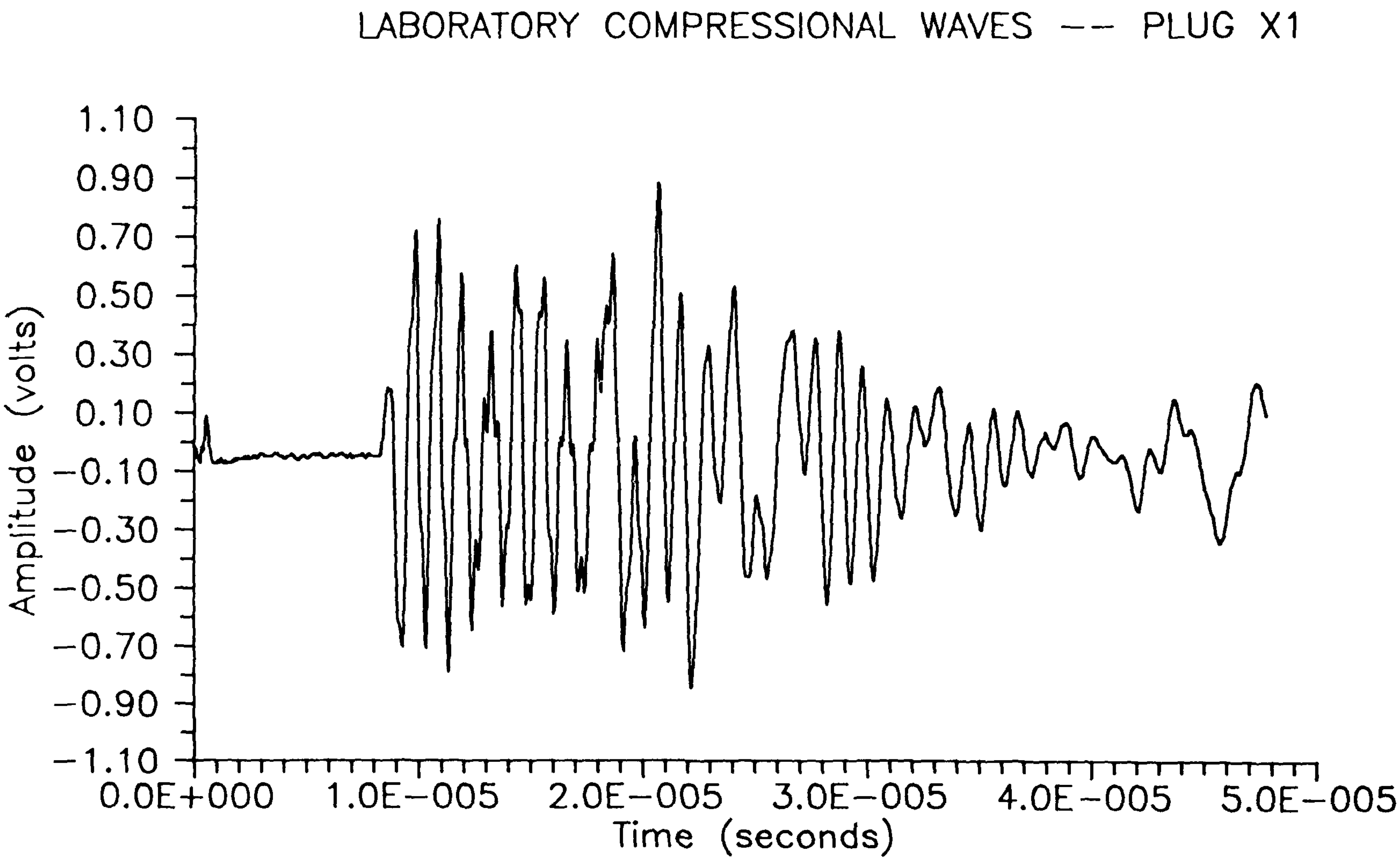


P-wave displacements polarized perpendicular to horizontal bedding planes.

LABORATORY SHEAR WAVES -- PLUG X1

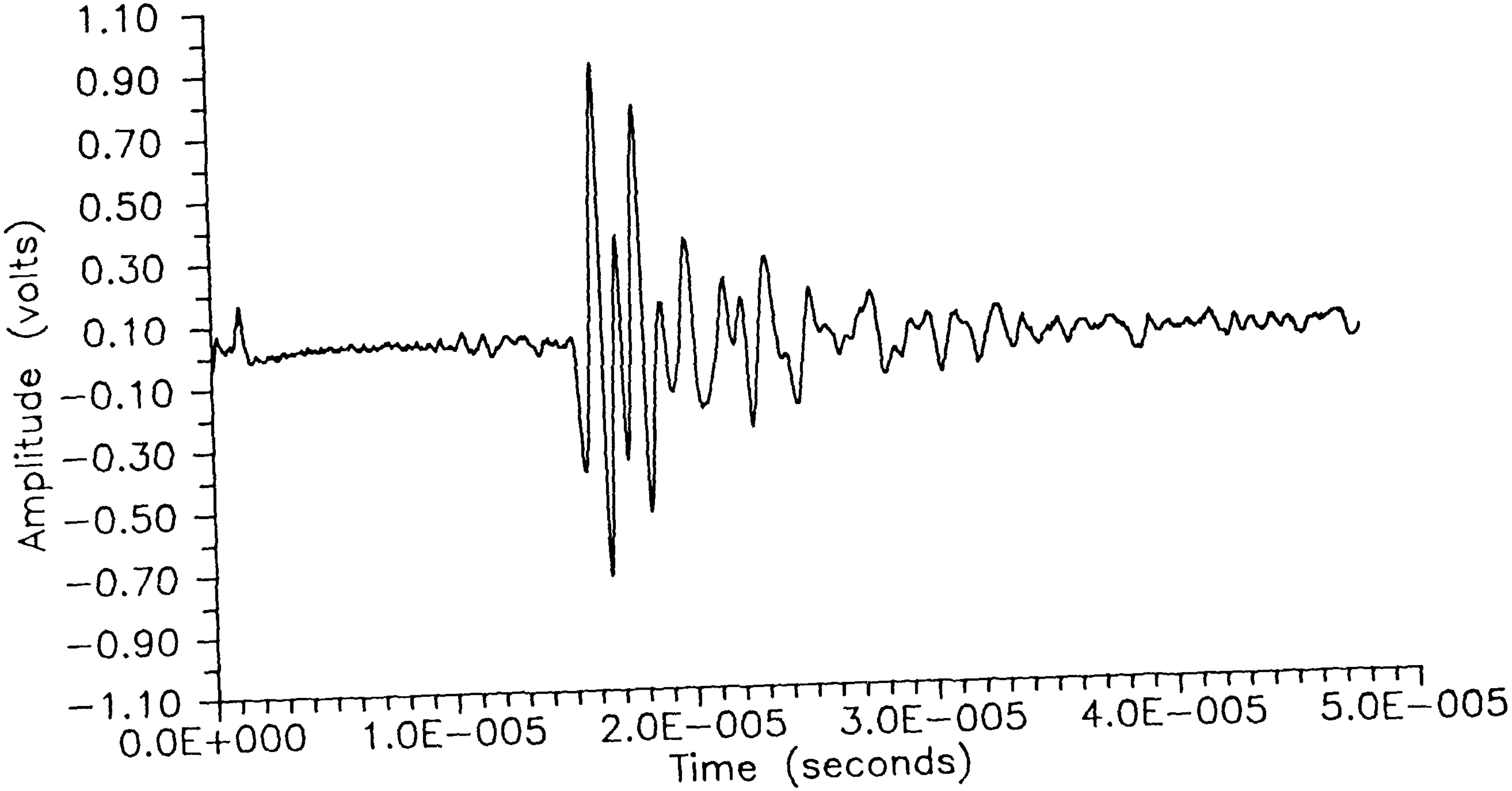


Shear wave displacements polarized horizontal and in plane of NNW fracture set.

LABORATORY SHEAR WAVES -- PLUG X1

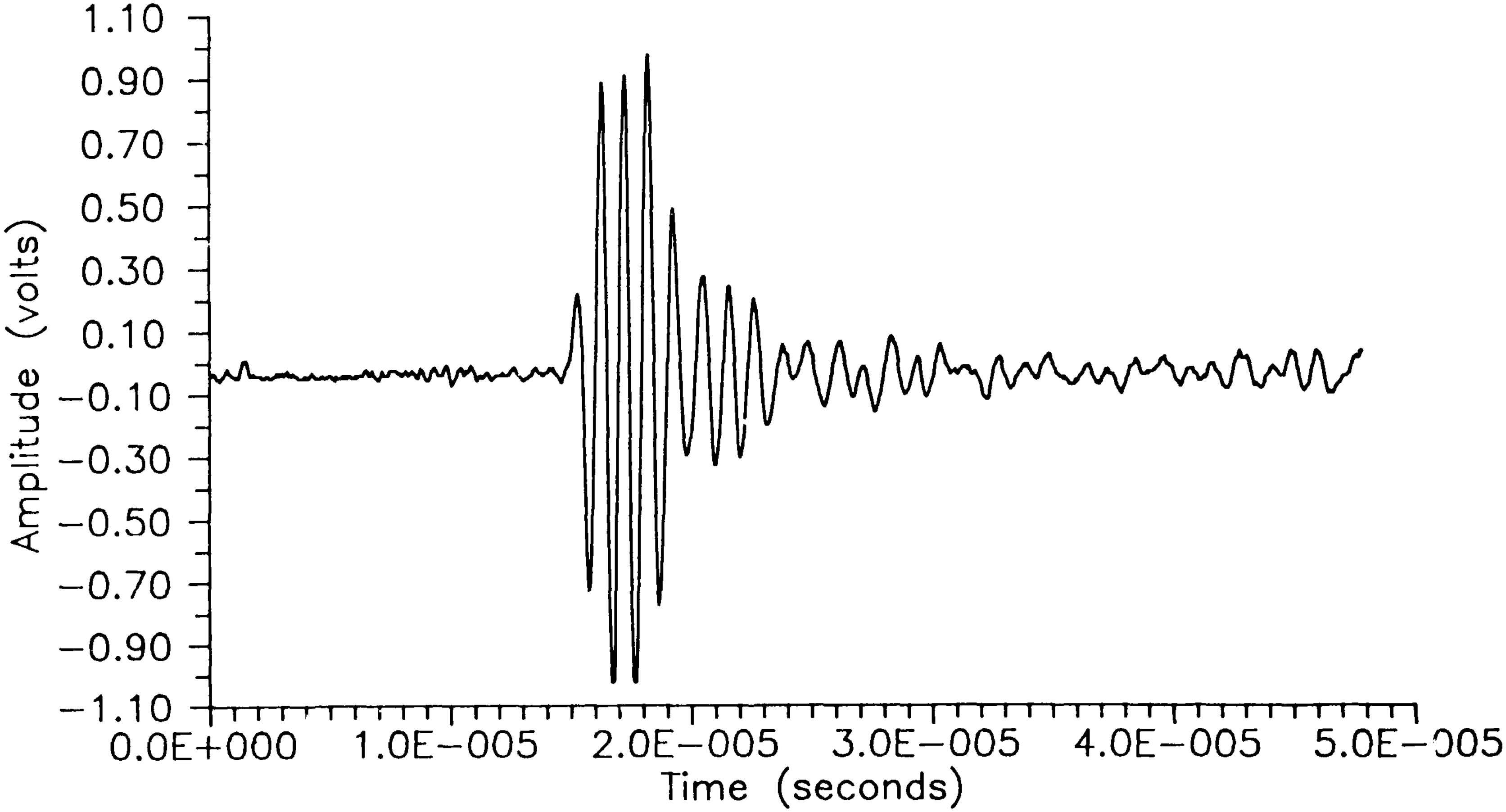


Shear wave displacements polarized horizontal and in plane of ENE fracture set.

LABORATORY COMPRESSIONAL WAVES -- PLUG Y1B

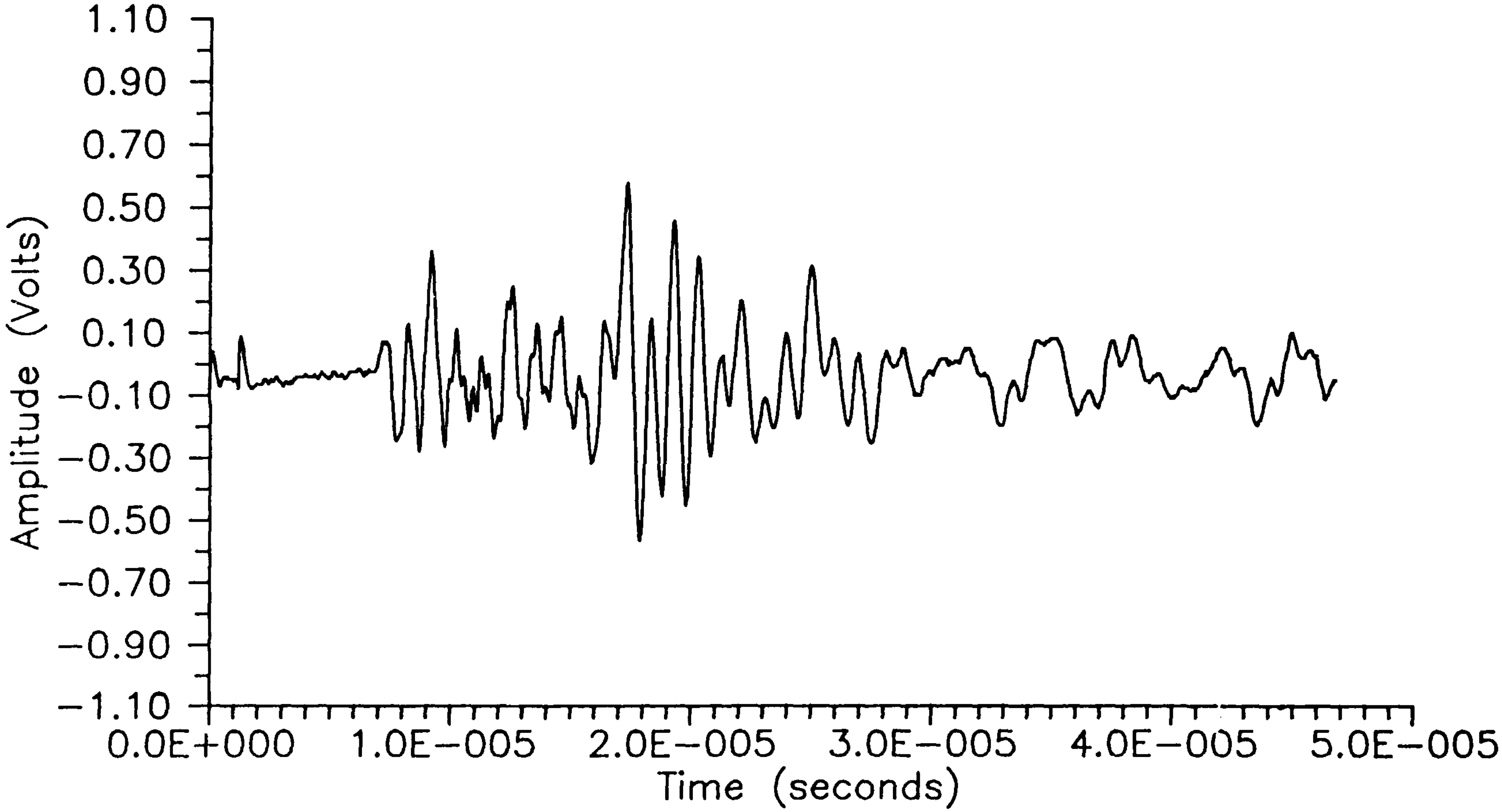


P—wave displacements polarized horizontal and in plane of ENE fracture set.

# LABORATORY SHEAR WAVES -- PLUG Y1B

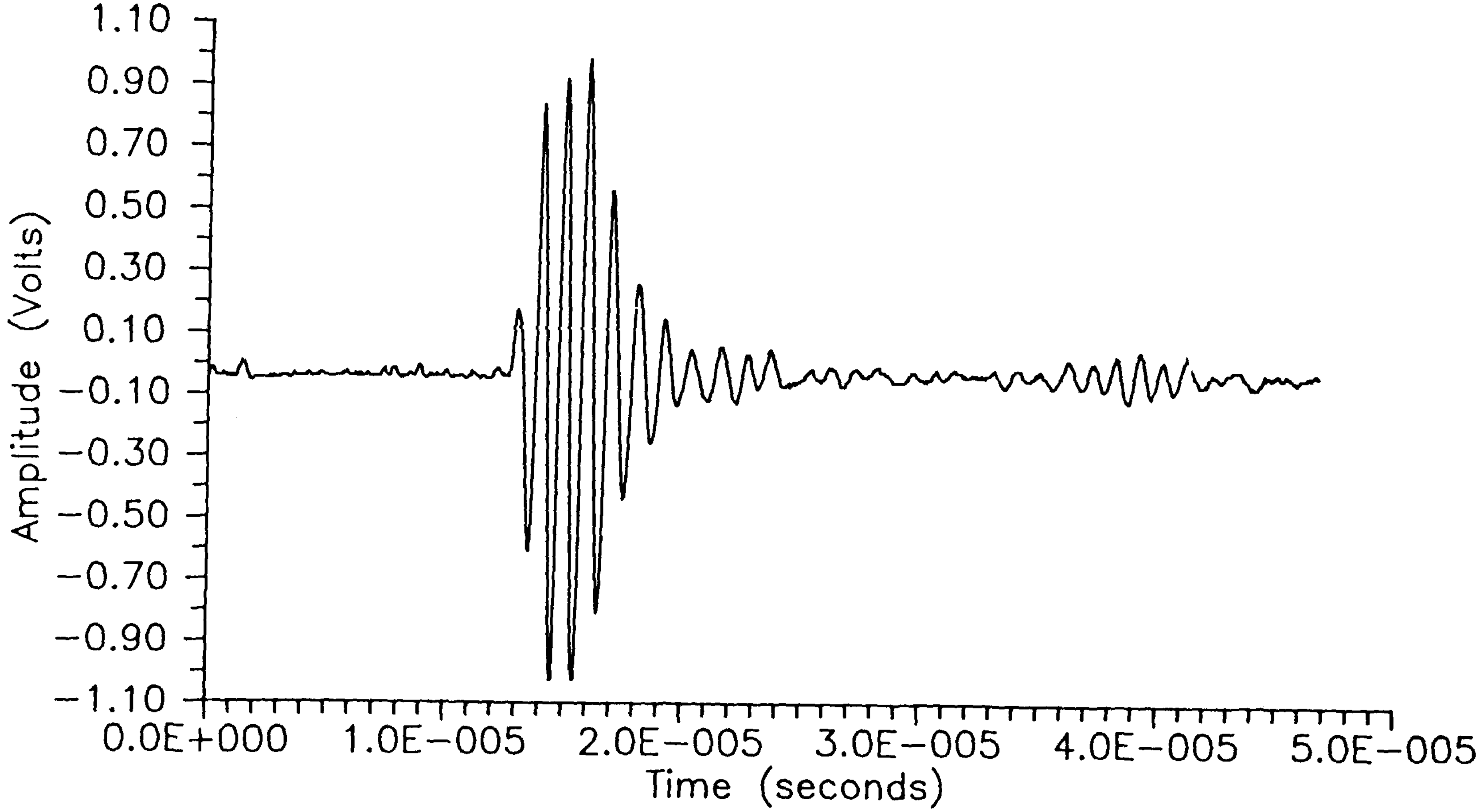


*Shear wave displacements polarized vertical and in plane of ENE fracture set.*

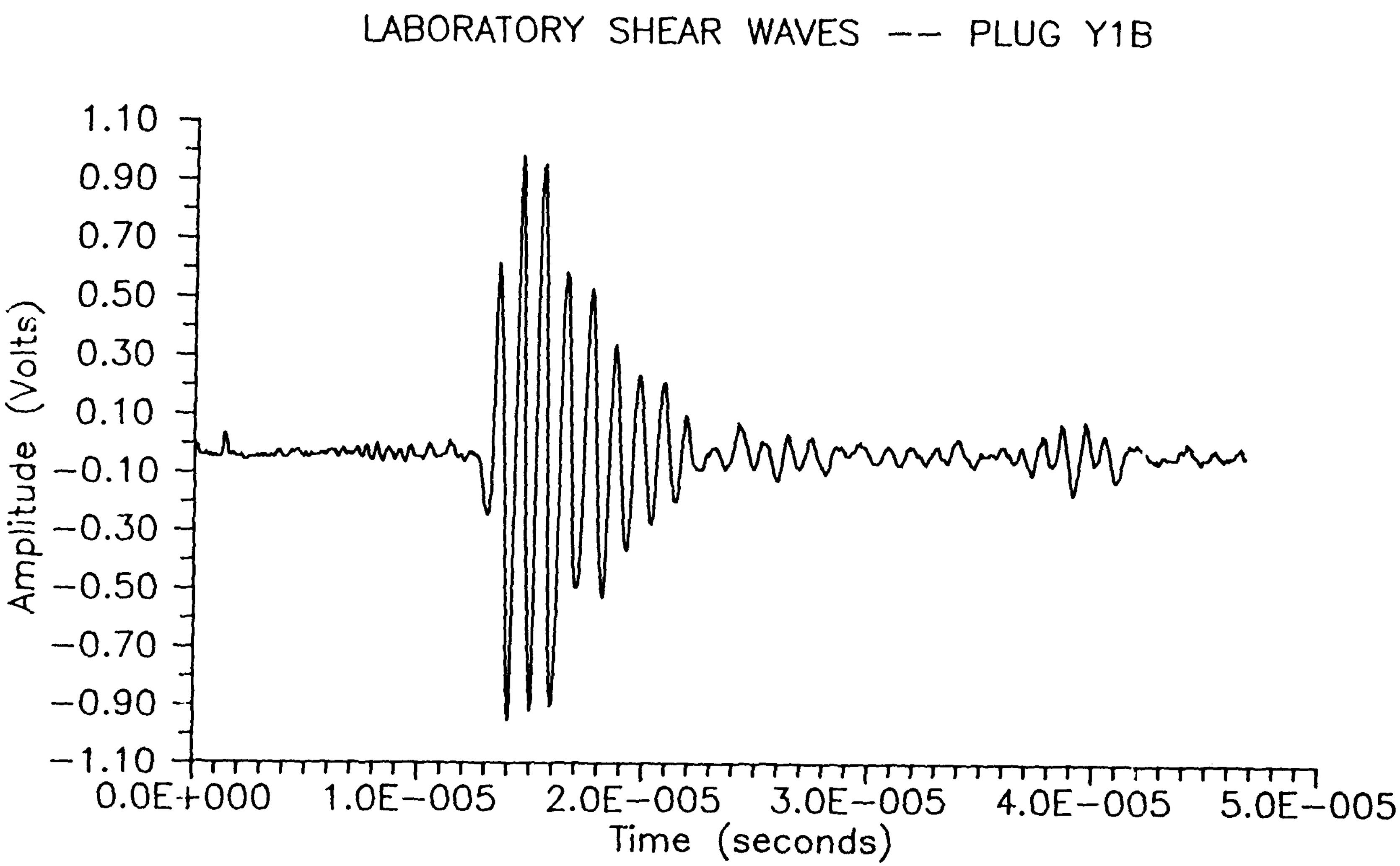

Shear wave displacements polarized perpendicular to ENE fracture planes.

LABORATORY COMPRESSIONAL WAVES -- PLUG Z1B

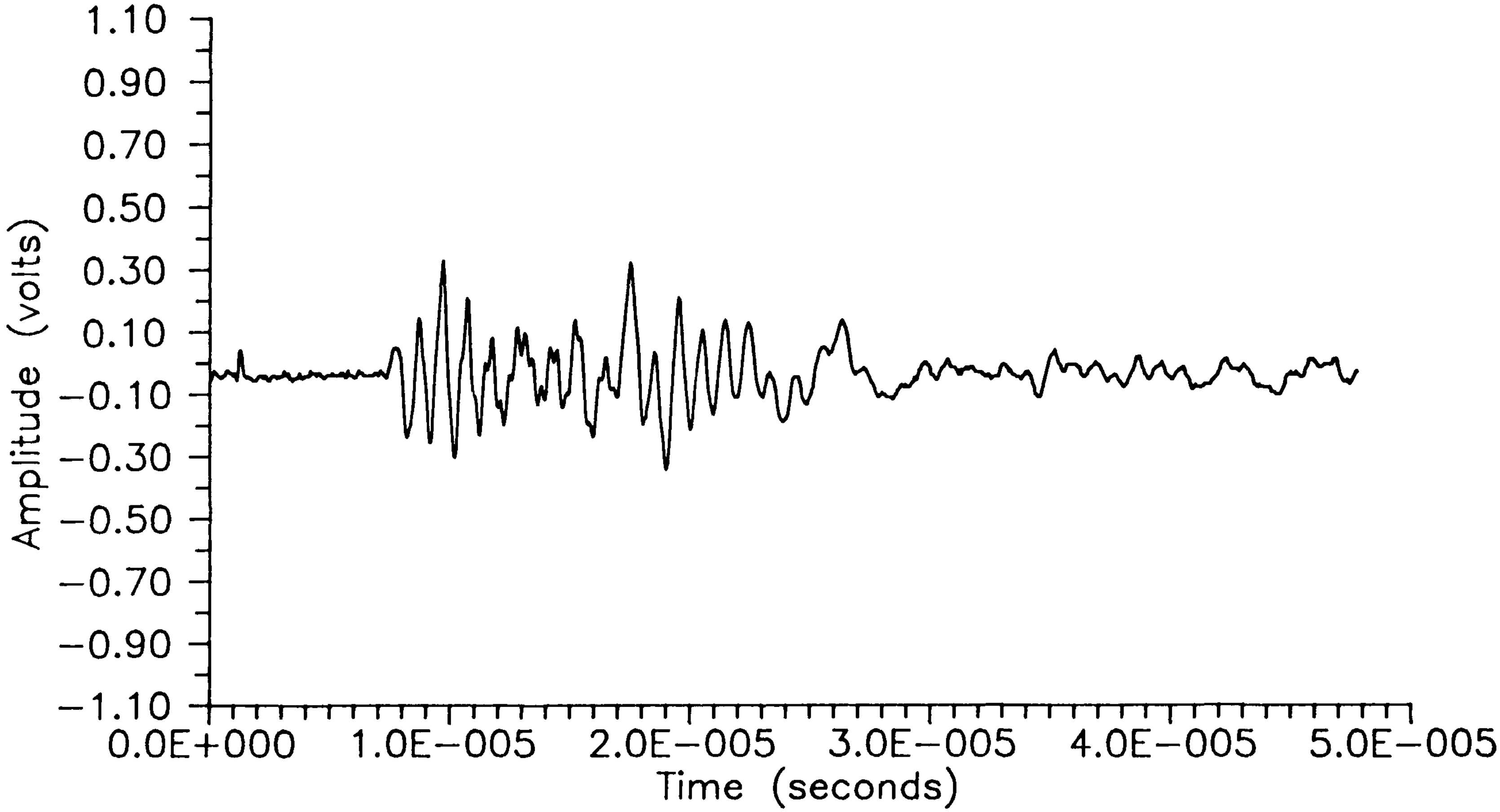


P—wave displacements polarized horizontal and in plane of NNW fracture set.

LABORATORY SHEAR WAVES -- PLUG Z1B

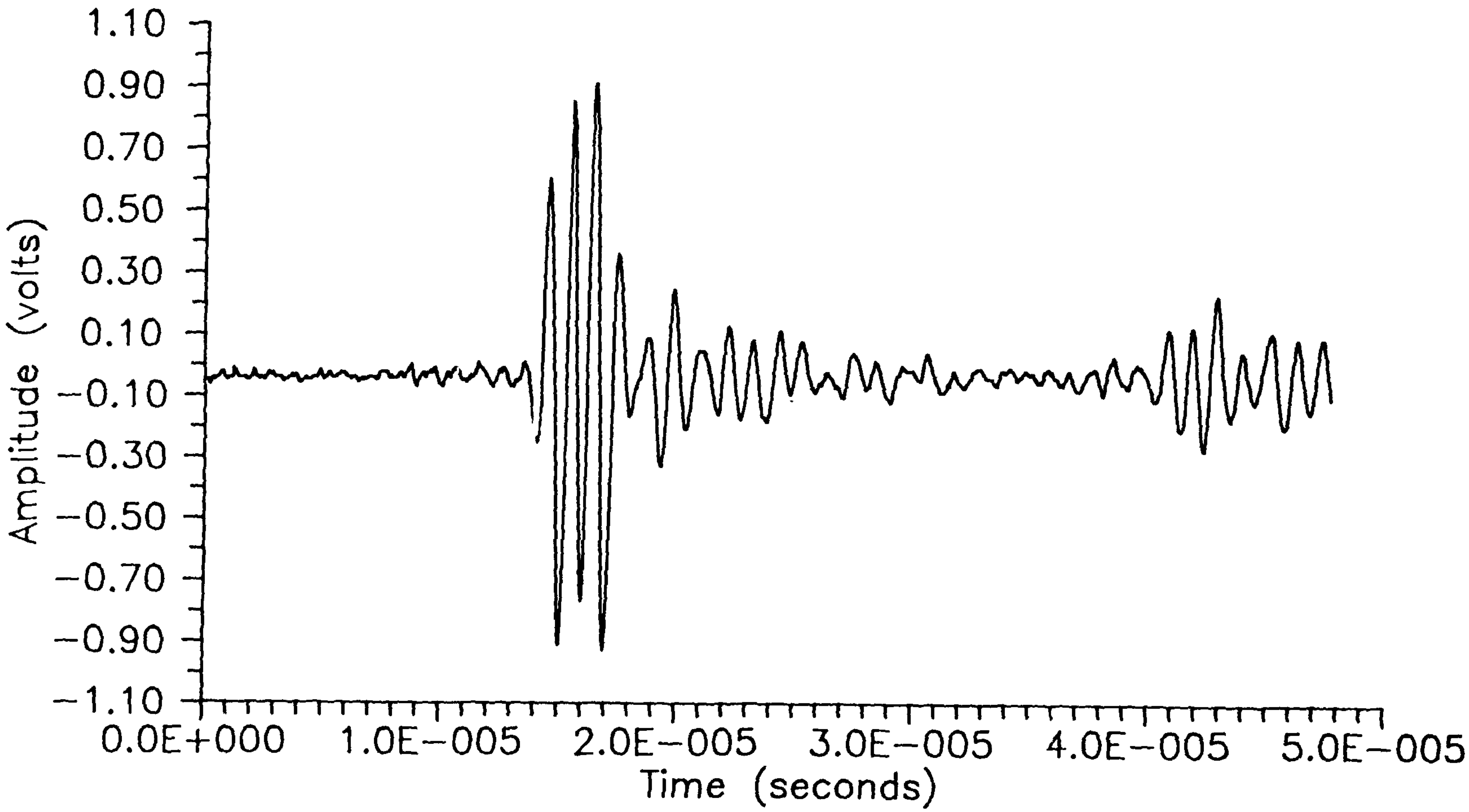


Shear wave displacements polarized vertical and in plane of NNW fracture set.

LABORATORY SHEAR WAVES -- PLUG Z1B

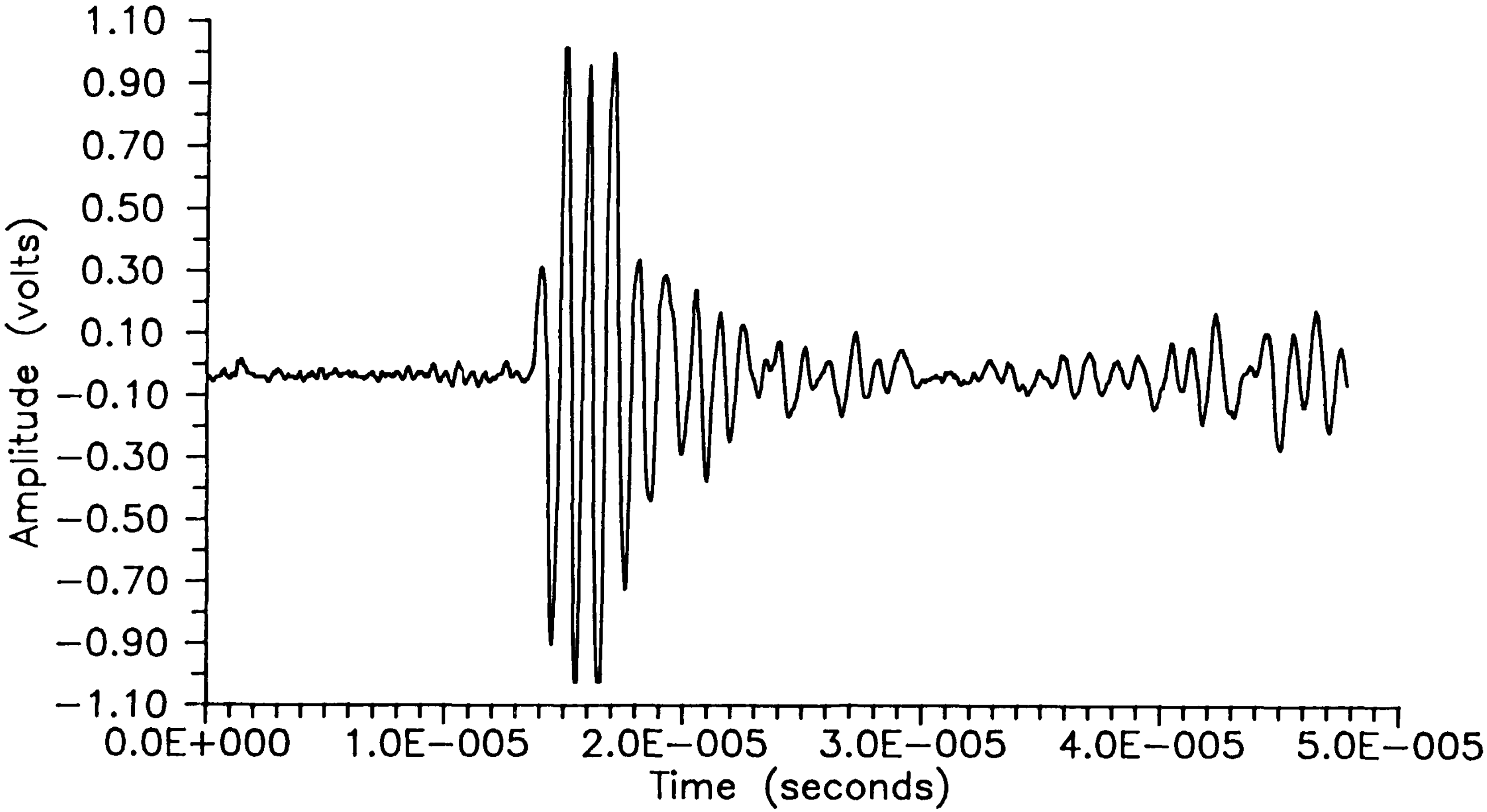


Shear wave displacements polarized horizontal and perpendicular to NNW fracture set.

# APPENDIX C

## SCALARS $T_{iijj}$ AND $T_{ijij}$

Defined below are the scalars $T_{iijj}$ and $T_{ijij}$ used by Toksoz et al. (1976):

$$T_{iijj} = \frac{3F_1}{F_2}$$

$$T_{ijij} - \frac{1}{3} T_{iijj} = \frac{2}{F_3} + \frac{1}{F_4} + \frac{F_4F_5 + F_6F_7 - F_8F_9}{F_2 F_4} ,$$

where

$$F_1 = 1 + A \left[\frac{3}{2}(g + \phi) - R\left(\frac{3}{2}g + \frac{5}{2}\phi - \frac{4}{3}\right)\right] ,$$

$$F_2 = 1 + A \left[1 + \frac{3}{2}(g + \phi) - \frac{R}{2}(3g + 5\phi)\right]$$

$$+ B(3 - 4R) + \frac{A}{2}(A + 3B)(3 - 4R)$$

$$\circ \left[g + \phi - R\left(g - \phi + 2\phi^2\right)\right] ,$$

$$F_3 = 1 + \frac{A}{2}\left[R(2 - \phi) + \frac{\left(1 + \alpha^2\right)}{\alpha^2} g(R - 1)\right] ,$$

$$F_4 = 1 + \frac{A}{4}\left[3\phi + g + - R(g - \phi)\right] ,$$

$$F_5 = A \left[R\left(g + \phi - \frac{4}{3}\right) - g\right] + B\phi(3 - 4R) ,$$

$$F_6 = 1 + A \left[1 + g - R(g + \phi)\right] + B(1 - \phi)(3 - 4R) ,$$

$$F_7 = 2 + \frac{A}{4}\left[9\phi + 3g - R\left(5\phi + 3g\right)\right] + B\phi(3 - 4R) ,$$

$$F_8 = A\left[1 - 2R + \frac{g}{2}(R - 1) + \frac{\phi}{2}(5R - 3)\right] + B\left(1 - \phi\right)(3 - 4R) ,$$

$$F_9 = A\left[g(R - 1) - R\phi\right] + B\phi(3 - 4R) ,$$

$$A = \frac{\mu'}{\mu} - 1 ,$$

$$B = \frac{1}{3}\left(\frac{K'}{K} - \frac{\mu'}{\mu}\right) ,$$

$$R = \frac{3\mu}{3K + 4\mu} ,$$

$$\phi = \frac{\alpha}{\left(1 - \alpha^2\right)^{\frac{3}{2}}}\left[\cos^{-1}\alpha - \alpha\left(1 - \alpha^2\right)^{\frac{1}{2}}\right],$$

$$g = \frac{\alpha^2}{\left(1 - \alpha^2\right)}(3\phi - 2) .$$

## APPENDIX D

## FIELD SEISMOGRAMS FOR SANTA ELENA LIMESTONE

P-WAVE SEISMIC RECORD FOR LINE 1 -- FORWARD PROFILE

2 meter source offset from nearest geophone

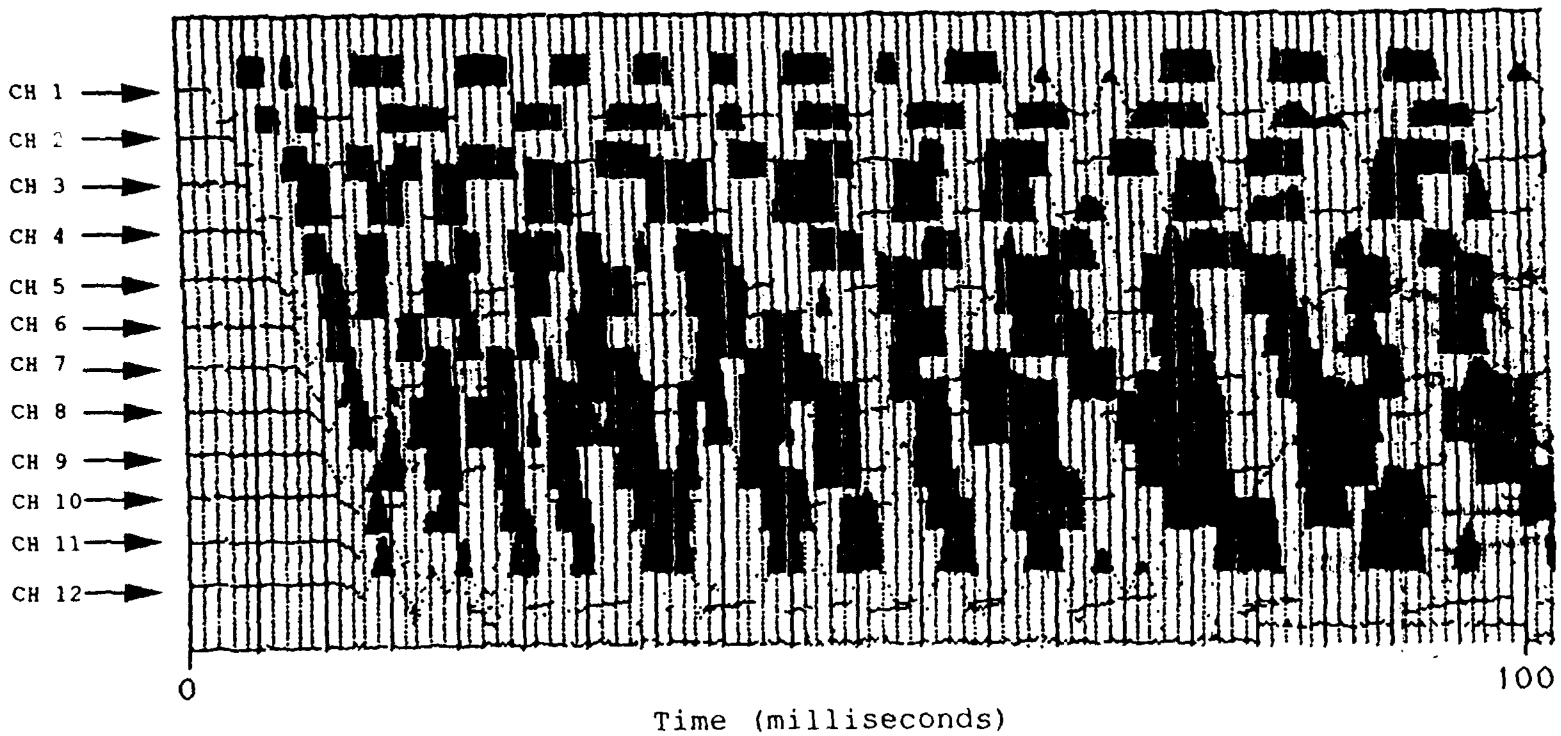

P-WAVE SEISMIC RECORD FOR LINE 1 -- FORWARD PROFILE

22 meter source offset from nearest geophone

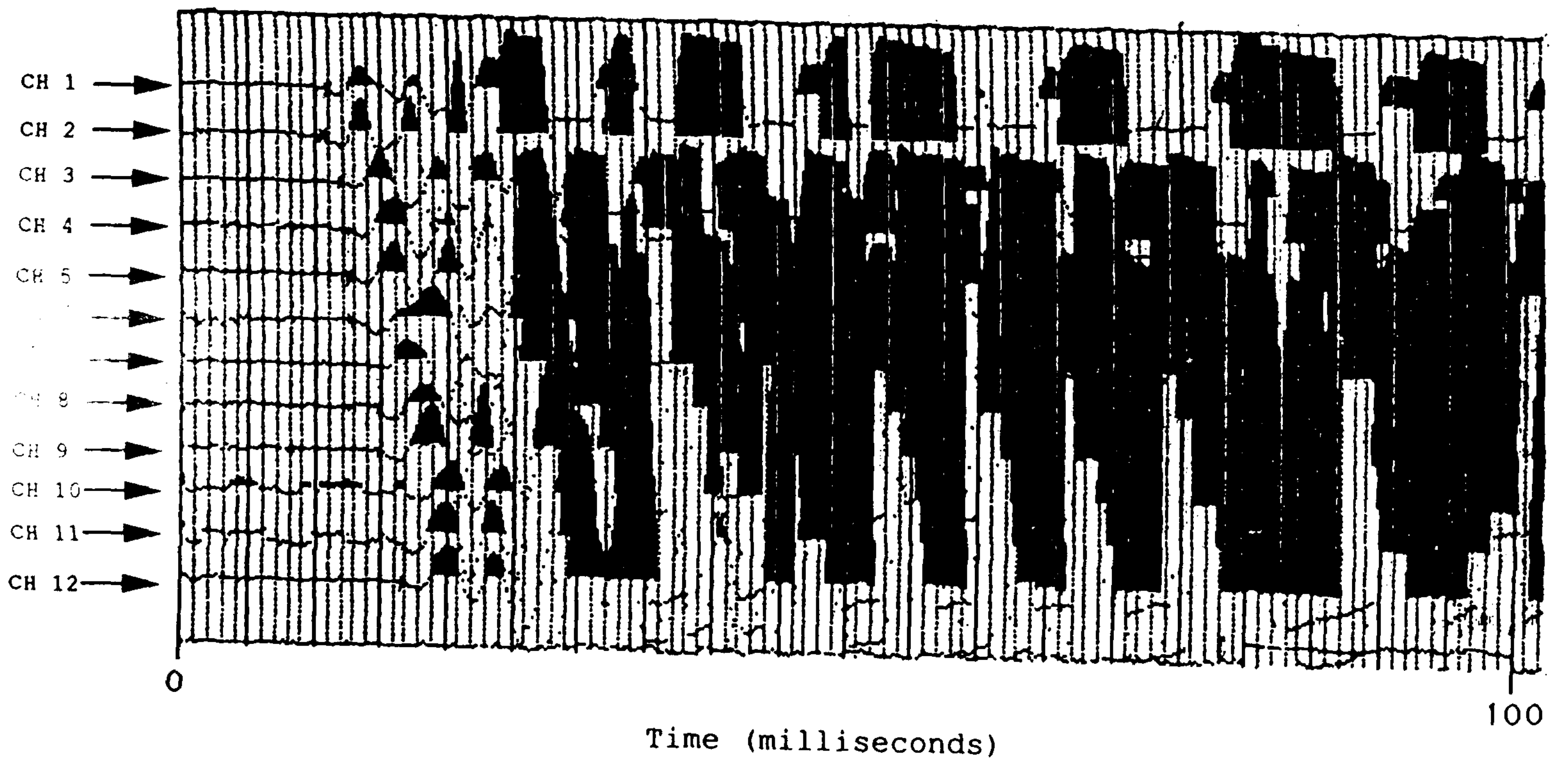

P-WAVE SEISMIC RECORD FOR LINE 1 -- REVERSE PROFILE

22 meter source offset from nearest geophone

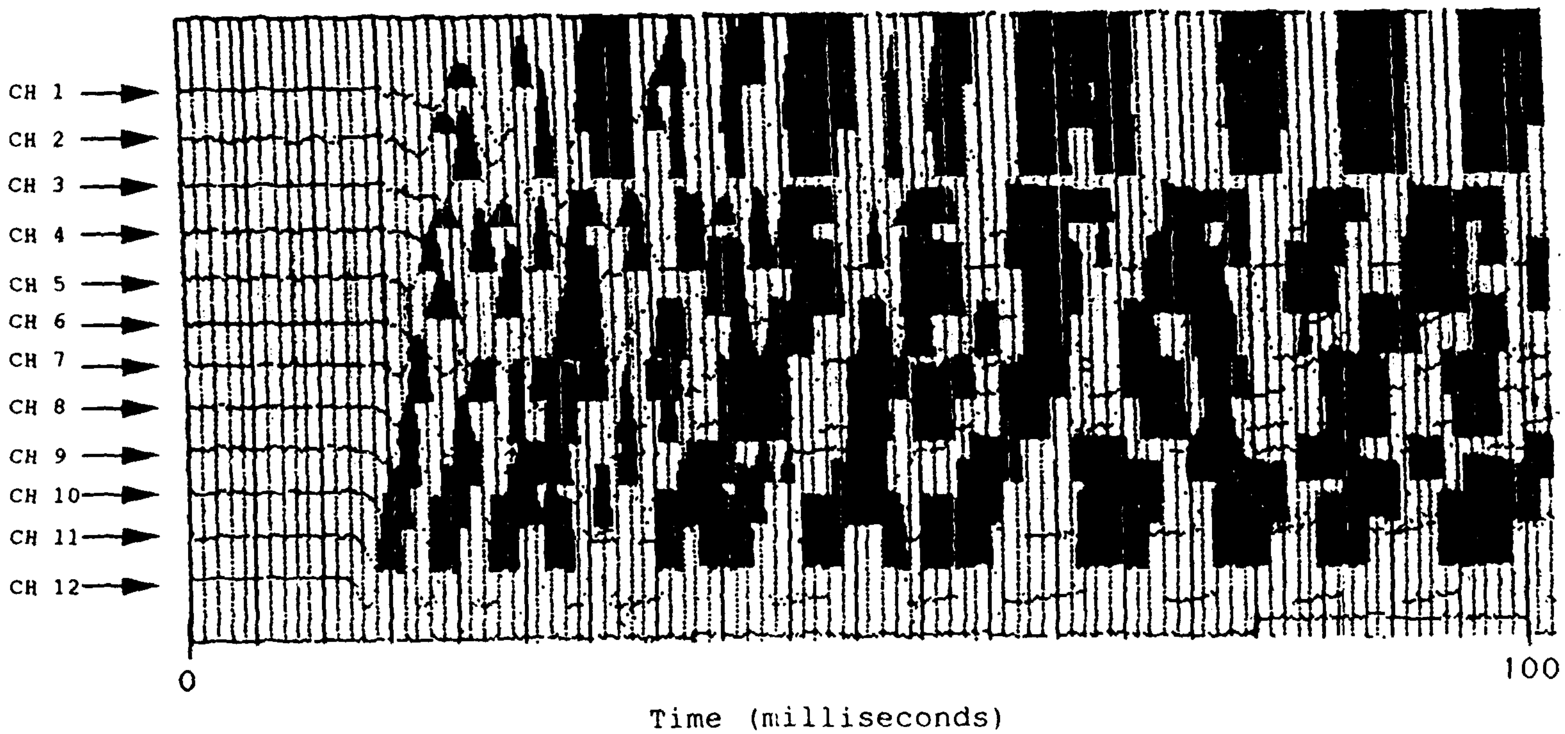

P-WAVE SEISMIC RECORD FOR LINE 1 -- REVERSE PROFILE

2 meter source offset from nearest geophone

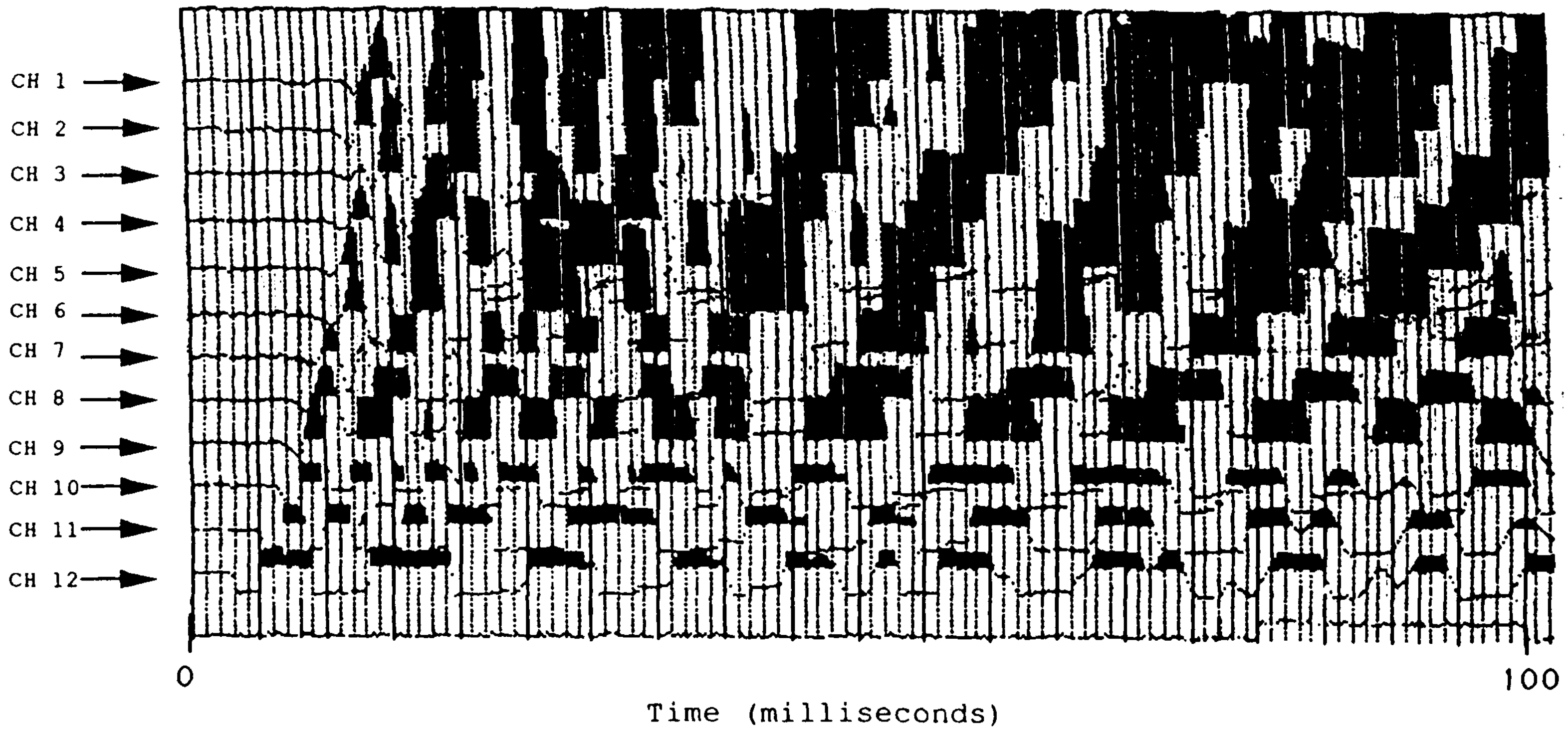

SV-WAVE SEISMIC RECORD FOR LINE 1 -- FORWARD PROFILE

2 meter source offset from nearest geophone

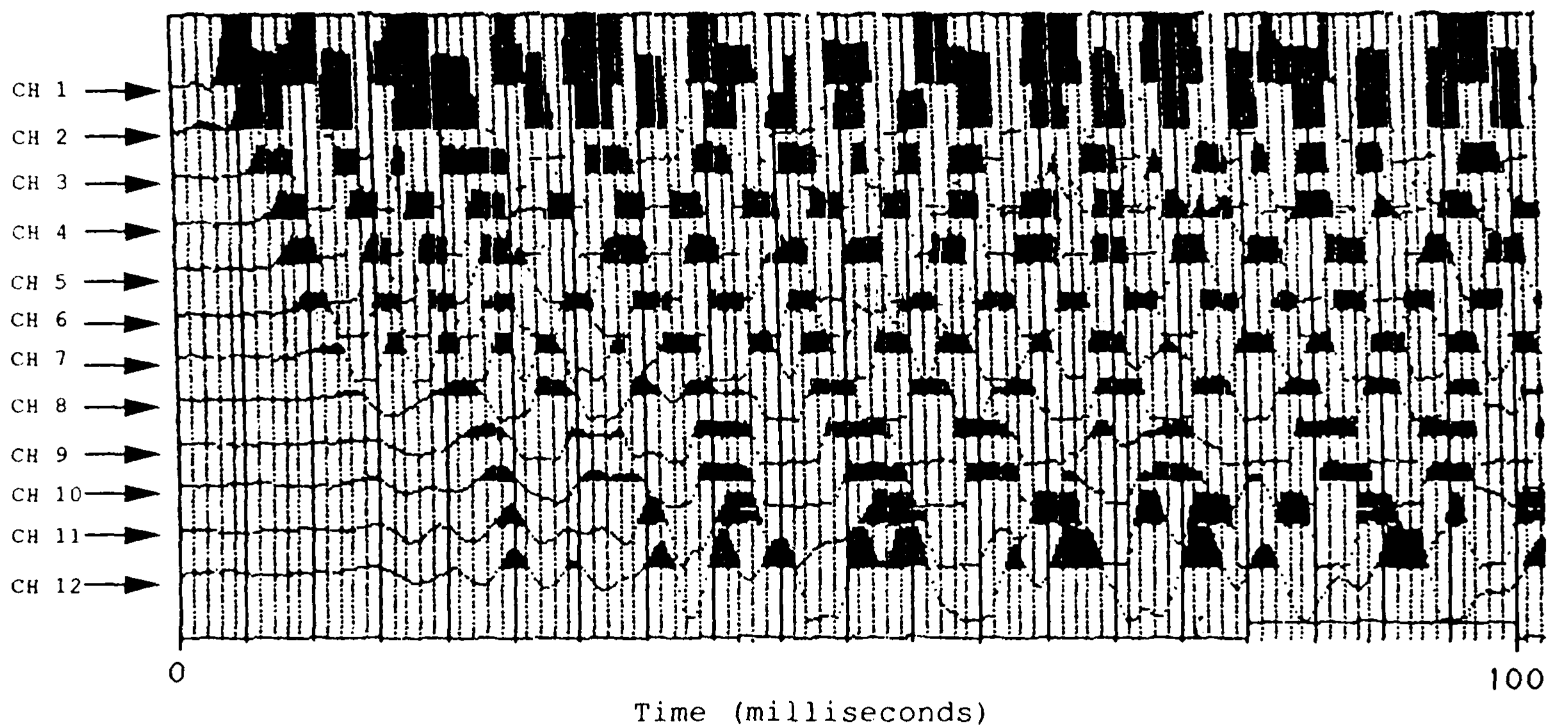

SV-WAVE SEISMIC RECORD FOR LINE 1 -- FORWARD PROFILE

22 meter source offset from nearest geophone

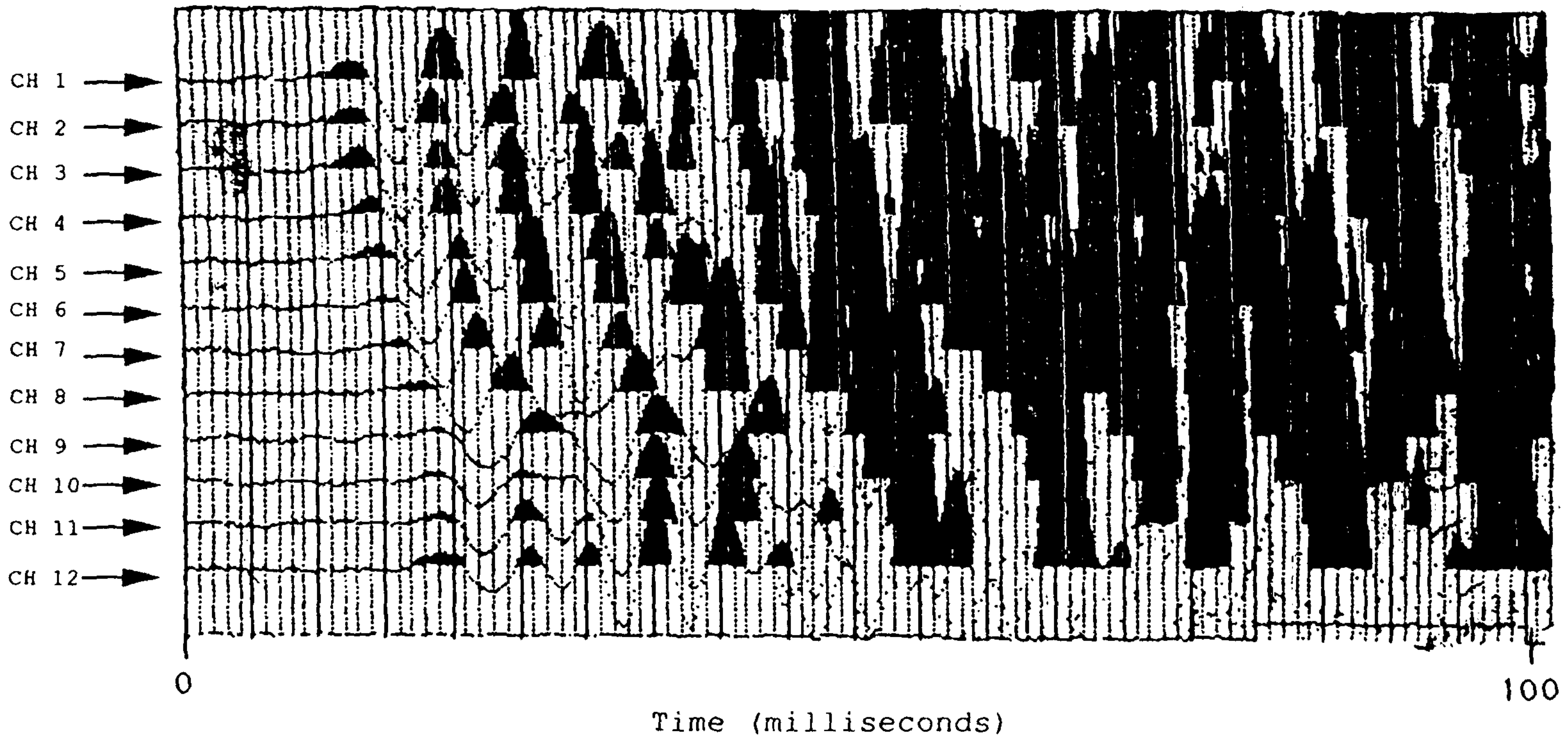

SV-WAVE SEISMIC RECORD FOR LINE 1 -- REVERSE PROFILE

2 meter source offset from nearest geophone

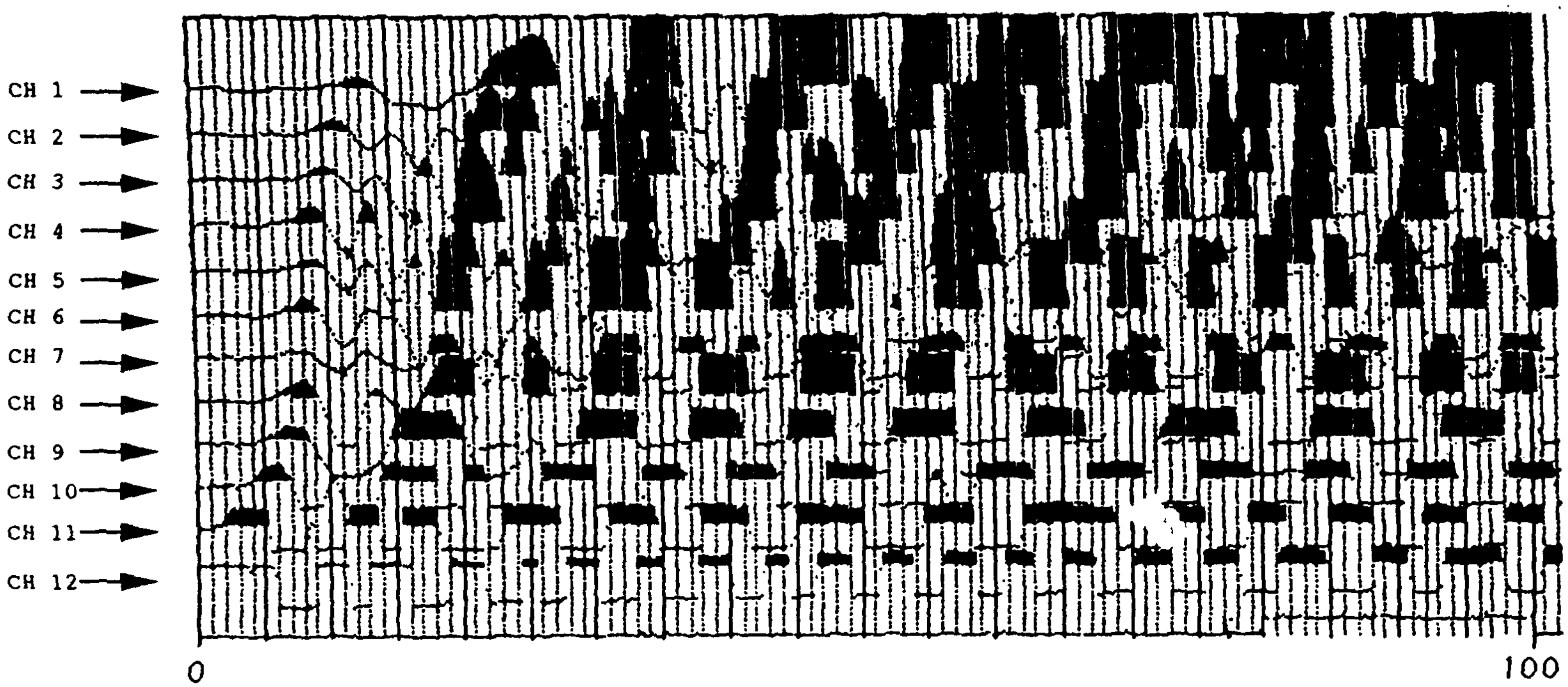

SV-WAVE SEISMIC RECORD FOR LINE 1 -- REVERSE PROFILE

22 meter source offset from nearest geophone

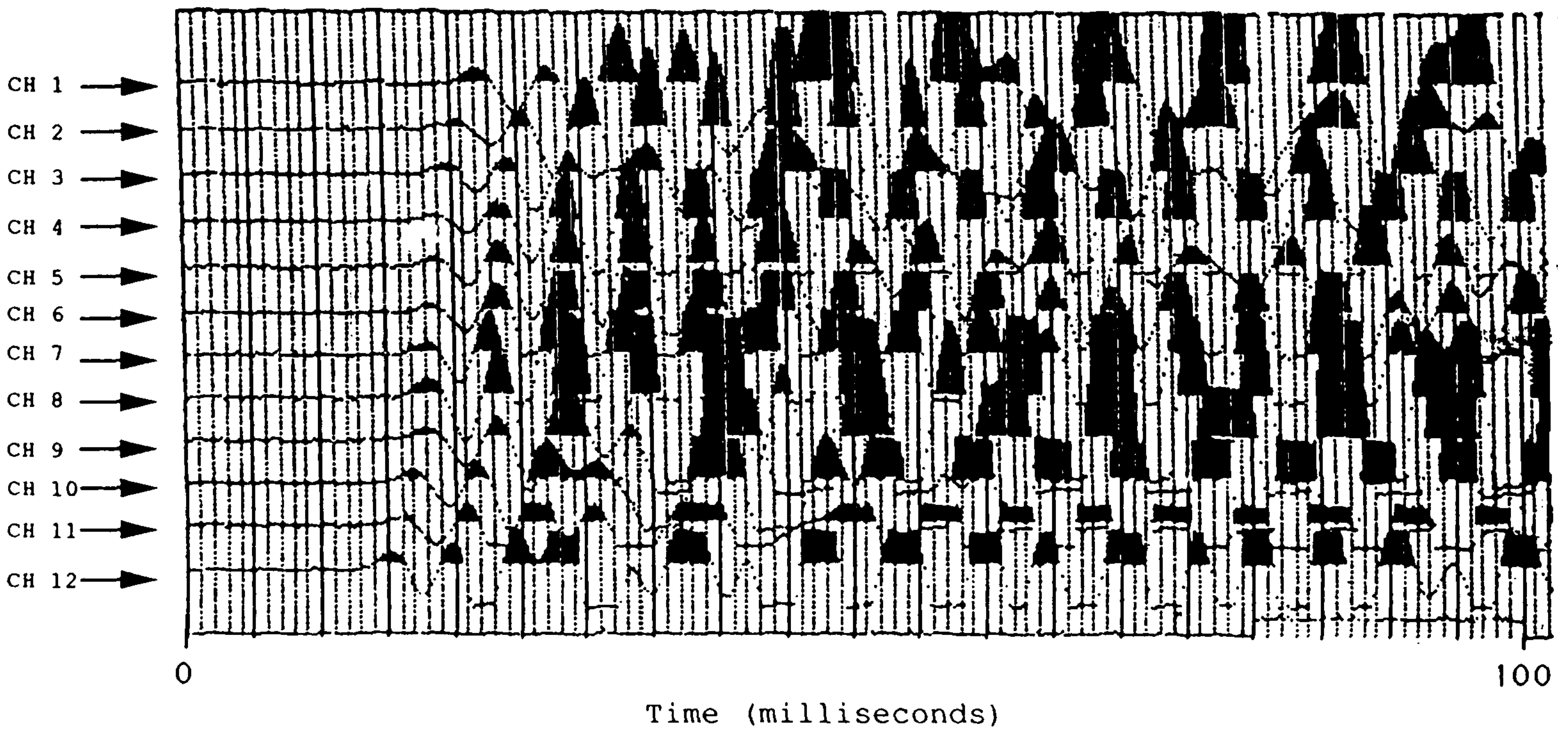

SH-WAVE SEISMIC RECORD FOR LINE 1 -- FORWARD PROFILE

2 meter source offset from nearest geophone

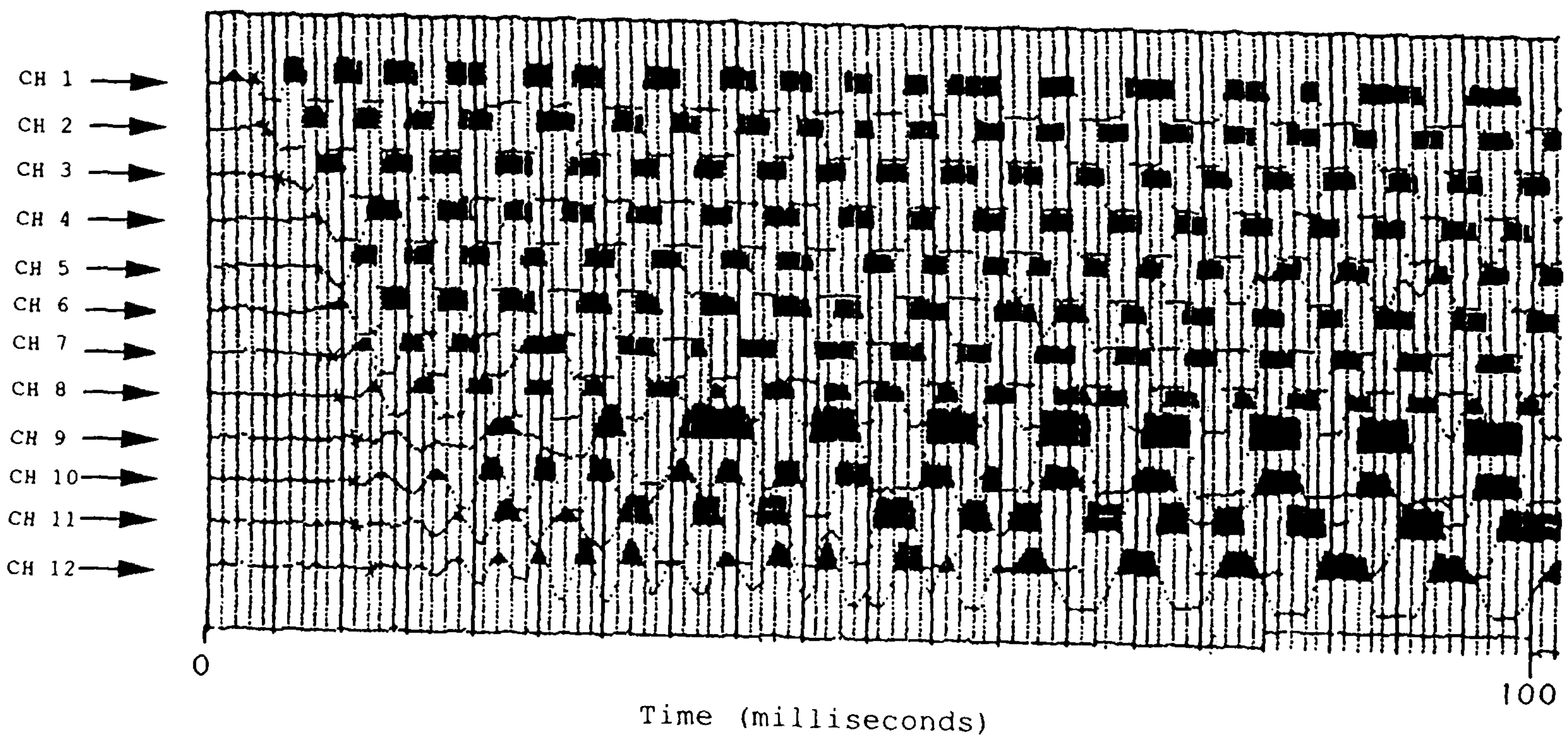

SH-WAVE SEISMIC RECORD FOR LINE 1 -- FORWARD PROFILE

22 meter source offset from nearest geophone

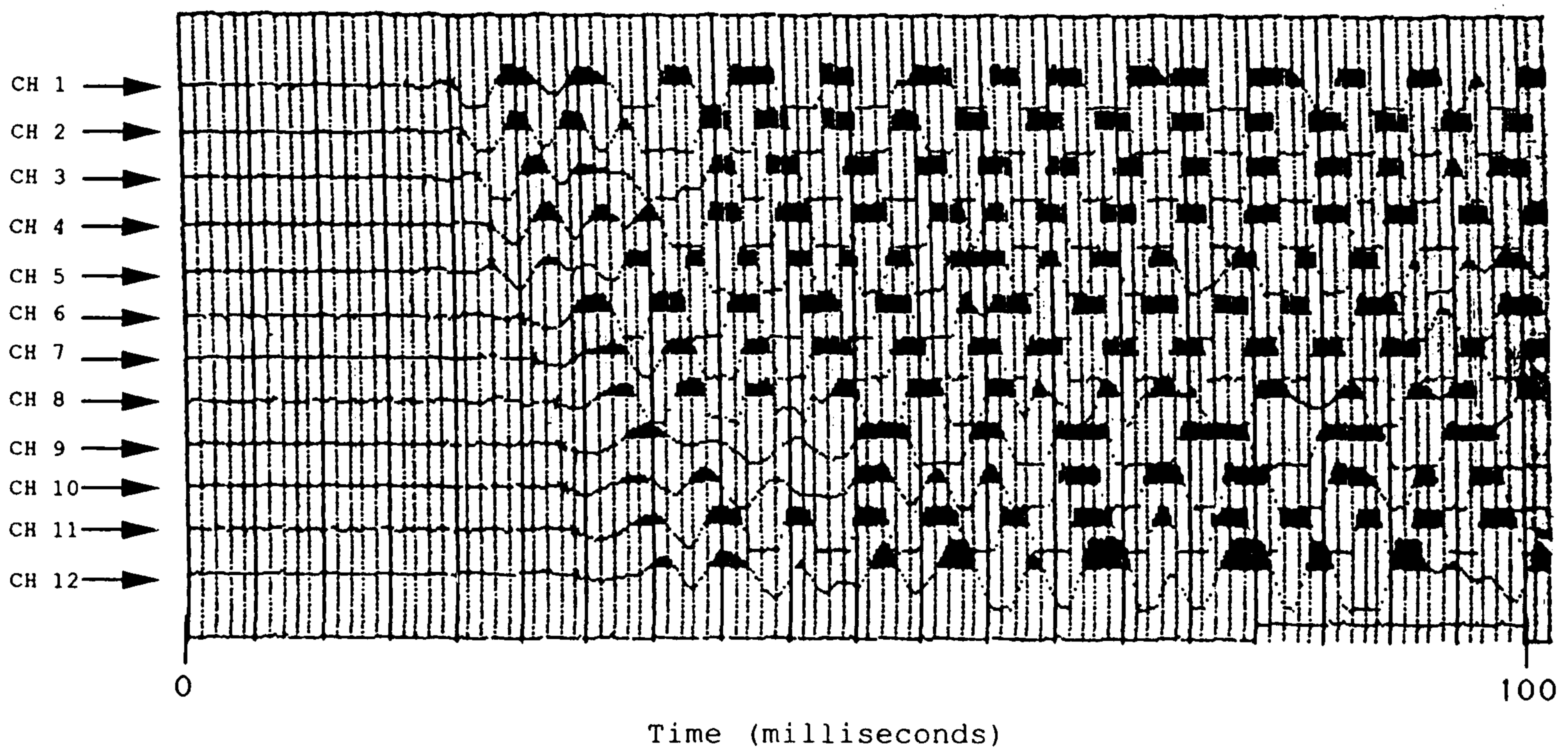

SH-WAVE SEISMIC RECORD FOR LINE 1 -- REVERSE PROFILE

2 meter source offset from nearest geophone

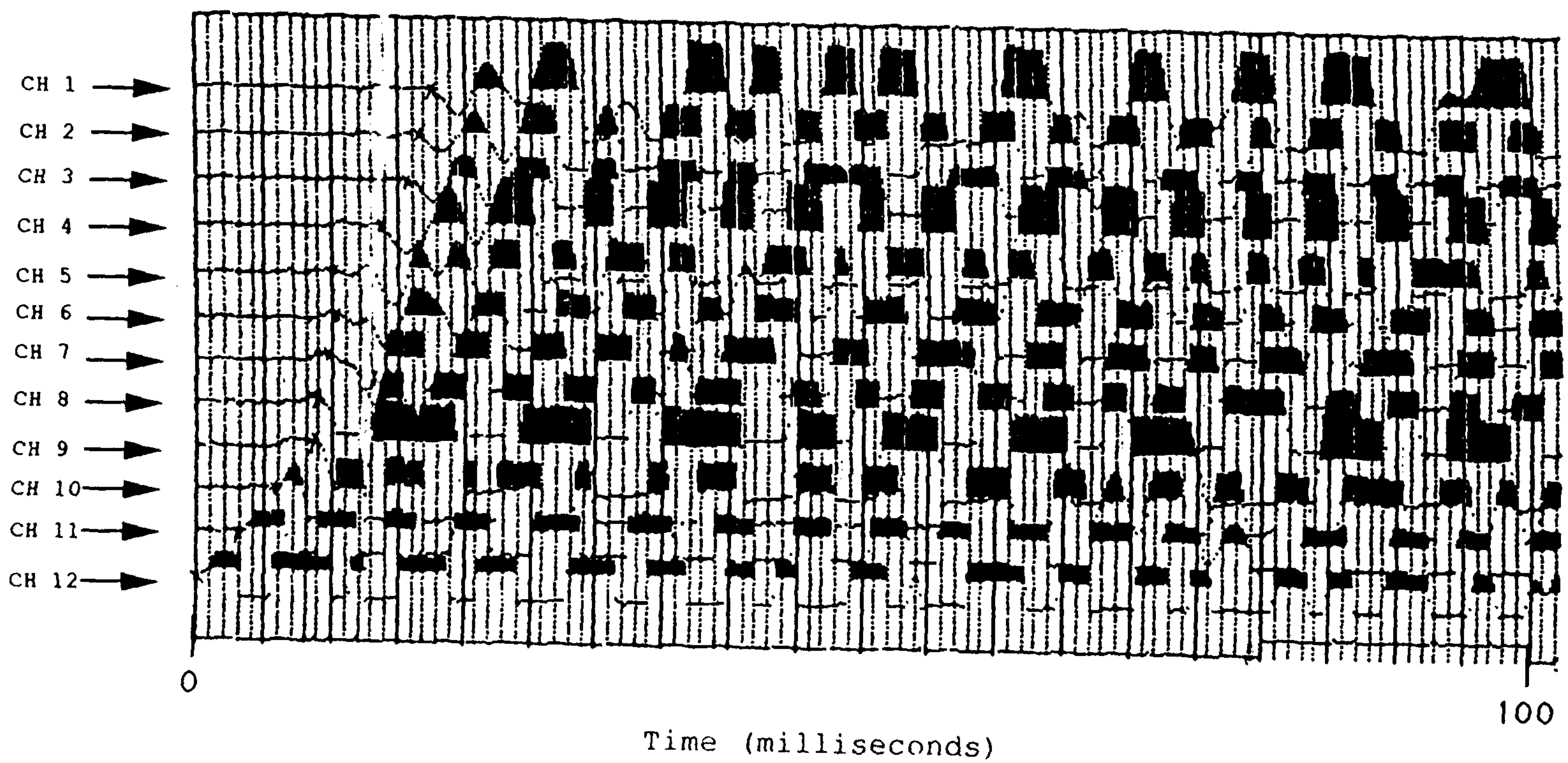

SH-WAVE SEISMIC RECORD FOR LINE 1 -- REVERSE PROFILE

22 meter source offset from nearest geophone

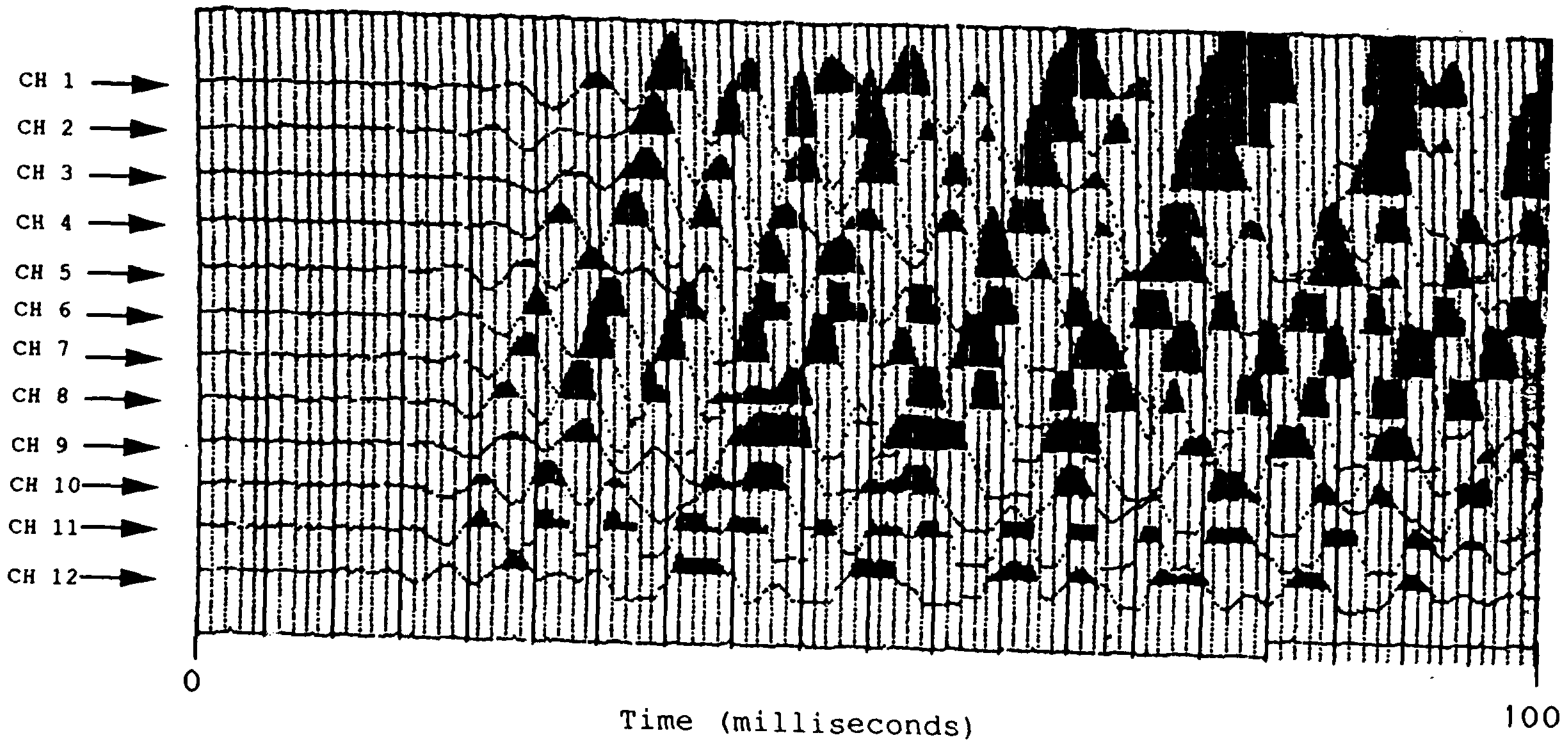

P-WAVE SEISMIC -- RADIAL ARRAY

15 meter source offset from nearest geophones (center shot)

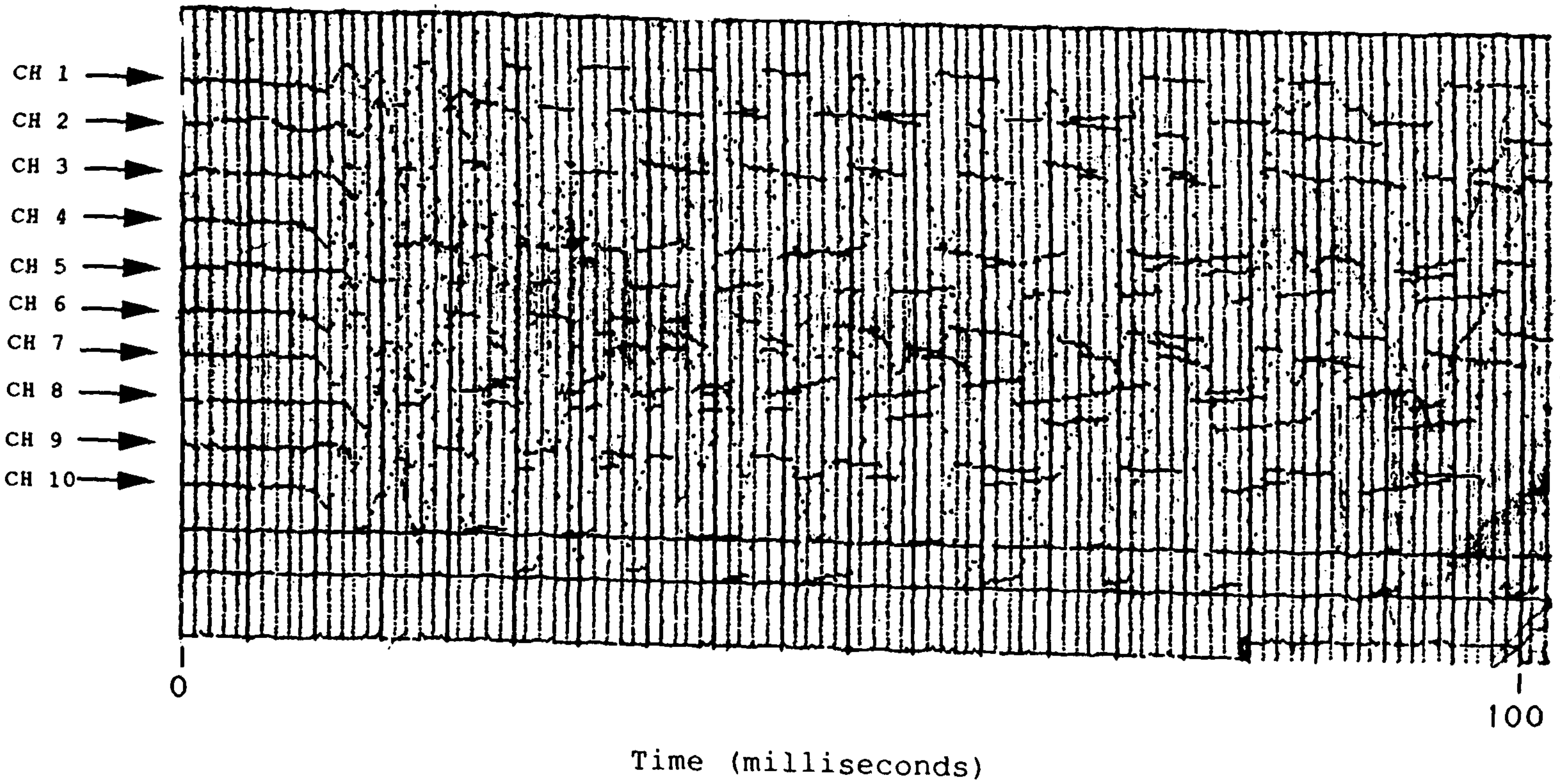

P-WAVE SEISMIC -- RADIAL ARRAY

20 meter source offset from nearest geophone in line 3

P-WAVE SEISMIC -- RADIAL ARRAY

20 meter source offset from nearest geophone in line 5

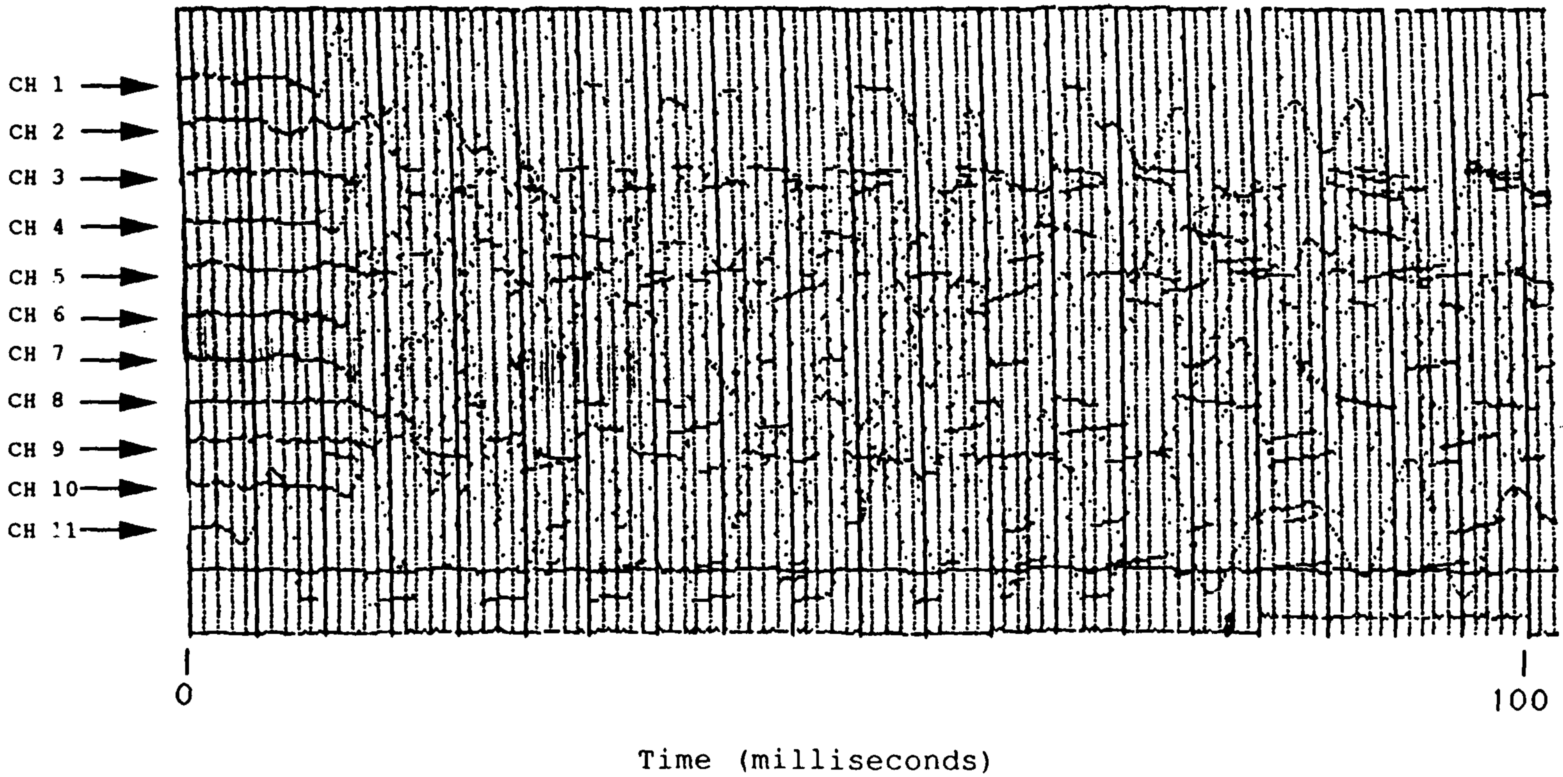

SV-WAVE SEISMIC RECORD FOR LINE 4 -- RADIAL ARRAY

10 meter source offset from nearest geophone (5 meters away from center shot)

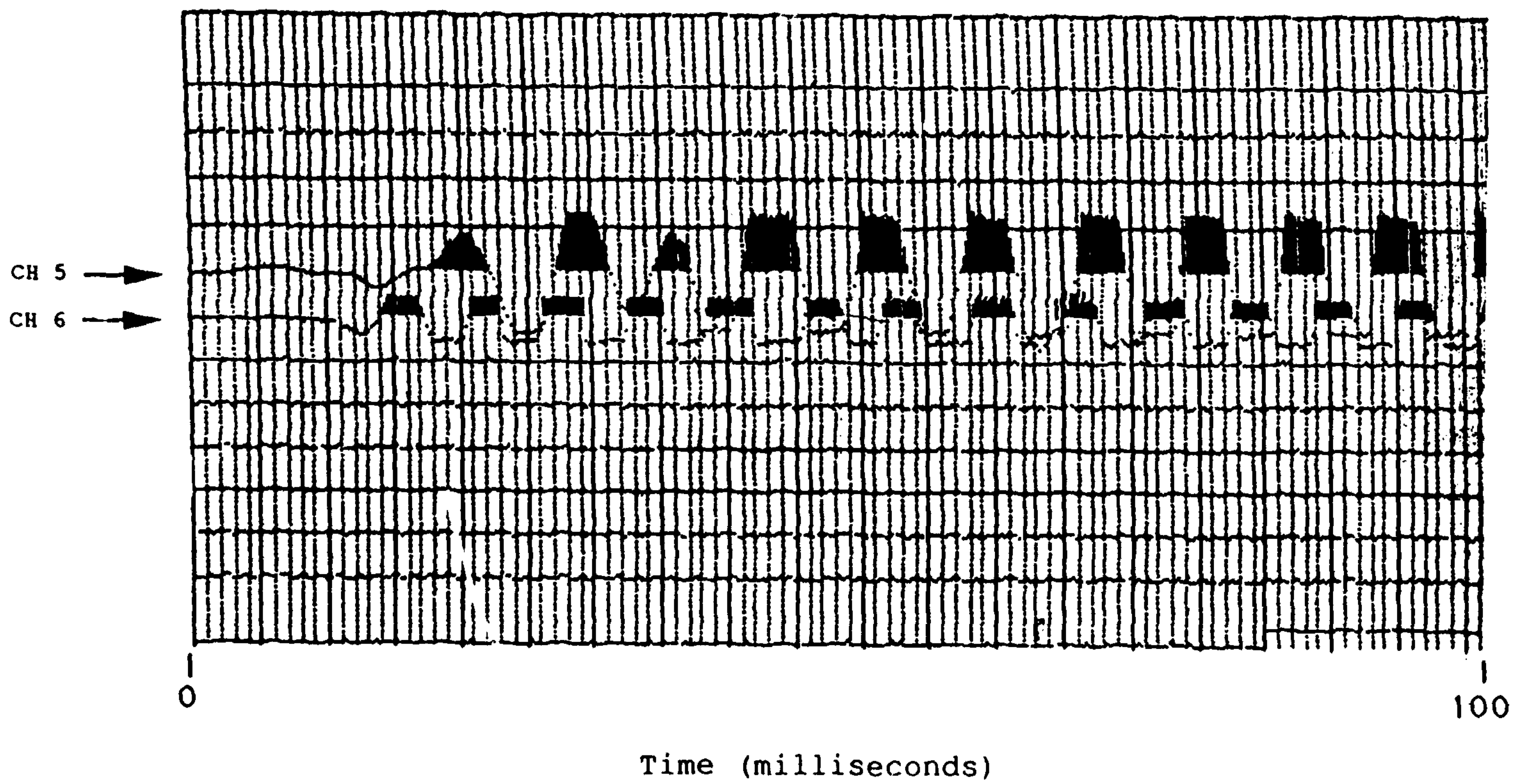

SV-WAVE SEISMIC RECORD FOR LINE 5 -- RADIAL ARRAY

15 meter source offset from nearest geophone (center shot)

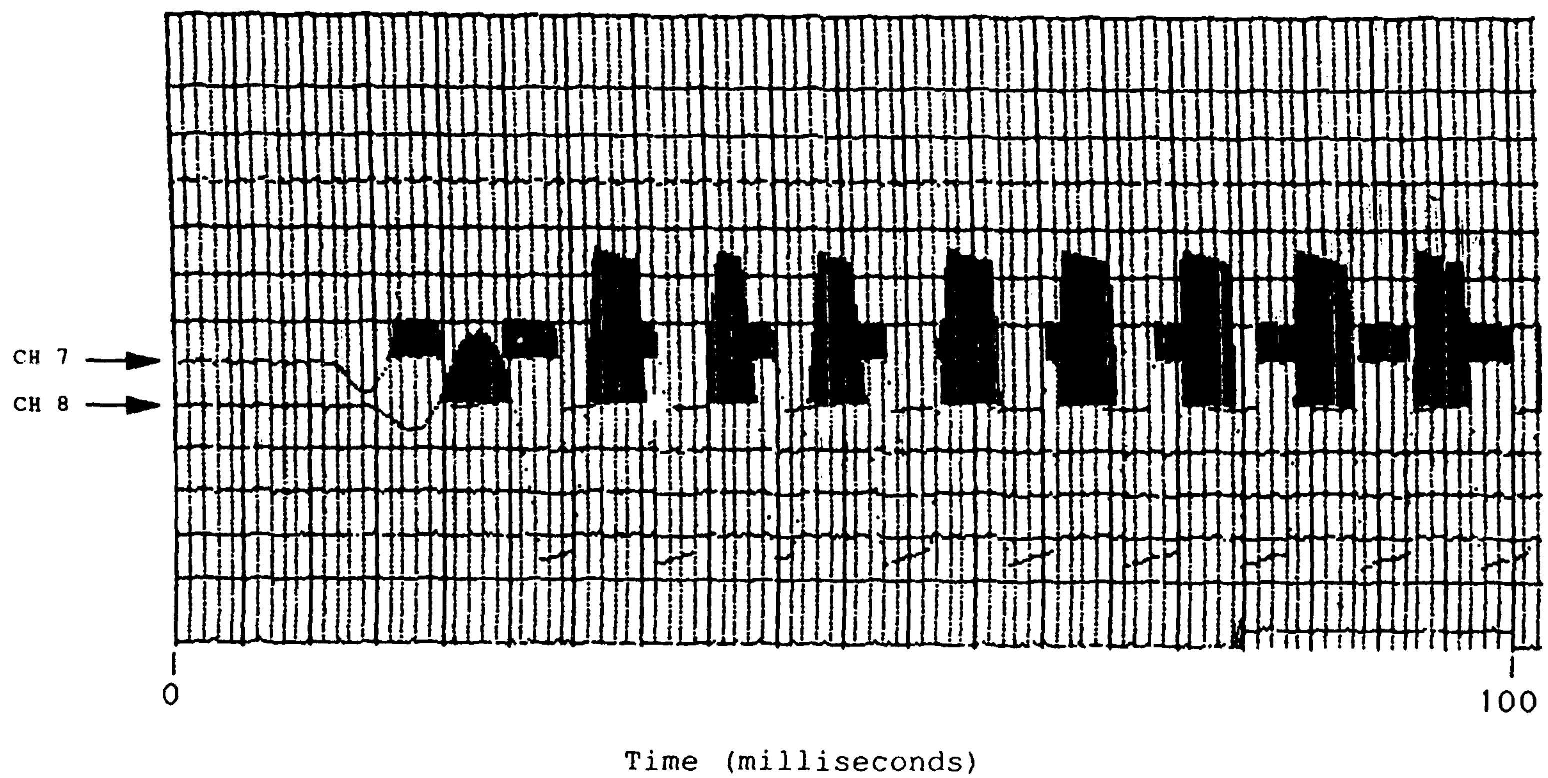

SV-WAVE SEISMIC RECORD FOR LINE 6 -- RADIAL ARRAY

15 meter source offset from nearest geophone (center shot)

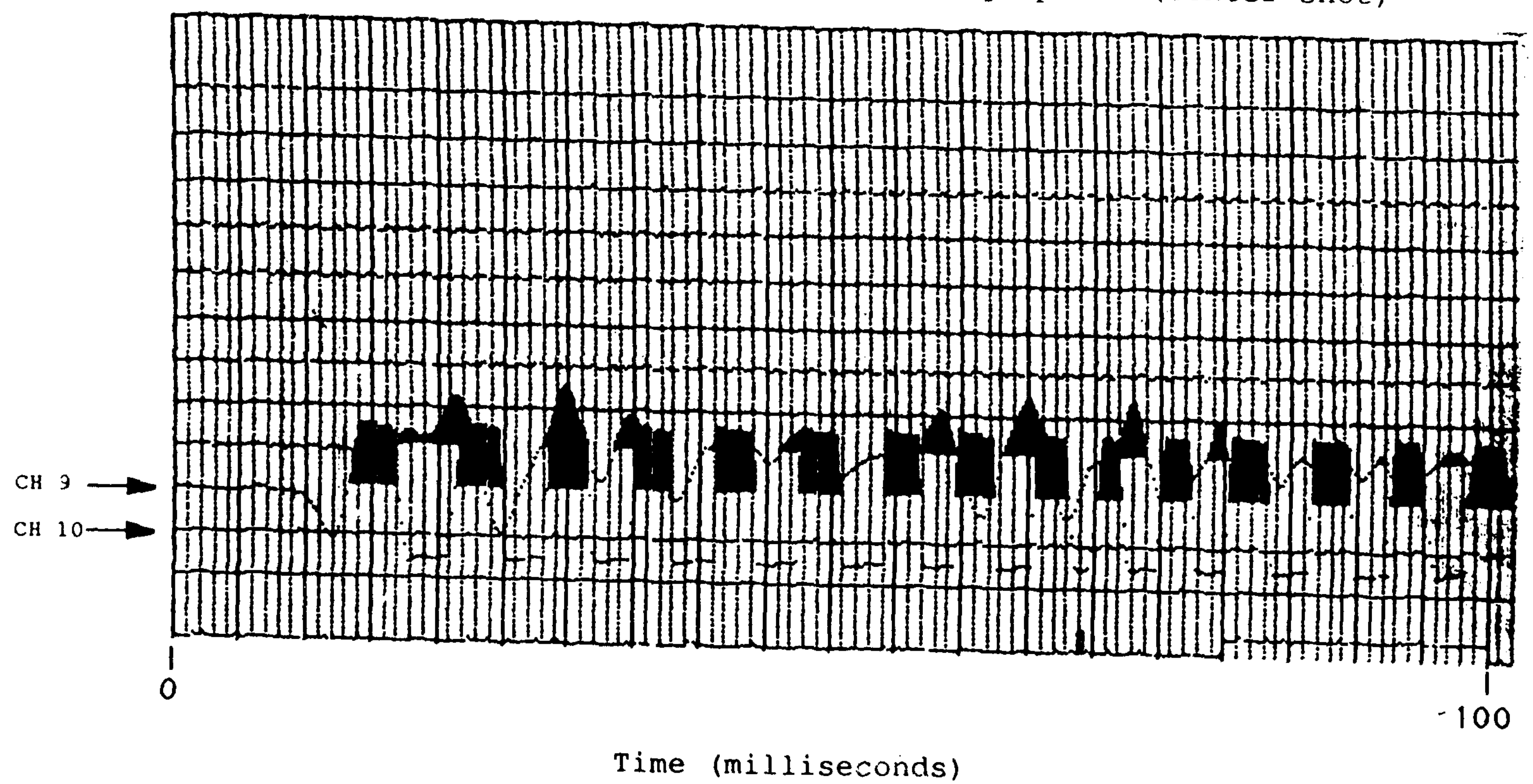

SH-WAVE SEISMIC RECORD FOR LINE 2 -- RADIAL ARRAY

20 meter source offset from nearest geophone (5 meters away from center shot)

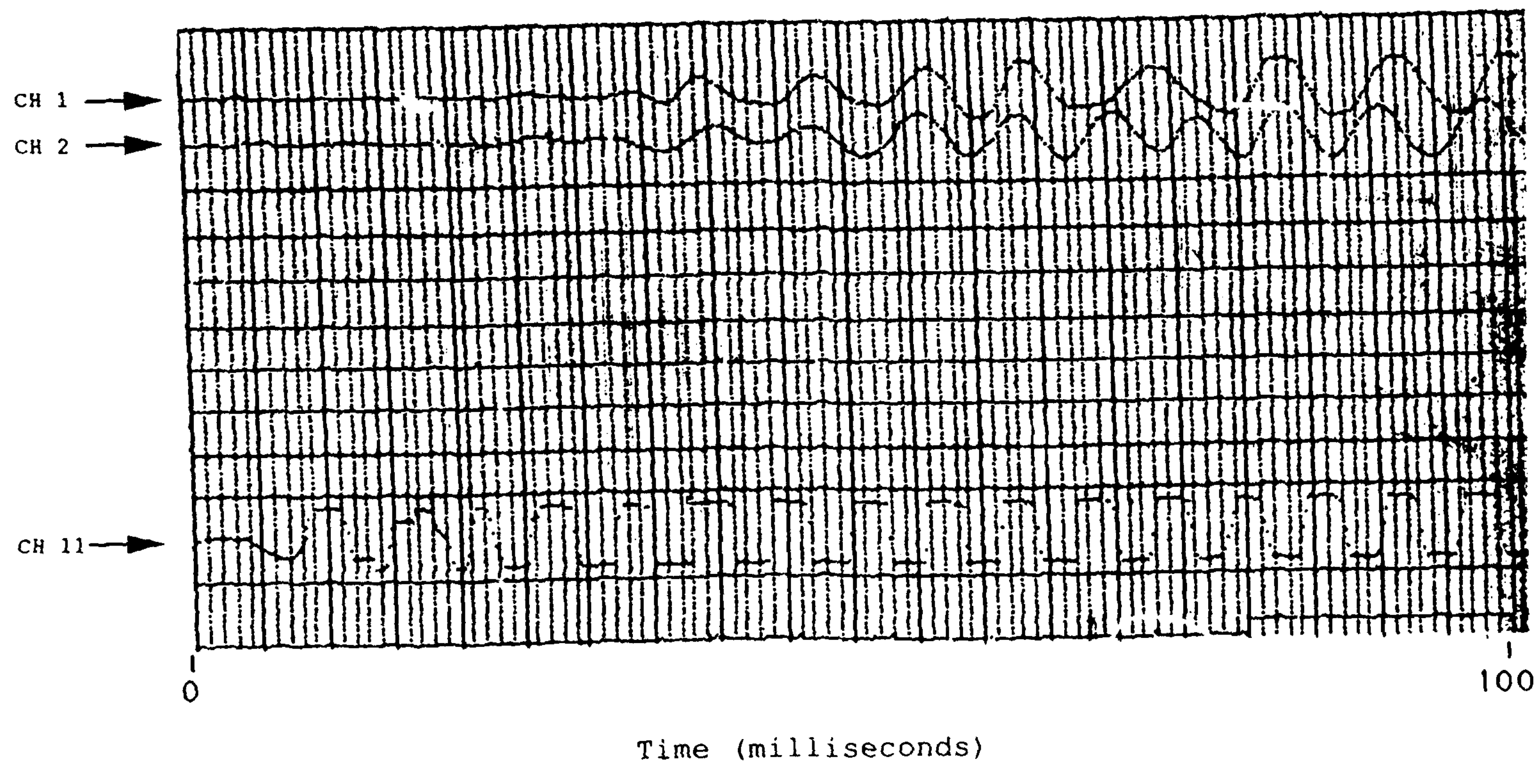

SH-WAVE SEISMIC RECORD FOR LINE 2 -- RADIAL ARRAY

15 meter source offset from nearest geophone (center shot)

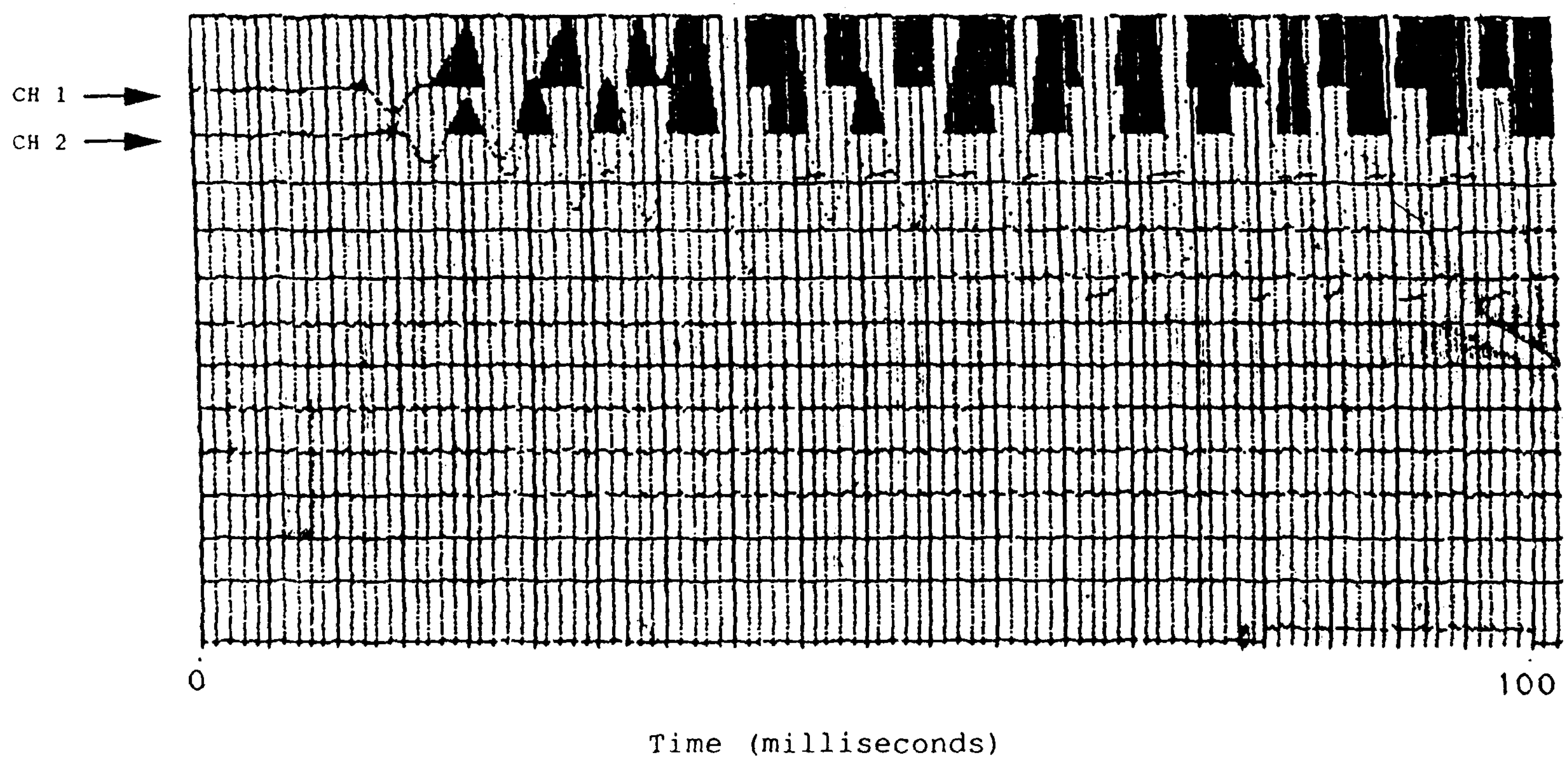

SH-WAVE SEISMIC RECORD FOR LINE 2 -- RADIAL ARRAY

10 meter source offset from nearest geophone (5 meters away from center shot)

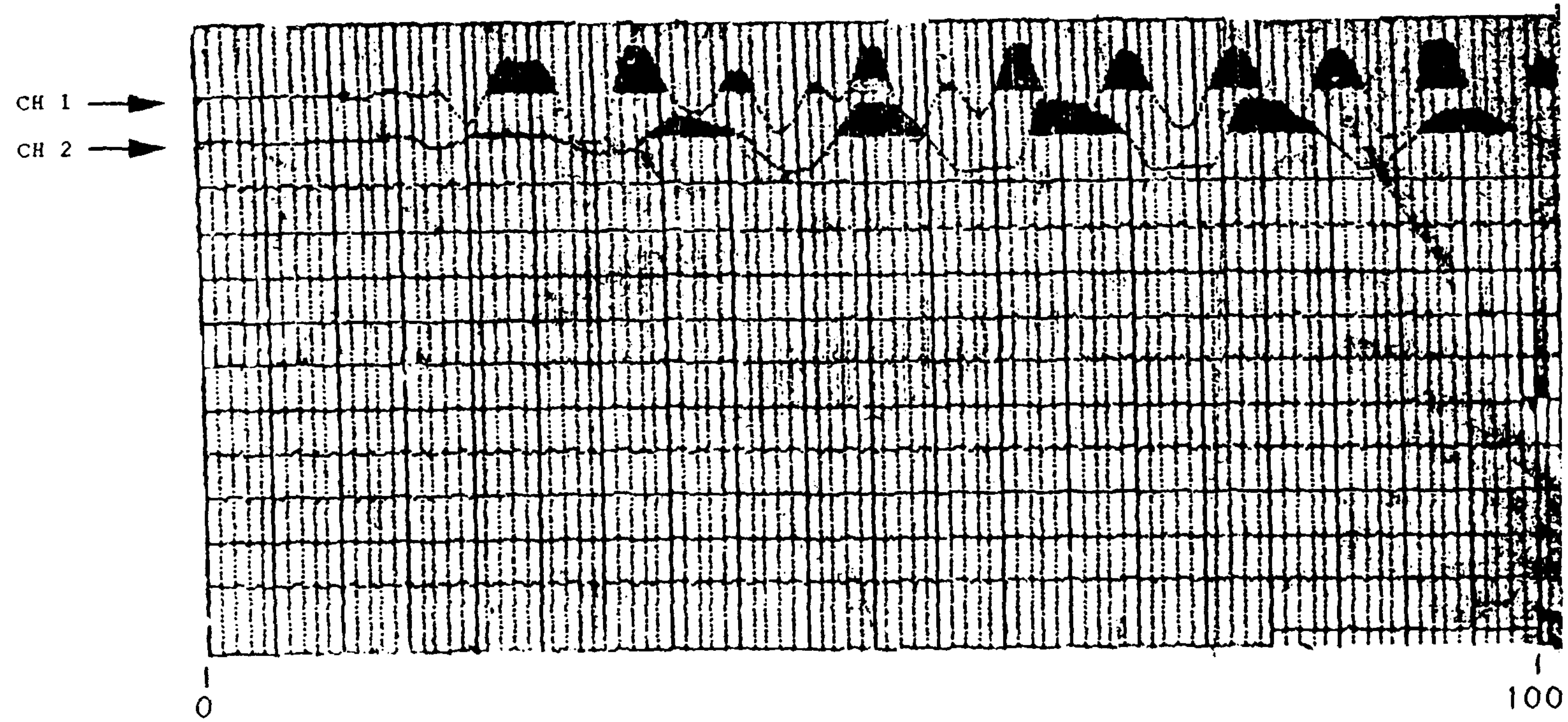

## REFERENCE LIST

Ackermann, H.D., Pankratz, L.W., and Dansereau,D., 1986, Resolution of ambiguities of seismic refraction traveltime curves: Geophys., 51, 223-235.

Alden, K., 1983, P- and S-wave Velocity Structure, Lajitas, Texas: report, Department of Geological Sciences, Southern Methodist Univesity, Dallas, TX, 75275.

Backus, G.E., 1962, Long-wave elastic anisotropy produced by horizontal layering: J. Geophys. Research, 67(11), 4427-4440.

Berryman, J.G., 1980, Long-wavelength propagation in composite elastic media I. Spherical inclusions: J. Acoust. Soc. Am., 68, 1809-1819.

Billings, M.P., 1972, Structural Geology, third edition: Prentice-Hall, Inc., Englewood Cliffs, New Jersey.

Biot, M.A., 1941, General theory of three-dimensional consolidation, J. Appl. Phys., 12, 155-164.

Biot, M.A., 1962, Mechanics of deformation and acoustic propagation in porous media: J. Appl. Phys., 33, 1482-1498.

Booth, D.C., Crampin, S., Chesnokov, E.M., and Krasnova,M.A., 1986, The effects of near vertical parallel cracks on shear-wave polarizations: Geophys. J. R. astr. Soc., 87, 583-594.

Bristow, J.R., 1960, Microcracks and the static and dynamic constants of annealed and heavily cold-worked metals: Brit. J. Appl. Phys., 11, 81-85.

Budiansky, B., and R.J. O'Connell, 1976, Elastic moduli of a cracked solid: Int. J. Solids Structures, 12, 81-97.

Budiansky, B., and R.J. O'Connell, 1980, Bulk dissipation in hetereogeneous media: Solid Earth Geophys. and Geotech., 42, 1-10.

Clark, S.P., 1966, Handbook of Physical Constants: rev. ed., Geol. Soc. Am., Mem. 97.

Compton, R.R., 1962, Manual of Field Geology: John Wiley and Sons, Inc., New York.

Crampin, S., 1978, Seismic wave propagation through a cracked solid; polarization as a possible dilitancy diagnostic: Geophys. J. R. astr. Soc., 53, 467-496.

Crampin, S., 1981, A review of wave motion in anisotropic and cracked elastic media: Wave Motion, 3, 343-391.

Crampin, S., 1984a, An introduction to wave propagation in anisotropic media: Geophys. J. R. astr. Soc., 76, 17-28.

Crampin, S., 1984b, Effective anisotropic elastic constants for wave propagation through cracked solids: Geophys. J. R. astr. Soc., 76, 135-145.

Crampin, S., Chesnokov, E.M., and Hipkin, R.G., 1984, Seismic anisotropy--the state of the art; II: Geophys. J. R. astr. Soc., 76, 1-15.

Crampin, S., 1985, Evaluation of anisotropy by shear-wave splitting: Geophysics, 50, 142-152.

Dandekar, D.P., 1968, Pressure dependence of the elastic constant of calcite: Phys. Rev., 172, 873-877.

Dobrin, M.B., 1976, Introduction to Geophysical Prospecting third ed.: McGraw-Hill Book Company.

Domzalski, W., 1956, Some Problems of Shallow Refraction Investigations: Geophys. Prospect., 4, 140-166.

Elliot, S.E. and Wiley, B.F., 1975, Compressional velocities of partially saturated, unconsolidated sands: Geophys., 40, 949-954.

Eshelby, J.D., 1957, The determination of the elastic field of an ellipsoidal inclusion, and related problems: Proc. Roy. Soc. of London, A241, 376-396.

Gardener, G.H.F., Gardner, L.W., and Gregory, A.R., 1974, Formation Velocity and Density: the diagnostic basis for stratigraphic traps: Geophys., 39, 770-780.

Gassmann, F., 1951, "Über die Elastizität poröser Medien, Mitteiluagen aus dem!: Inst. für Geophysik (Zu!rich), 17, 1-23.

Geertsma, J., 1957, The effect of fluid pressure decline on volumetric changes of porous rock: Trans., Assoc. of Industr. and Mech. Eng., 210, 331-340.

Golden, P., E. Herrin (Department of Geological Sciences, Southern Methodist University, Dallas, TX, 75275) and H.B. Durham (Sandia National Labs, Albuquerque, NM, 87185), 1985, The Lajitas Tx. Vibroseis™ Experiment: report.

Hudson, J.A., 1981, Wave speeds and attenuation of elastic waves in material containing cracks: Geophys. J. R. astr. Soc., 64, 133-150.

Hurlbut, C.S. Jr. and C. Klein, 1977, Manual of Mineralogy (after James.D. Dana), 19th ed.: John Wiley and Sons, Inc., New York.

King, M.S., 1966, Wave velocities in rocks as a function of changes in overburden pressure and pore fluid saturants: Geophys., 31, 50-73.

Klug, H.P. and L.E. Alexander, 1974, X-ray Diffraction Procedures, second ed.: John Wiley and Sons, Inc., New York.

Krohn, C.E., 1984, Geophone ground coupling: Geophys., 49(6), 722-731.

Kuster, G.T., and M.N. Toksöz, 1974, Velocity and attenuation of seismic waves in two-phase media; I. Theoretical formulations: Geophys., 39, 587-606.

Lewis, R.D., 1987, Construction of Temporary Seismometer Vaults Using "Jug Plug", The Mighty Miracle Mix: Earthquake Engineering and Geophysics Division of the U.S. Army Corps of Engineers (USACE), Waterways Experiment Station (WES), preprint.

Long, J.S.C., 1983, Investigation of equivalent porous medium permeability in networks of discontinuous fractures: Ph.D. thesis, University of California.

Lynn, H.B. and L.A. Thomsen, 1986, Reflection shear-wave data along the principal axes of azimuthal anisotropy: *presented at* SEG 56th Annual International Meeting, Houston.

Maxwell, R.A., 1971, The Big Bend of the Rio Grande, Guidebook 7: Bureau of Economic Geology, The University of Texas at Austin.

McSkimin, H.J., Andreatch, P., Jr., and Thurston, R.N., 1965, Elastic moduli of quartz versus hydrostatic pressure at 25° and -195.8°C: J. Appl. Phys., 36, 1624-1632.

Nur, A. and Byerlee, J.D., 1971, An exact effective stress law for elastic deformation of rock with fluids: J. Geophys. Res., 76, 6414-6419.

O'Connell, R.J. and B. Budiansky, 1974, Seismic velocities in dry and cracked solids: J. Geophys. Res., 79, 5412-5426.

O'Connell, R.J. and B. Budiansky, 1977, Viscoelastic properties of fluid-saturated cracked solids: J. Geophys. Res., 82, 5719-5735.

Plona, T.J., 1980, Observation of a second bulk compressional wave in a porous medium at ultrasonic frequencies: Appl. Phys. Lett., 36, 259-261.

Prior, D.J., Knipe, R.J., Bates, M.P., Grant, N.T., Law, R.D., Lloyd, G.E., Welbon, A., Agar, S.M., Brodie, K.H. Maddock, R.H., Rutter, E.H., White, S.H., Bell, T.H., Ferguson, C.C., and Wheeler, J., 1987, Orientation of specimens: Essential data for all fields of geology. Geology, 15, 829-831.

Pai, C.S., and K.E. Hanson, 1986, Shear-wave birefringence; a laboratory study: *presented at* SEG 56th Annual International Meeting, Houston.

Reinke, R. and J. Logan, 1983, Results of the Seismic Surveys at the Lajitas, Texas Seismic Array: Site Characterization and Seismology Section, Civil Engineering Research Division, Air Force Weapons Laboratory, Kirtland AFB NM 87117.

Scott, J.H., 1973, Seismic refraction modeling by computer: Geophys., 38(2), 271-284.

Simmons, G., 1965, Ultrsonics in Geology: *reprinted from the* Proceedings of the IEEE, 53(10), 1337-1345.

Simmons, G. and D. Richter, 1974, Microcracks in rocks: *in* The Physics and Chemistry of Minerals and Rocks, R.G. J. Strens. London (ed.), Wiley Interscience Publication, c1976, New York.

Sjögren, B., 1984, Shallow Refraction Seismics: Chapman and Hall Ltd.

Spencer, T.W., 1965, Refraction along a layer: Geophys., 30(3), 369-388.

Sorrells, G.G., 1961, Variations of Longitudinal Wave Velocity in Low Porosity Carbonate Rocks: Masters thesis, Southern Methodist University, Dallas, TX, 75275.

Telford, W.M., Geldhart, L.P., Sheriff, R.E., and Keys, D.A., 1976, Refraction field methods and equipment: *in* Applied Geophysics, Press Syndicate of the University of Cambridge.

Thomsen, L., 1985, Biot-consistent elastic moduli of porous rocks; Low-frequency limit: Geophys., 50(12), 2797-2807.

Tipler, P., 1982, Solids and Fluids: *in* Physics, second ed., Worth Publishers, Inc.

Toksöz, M.N., Cheng, C.H., and Timur, A., 1976, Velocities of seismic waves in porous rocks: Geophys., 41(4), 621-645.

Wilkens, R., Simmons, G., and Caruso, L., 1984, The ratio of $V_p/V_s$ as a discriminant of composition for siliceous limestones: Geophys., 49(11), 1850-1860.

Wyllie, M.R.J., Gregory, A.R.,and Gardner, L.W., 1956, Elastic wave velocities in heterogeneous and porous media: Geophys., 21, 41-70.

Wyllie, M.R.J., Gregory, A.R., and Gardner, G.H.F., 1958, An experimental investigation of factors affecting elastic wave velocities in porous media: Geophys., 23, 459-493.

Professor Keiiti Aki
Center for Earth Sciences
University of Southern California
University Park
Los Angeles, CA 90089-0741

Professor Thomas Ahrens
Seismological Lab, 252-21
Div. of Geological and Planetary Sciences
California Institute of Technology
Pasadena, CA 91125

Professor Charles B. Archambeau
Cooperative Institute for Resch in Environmental Sciences
University of Colorado
Boulder, CO 80309

Dr. Thomas C. Bache Jr.
Science Applications Int'l Corp.
10210 Campus Point Drive
San Diego, CA 92121 (2 copies)

Dr. Muawia Barazangi
Institute for the Study of of the Continent
Cornell University
Ithaca, NY 14853

Dr. Douglas R. Baumgardt
Signal Analysis & Systems Div.
ENSCO, Inc.
5400 Port Royal Road
Springfield, VA 22151-2388

Dr. Jonathan Berger
Institute of Geophysics and Planetary Physics
Scripps Institution of Oceanography
A-025
University of California, San Diego
La Jolla, CA 92093

Dr. S. Bratt
Science Applications Int'l Corp.
10210 Campus Point Drive
San Diego, CA 92121

Dr. Lawrence J. Burdick
Woodward-Clyde Consultants
P.O. Box 93245
Pasadena, CA 91109-3245 (2 copies)

Professor Robert W. Clayton
Seismological Laboratory/Div. of Geological & Planetary Sciences
California Institute of Technology
Pasadena, CA 91125

Dr Karl Coyner
New England Research, Inc.
76 Olcott Drive
White River Junction, VT 05001

Dr. Vernon F. Cormier
Department of Geology & Geophysics
U-45, Room 207
The University of Conneticut
Storrs, Connecticut 06268

Dr. Steven Day
Dept. of Geological Sciences
San Diego State U.
San Diego, CA 92182

Dr. Zoltan A. Der
ENSCO, Inc.
5400 Port Royal Road
Springfield, VA 22151-2388

Professor John Ferguson
Center for Lithospheric Studies
The University of Texas at Dallas
P.O. Box 830688
Richardson, TX 75083-0688

Professor Stanley Flatte'
Applied Sciences Building
University of California,
Santa Cruz, CA 95064

Dr. Alexander Florence
SRI International
333 Ravenswood Avenue
Menlo Park, CA 94025-3493

Professor Steven Grand
University of Texas at Austin
Dept of Geological Sciences
Austin, TX 78713-7909

Dr. Henry L. Gray
Associate Dean of Dedman College
Department of Statistical Sciences
Southern Methodist University
Dallas, TX 75275

Professor Roy Greenfield
Geosciences Department
403 Deike Building
The Pennsylvania State University
University Park, PA 16802

Professor David G. Harkrider
Seismological Laboratory
Div of Geological & Planetary Sciences
California Institute of Technology
Pasadena, CA 91125

Professor Donald V. Helmberger
Seismological Laboratory
Div of Geological & Planetary Sciences
California Institute of Technology
Pasadena, CA 91125

Professor Eugene Herrin
Institute for the Study of Earth
and Man/Geophysical Laboratory
Southern Methodist University
Dallas, TX 75275

Professor Robert B. Herrmann
Department of Earth & Atmospheric
Sciences
Saint Louis University
Saint Louis, MO 63156

Professor Bryan Isacks
Cornell University
Dept of Geological Sciences
SNEE Hall
Ithaca, NY 14850

Professor Lane R. Johnson
Seismographic Station
University of California
Berkeley, CA 94720

Professor Thomas H. Jordan
Department of Earth, Atmospheric
and Planetary Sciences
Mass Institute of Technology
Cambridge, MA 02139

Dr. Alan Kafka
Department of Geology &
Geophysics
Boston College
Chestnut Hill, MA 02167

Professor Leon Knopoff
University of California
Institute of Geophysics
& Planetary Physics
Los Angeles, CA 90024

Professor Charles A. Langston
Geosciences Department
403 Deike Building
The Pennsylvania State University
University Park, PA 16802

Professor Thorne Lay
Department of Geological Sciences
1006 C.C. Little Building
University of Michigan
Ann Arbor, MI 48109-1063

Dr. Randolph Martin III
New England Research, Inc.
76 Olcott Drive
White River Junction, VT 05001

Dr. Gary McCartor
Mission Research Corp.
735 State Street
P.O. Drawer 719
Santa Barbara, CA 93102 (2 copies)

Professor Thomas V. McEvilly
Seismographic Station
University of California
Berkeley, CA 94720

Dr. Keith L. McLaughlin
S-CUBED,
A Division of Maxwell Laboratory
P.O. Box 1620
La Jolla, CA 92038-1620

Professor William Menke
Lamont-Doherty Geological Observatory
of Columbia University
Palisades, NY 10964

Professor Brian J. Mitchell
Department of Earth & Atmospheric
Sciences
Saint Louis University
Saint Louis, MO 63156

Mr. Jack Murphy
S-CUBED
A Division of Maxwell Laboratory
11800 Sunrise Valley Drive
Suite 1212
Reston, VA 22091 (2 copies)

Professor J. A. Orcutt
IGPP, A-205
Scripps Institute of Oceanography
Univ. of California, San Diego
La Jolla, CA 92093

Professor Keith Priestley
University of Nevada
Mackay School of Mines
Reno, NV 89557

Professor Paul G. Richards
Lamont-Doherty Geological
Observatory of Columbia Univ.
Palisades, NY 10964

Wilmer Rivers
Teledyne Geotech
314 Montgomery Street
Alexandria, VA 22314

Dr. Alan S. Ryall, Jr.
Center of Seismic Studies
1300 North 17th Street
Suite 1450
Arlington, VA 22209-2308 (4 copies)

Professor Charles G. Sammis
Center for Earth Sciences
University of Southern California
University Park
Los Angeles, CA 90089-0741

Professor Christopher H. Scholz
Geological Sciences
Lamont-Doherty Geological Observatory
Palisades, NY 10964

Dr. Jeffrey L. Stevens
S-CUBED,
A Division of Maxwell Laboratory
P.O. Box 1620
La Jolla, CA 92038-1620

Professor Brian Stump
Institute for the Study of Earth & Man
Geophysical Laboratory
Southern Methodist University
Dallas, TX 75275

Professor Ta-liang Teng
Center for Earth Sciences
University of Southern California
University Park
Los Angeles, CA 90089-0741

Dr. Clifford Thurber
State University of New York at
Stony Brooks
Dept of Earth and Space Sciences
Stony Brook, NY 11794-2100

Professor M. Nafi Toksoz
Earth Resources Lab
Dept of Earth, Atmospheric and
Planetary Sciences
Massachusetts Institute of Technology
42 Carleton Street
Cambridge, MA 02142

Professor Terry C. Wallace
Department of Geosciences
Building #77
University of Arizona
Tucson, AZ 85721

Weidlinger Associates
ATTN: Dr. Gregory Wojcik
4410 El Camino Real, Suite 110
Los Altos, CA 94022

Professor Francis T. Wu
Department of Geological Sciences
State University of New York
at Binghamton
Vestal, NY 13901

## OTHERS (United States)

Dr. Monem Abdel-Gawad
Rockwell Internat'l Science Center
1049 Camino Dos Rios
Thousand Oaks, CA 91360

Professor Shelton S. Alexander
Geosciences Department
403 Deike Building
The Pennsylvania State University
University Park, PA 16802

Dr. Ralph Archuleta
Department of Geological
Sciences
Univ. of California at
Santa Barbara
Santa Barbara, CA

J. Barker
Department of Geological Sciences
State University of New York
at Binghamton
Vestal, NY 13901

Mr. William J. Best
907 Westwood Drive
Vienna, VA 22180

Dr. N. Biswas
Geophysical Institute
University of Alaska
Fairbanks, AK 99701

Dr. G. A. Bollinger
Department of Geological Sciences
Virginia Polytechnical Institute
21044 Derring Hall
Blacksburg, VA 24061

Mr. Roy Burger
1221 Serry Rd.
Schenectady, NY 12309

Dr. Robert Burridge
Schlumberger-Doll Resch Ctr.
Old Quarry Road
Ridgefield, CT 06877

Science Horizons, Inc.
ATTN: Dr. Theodore Cherry
710 Encinitas Blvd., Suite 101
Encinitas, CA 92024 (2 copies)

Professor Jon F. Claerbout
Professor Amos Nur
Dept. of Geophysics
Stanford University
Stanford, CA 94305 (2 copies)

Dr. Anton W. Dainty
Earth Resources Lab
Massachusetts Institute of Technology
42 Carleton Street
Cambridge, MA 02142

Professor Adam Dziewonski
Hoffman Laboratory
Harvard University
20 Oxford St.
Cambridge, MA 02138

Professor John Ebel
Dept of Geology and Geophysics
Boston College
Chestnut Hill, MA 02167

Dr. Donald Forsyth
Dept of Geological Sciences
Brown University
Providence, RI 02912

Dr. Anthony Gangi
Texas A&M University
Department of Geophysics
College Station, TX 77843

Dr. Freeman Gilbert
Institute of Geophysics &
Planetary Physics
University of California, San Diego
P.O. Box 109
La Jolla, CA 92037

Mr. Edward Giller
Pacific Seirra Research Corp.
1401 Wilson Boulevard
Arlington, VA 22209

Dr. Jeffrey W. Given
Sierra Geophysics
11255 Kirkland Way
Kirkland, WA 98033

Rong Song Jih
Teledyne Geotech
314 Montgomery Street
Alexandria, Virginia 22314

Professor F.K. Lamb
University of Illinois at
Urbana-Champaign
Department of Physics
1110 West Green Street
Urbana, IL 61801

Dr. Arthur Lerner-Lam
Lamont-Doherty Geological Observatory
of Columbia University
Palisades, NY 10964

Dr. L. Timothy Long
School of Geophysical Sciences
Georgia Institute of Technology
Atlanta, GA 30332

Dr. Peter Malin
University of California at
Santa Barbara
Institute for Central Studies
Santa Barbara, CA 93106

Dr. George R. Mellman
Sierra Geophysics
11255 Kirkland Way
Kirkland, WA 98033

Dr. Bernard Minster
IGPP, A-205
Scripps Institute of Oceanography
Univ. of California, San Diego
La Jolla, CA 92093

Professor John Nabelek
College of Oceanography
Oregon State University
Corvallis, OR 97331

Dr. Geza Nagy
U. California, San Diego
Dept of Ames, M.S. B-010
La Jolla, CA 92093

Dr. Jack Oliver
Department of Geology
Cornell University
Ithaca, NY 14850

Dr. Robert Phinney/Dr. F. A. Dahlen
Dept of Geological
Geological Science University
Princeton University
Princeton, NJ 08540

RADIX System, Inc.
Attn: Dr. Jay Pulli
2 Taft Court, Suite 203
Rockville, Maryland 20850

Dr. Norton Rimer
S-CUBED
A Division of Maxwell Laboratory
P.O. 1620
La Jolla, CA 92038-1620

Professor Larry J. Ruff
Department of Geological Sciences
1006 C.C. Little Building
University of Michigan
Ann Arbor, MI 48109-1063

Dr. Richard Sailor
TASC Inc.
55 Walkers Brook Drive
Reading, MA 01867

Thomas J. Sereno, Jr.
Science Application Int'l Corp.
10210 Campus Point Drive
San Diego, CA 92121

Dr. David G. Simpson
Lamont-Doherty Geological Observ.
of Columbia University
Palisades, NY 10964

Dr. Bob Smith
Department of Geophysics
University of Utah
1400 East 2nd South
Salt Lake City, UT 84112

Dr. S. W. Smith
Geophysics Program
University of Washington
Seattle, WA 98195

Dr. Stewart Smith
IRIS Inc.
1616 N. Fort Myer Drive
Suite 1440
Arlington, VA 22209

Rondout Associates
ATTN: Dr. George Sutton,
Dr. Jerry Carter, Dr. Paul Pomeroy
P.O. Box 224
Stone Ridge, NY 12484 (4 copies)

Dr. L. Sykes
Lamont Doherty Geological Observ.
Columbia University
Palisades, NY 10964

Dr. Pradeep Talwani
Department of Geological Sciences
University of South Carolina
Columbia, SC 29208

Dr. R. B. Tittmann
Rockwell International Science Center
1049 Camino Dos Rios
P.O. Box 1085
Thousand Oaks, CA 91360

Professor John H. Woodhouse
Hoffman Laboratory
Harvard University
20 Oxford St.
Cambridge, MA 02138

Dr. Gregory B. Young
ENSCO, Inc.
5400 Port Royal Road
Springfield, VA 22151-2388

Dr. Gregory van der Vink
IRIS
Suite 1440
1616 North Fort Myer Drive
Arlington, VA 22209

U.S. GOVERNMENT PRINTING OFFICE

FOREIGN (OTHERS)

Dr. Peter Basham
Earth Physics Branch
Geological Survey of Canada
1 Observatory Crescent
Ottawa, Ontario
CANADA K1A OY3

Professor Ari Ben-Menahem
Dept of Applied Mathematics
Weizman Institute of Science
Rehovot
ISRAEL 951729

Dr. Eduard Berg
Institute of Geophysics
University of Hawaii
Honolulu, HI 96822

Dr. Michel Bouchon - Universite
Scientifique et Medicale de Grenob
Lab de Geophysique - Interne et
Tectonophysique - I.R.I.G.M-B.P.
38402 St. Martin D'Heres
Cedex FRANCE

Dr. Hilmar Bungum/NTNF/NORSAR
P.O. Box 51
Norwegian Council of Science,
Industry and Research, NORSAR
N-2007 Kjeller, NORWAY

Dr. Michel Campillo
I.R.I.G.M.-B.P. 68
38402 St. Martin D'Heres
Cedex, FRANCE

Dr. Kin-Yip Chun
Geophysics Division
Physics Department
University of Toronto
Ontario, CANADA M5S 1A7

Dr. Alan Douglas
Ministry of Defense
Blacknest, Brimpton,
Reading RG7-4RS
UNITED KINGDOM

Dr. Manfred Henger
Fed. Inst. For Geosciences & Nat'l Res.
Postfach 510153
D-3000 Hannover 51
FEDERAL REPUBLIC OF GERMANY

Ms. Eva Johannisson
Senior Research Officer
National Defense Research Inst.
P.O. Box 27322
S-102 54 Stockholm
SWEDEN

Tormod Kvaerna
NTNF/NORSAR
P.O. Box 51
N-2007 Kjeller, NORWAY

Mr. Peter Marshall, Procurement
Executive, Ministry of Defense
Blacknest, Brimpton,
Reading FG7-4RS
UNITED KINGDOM (3 copies)

Dr. Robert North
Geophysics Division
Geological Survey of Canada
1 Observatory crescent
Ottawa, Ontario
CANADA, K1A OY3

Dr. Frode Ringdal
NTNF/NORSAR
P.O. Box 51
N-2007 Kjeller, NORWAY

Dr. Jorg Schlittenhardt
Federal Inst. for Geosciences & Nat'l Res.
Postfach 510153
D-3000 Hannover 51
FEDERAL REPUBLIC OF GERMANY

University of Hawaii
Institute of Geophysics
ATTN: Dr. Daniel Walker
Honolulu, HI 96822

FOREIGN CONTRACTORS

Dr. Ramon Cabre, S.J.
Observatorio San Calixto
Casilla 5939
La Paz Bolivia

Professor Peter Harjes
Institute for Geophysik
Rhur University/Bochum
P.O. Box 102148, 4630 Bochum 1
FEDERAL REPUBLIC OF GERMANY

Dr. E. Husebye
NTNF/NORSAR
P.O. Box 51
N-2007 Kjeller, NORWAY

Professor Brian L.N. Kennett
Research School of Earth Sciences
Institute of Advanced Studies
G.P.O. Box 4
Canberra 2601
AUSTRALIA

Dr. B. Massinon
Societe Radiomana
27, Rue Claude Bernard
7,005, Paris, FRANCE (2 copies)

Dr. Pierre Mechler
Societe Radiomana
27, Rue Claude Bernard
75005, Paris, FRANCE

Dr. Svein Mykkeltveit
NTNF/NORSAR
P.O. Box 51
N-2007 Kjeller, NORWAY (3 copies)

GOVERNMENT

Dr. Ralph Alewine III
DARPA/NMRO
1400 Wilson Boulevard
Arlington, VA 22209-2308

Dr. Robert Blandford
DARPA/NMRO
1400 Wilson Boulevard
Arlington, VA 22209-2308

Sandia National Laboratory
ATTN: Dr. H. B. Durham
Albuquerque, NM 87185

Dr. Jack Evernden
USGS-Earthquake Studies
345 Middlefield Road
Menlo Park, CA 94025

U.S. Geological Survey
ATTN: Dr. T. Hanks
Nat'l Earthquake Resch Center
345 Middlefield Road
Menlo Park, CA 94025

Dr. James Hannon
Lawrence Livermore Nat'l Lab.
P.O. Box 808
Livermore, CA 94550

Paul Johnson
ESS-4, Mail Stop J979
Los Alamos National Laboratory
Los Alamos, NM 87545

Ms. Ann Kerr
DARPA/NMRO
1400 Wilson Boulevard
Arlington, VA 22209-2308

Dr. Max Koontz
US Dept of Energy/DP 5
Forrestal Building
1000 Independence Ave.
Washington, D.C. 20585

Dr. W. H. K. Lee
USGS
Office of Earthquakes, Volcanoes,
& Engineering
Branch of Seismology
345 Middlefield Rd
Menlo Park, CA 94025

Dr. William Leith
U.S. Geological Survey
Mail Stop 928
Reston, VA 22092

Dr. Richard Lewis
Dir. Earthquake Engineering and
Geophysics
U.S. Army Corps of Engineers
Box 631
Vicksburg, MS 39180

Dr. Robert Masse'
Box 25046, Mail Stop 967
Denver Federal Center
Denver, Colorado 80225

Richard Morrow
ACDA/VI
Room 5741
320 21st Street N.W.
Washington, D.C. 20451

Dr. Keith K. Nakanishi
Lawrence Livermore National Laboratory
P.O. Box 808, L-205
Livermore, CA 94550 (2 copies)

Dr. Carl Newton
Los Alamos National Lab.
P.O. Box 1663
Mail Stop C335, Group ESS-3
Los Alamos, NM 87545

Dr. Kenneth H. Olsen
Los Alamos Scientific Lab.
P.O. Box 1663
Mail Stop C335, Group ESS-3
Los Alamos, NM 87545

Howard J. Patton
Lawrence Livermore National
Laboratory
P.O. Box 808, L-205
Livermore, CA 94550

Mr. Chris Paine
Office of Senator Kennedy
SR 315
United States Senate
Washington, D.C. 20510

AFOSR/NP
ATTN: Colonel Jerry J. Perrizo
Bldg 410
Bolling AFB, Wash D.C. 20332-6448

HQ AFTAC/TT
Attn: Dr. Frank F. Pilotte
Patrick AFB, Florida 32925-6001

Mr. Jack Rachlin
USGS - Geology, Rm 3 C136
Mail Stop 928 National Center
Reston, VA 22092

Robert Reinke
AFWL/NTESG
Kirtland AFB, NM 87117-6008

Dr. Byron Ristvet
HQ DNA, Nevada Operations Office
Attn: NVCG
P.O. Box 98539
Las Vegas, NV 89193

HQ AFTAC/TGR
Attn: Dr. George H. Rothe
Patrick AFB, Florida 32925-6001

Donald L. Springer
Lawrence Livermore National Laboratory
P.O. Box 808, L-205
Livermore, CA 94550

Dr. Lawrence Turnbull
OSWR/NED
Central Intelligence Agency
CIA, Room 5G48
Washington, D.C. 20505

Dr. Thomas Weaver
Los Alamos National Laboratory
P.O. Box 1663
MS C 335
Los Alamos, NM 87545

GL/SULL
Research Library
Hanscom AFB, MA 01731-5000 (2 copies)

Secretary of the Air Force (SAFRD)
Washington, DC 20330
Office of the Secretary Defense
DDR & E
Washington, DC 20330

HQ DNA
ATTN: Technical Library
Washington, DC 20305

DARPA/RMO/RETRIEVAL
1400 Wilson Blvd.
Arlington, VA 22209

DARPA/RMO/Security Office
1400 Wilson Blvd.
Arlington, VA 22209

GL/XO
Hanscom AFB, MA 01731-5000

GL/LW
Hanscom AFB, MA 01731-5000

DARPA/PM
1400 Wilson Boulevard
Arlington, VA 22209

Defense Technical
Information Center
Cameron Station
Alexandria, VA 22314
(5 copies)

Defense Intelligence Agency
Directorate for Scientific &
Technical Intelligence
Washington, D.C. 20301

Defense Nuclear Agency/SPSS
ATTN: Dr. Michael Shore
6801 Telegraph Road
Alexandria, VA 22310

AFTAC/CA (STINFO)
Patrick AFB, FL 32925-6001

TACTEC
Battelle Memorial Institute
505 King Avenue
Columbus, OH 43201 (Final report only)

Mr. Alfred Lieberman
ACDA/VI-OA'State Department Building
Room 5726
320 - 21St Street, NW
Washington, D.C. 20451